THE UNIVERSITY OF QUEENSLAND

AUSTRALIA

BOSE-EINSTEIN CONDENSATES IN NON-HARMONIC OPTICAL POTENTIALS

Sebastian Schnelle

A THESIS SUBMITTED FOR THE DEGREE OF DOCTOR OF PHILOSOPHY AT
THE UNIVERSITY OF QUEENSLAND IN MARCH 2011
THE SCHOOL OF MATHEMATICS AND PHYSICS

Typeset in $\LaTeX\,2_\varepsilon$.

Declaration by Author

This thesis is composed of my original work, and contains no material previously published or written by another person except where due reference has been made in the text. I have clearly stated the contribution by others to jointly-authored works that I have included in my thesis.

I have clearly stated the contribution of others to my thesis as a whole, including statistical assistance, survey design, data analysis, significant technical procedures, professional editorial advice, and any other original research work used or reported in my thesis. The content of my thesis is the result of work I have carried out since the commencement of my research higher degree candidature and does not include a substantial part of work that has been submitted to qualify for the award of any other degree or diploma in any university or other tertiary institution. I have clearly stated which parts of my thesis, if any, have been submitted to qualify for another award.

I acknowledge that an electronic copy of my thesis must be lodged with the University Library and, subject to the General Award Rules of The University of Queensland, immediately made available for research and study in accordance with the Copyright Act 1968.

I acknowledge that copyright of all material contained in my thesis resides with the copyright holder(s) of that material.

Statement of Contributions to Jointly Authored Works Contained in the Thesis

S. K. Schnelle, E. D. van Ooijen, M. J. Davis, N. R. Heckenberg and H. Rubinsztein-Dunlop *Versatile two-dimensional potentials for ultra-cold atoms.* Opt. Express **16**, 1405 (2008).

Data acquisition was mainly carried out by this author with help from Dr van Ooijen. Data analysis and theory parts of the paper were mainly done by this author with help from Dr van Oijen and Dr Davis. The paper was drafted and written mainly by this author with contributions of all co-authors.

M. C. Garrett, A. Ratnapala, E. D. van Ooijen, C. J. Vale, K. Weegink, S. K. Schnelle, O. Vainio, N. R. Heckenberg, H. Rubinsztein-Dunlop and M. J. Davis *Growth dynamics of a Bose-Einstein condensate in a dimple trap without cooling.* Phys. Rev. A **83**, 013630 (2011).

Data acquisition was carried out by Dr Ratnapala (50%), Dr Vale (12.5%), Dr van Ooijen (12.5%), K. Weegink (12.5%) and this author (12.5%). Theory and calculations were mainly done by M. Garrett with help from Dr Davis. The paper was drafted and written mainly by M. Garrett with help from all co-authors.

Statement of Contributions by Others to the Thesis as a Whole

The work in this thesis would not have been possible without the guidance and support given by Dr Erik van Ooijen, Dr Mark Baker, Dr Matthew Davis, Prof. Norman Heckenberg and Prof. Halina Rubinsztein-Dunlop.

Statement of Parts of the Thesis Submitted to Qualify for the Award of Another Degree

None

Published Works by the Author Incorporated into the Thesis

S. K. Schnelle, E. D. van Ooijen, M. J. Davis, N. R. Heckenberg and H. Rubinsztein-Dunlop *Versatile two-dimensional potentials for ultra-cold atoms.* Opt. Express **16**, 1405 (2008).

M. C. Garrett, A. Ratnapala, E. D. van Ooijen, C. J. Vale, K. Weegink, S. K. Schnelle, O. Vainio, N. R. Heckenberg, H. Rubinsztein-Dunlop and M. J. Davis *Growth dynamics of a Bose-Einstein condensate in a dimple trap without cooling.* Phys. Rev. A **83**, 013630 (2011).

Additional Published Works by the Author Relevant to the Thesis but not Forming Part of it

None

Acknowledgements

First of all I would like to acknowledge and thank Dr Adrian Ratnapala, Kristian Weegink and Dr Erik van Ooijen for their part in the experiments presented in this thesis. Furthermore, I would like to acknowledge and thank Michael Garrett and Chao Feng for simulations presented in this thesis that help make sense of the data collected. Also, I would like to thank my supervisors Prof Halina Rubinsztein-Dunlop and Prof Norman Heckenberg for guidance through the experiments and while writing this thesis. Thanks also to Dr Mark Baker and Dr Jochen Kronjäger for corrections and suggestions improving this thesis. Thanks to the other people in the lab, Leif Humbert, Jessica Butcher and Daniel Sigle, for conversations about science and otherwise, including our camping trips away from the lab. Thanks also to A/Prof Matthew Davis and Dr Simon Haine for help making sense of the trickier parts of Bose-Einstein theory. Finally, I would like to thank all those involved with the Australian OSA chapters, especially the KOALA conference and outreach programs, which have been fun but also great experiences. Here I would like to mention Sarah Midgely (UQ), Catarina Sahlberg (Otago), Bill Corcoran (USYD) and Matthew Broom (UQ). Thanks to you all!

Abstract

This thesis presents work on Bose-Einstein condensates in non-harmonic optical potentials. First, a new trap design developed at the University of Queensland is presented that allows the creation of nearly arbitrary two-dimensional potential landscapes by spatially scanning a far red-detuned laser beam using a two-dimensional acousto-optic modulator. In conjunction with a feed-forward technique this trap is capable of producing optical traps which have the necessary stability to be used in ultra-cold atom research. Different geometries are presented. In particular toroidal trap geometries are discussed which are interesting because they offer the possibility for a multiply connected Bose-Einstein condensate. The trap also offers the possibility of dynamic potentials which have been employed to measure the critical velocity of superfluidity in Bose-Einstein condensates.

Secondly, measurements on condensation dynamics are presented which use an optical dimple potential superimposed upon a harmonic magnetic trap. In the experiments the dimple potential is ramped on slowly or turned on suddenly for a range of dimple depths and widths and the condensate fraction and temperature are measured as a function of hold times. The measurements taken are compared to equilibrium thermodynamics and quantum kinetic theory and for the first time a quantitative model is presented that allows correct prediction of condensate fractions and temperatures in good agreement with the measurements. Also presented are first results in condensate rethermalization experiments where a dimple potential is suddenly switched off and the condensate left to rethermalize in a much wider magnetic potential. The measurements show a sudden breakdown in condensate fraction followed by a subsequent recovery. So far no theory exists to properly interpret the results as quantum kinetic theory cannot be applied to the problem.

Lastly, progress on experiments to measure the critical velocity of superfluidity in Bose-Einstein condensates is reported. Calculations have been carried out that show the creation of solitons and vortices as mechanisms to dissipate energy leading to a breakdown of superfluid behaviour at velocities lower than that predicted by Landau's theory of superfluidity, the first theory to describe superfluidity. Progress on an experiment is presented that uses the scanning beam trap developed as part of this project to create a line potential with a moving barrier to measure the critical velocity and show solitons and vortices as the mechanisms for energy dissipation as seen in the calculations.

Keywords

bose-einstein condensate, optical trapping

Australian and New Zealand Standard Research Classifications (ANZSRC)

020601 Degenerate Quantum Gases and Atom Optics

Contents

List of Figures

List of Tables

1

Introduction

Bose-Einstein condensation (BEC) in dilute alkali gases is a fascinating phenomenon that allows the observation of quantum mechanical effects on a macroscopic scale. In this phenomenon the ground state of a system is occupied by a large number of atoms purely as a result of the quantum statistics for particles with integer spin. Experimentally BEC in dilute gases was first achieved in 1995 [1, 2] and the significance of this achievement was recognized by awarding the Nobel Prize in physics in 2001 to the principal investigators behind those projects. The area of Bose-Einstein condensation is still a very active field which has progressed greatly since the first achievement of BEC, and this thesis aims to provide a further piece of understanding in this fascinating field of physics.

1.1 A Short Historical Overview

The phenomenon of Bose-Einstein condensation was first described by Albert Einstein in 1925 [3] even before the invention of quantum mechanics and before particles were divided into particles with integer spin, now termed bosons, and those with half-integer spin, now termed fermions. Inspired by de Broglie's concept of the wave nature of particles with mass [4] which was published in 1923, Einstein extended the works of Satyendra Nath Bose's theory on the quantum statistics of photons [5] to particles with mass. Einstein realized that below a certain critical temperature T_c an ideal Bose gas of interaction-free particles would have a significant population of the ground state. It was not until 1938 when Fritz London suggested a connection between the phenomenon of superfluidity in helium and BEC, however, that there was a clue that such a state of matter could indeed exist [6]. This was the very first time that a system had been discovered which could be described by one multi-particle wavefunction. Since then, the phenomenon of Bose-Einstein condensation has been linked to several systems that exhibit previously unexpected behaviour such as superconductivity, where pairs of fermions form composite bosons [7], or Bose-Einstein condensates of excitons in semiconductors [8, 9].

Even though the systems mentioned above had been studied in great detail, there had still been a desire for a weakly interacting system that could be described from first principles. Long before BEC was achieved in dilute atomic vapours (the first long-lived, weakly interacting system that did satisfy that desire) the theory of such systems had been studied to gain insight into theoretically more complex systems, such as superfluid helium. BEC in dilute atomic vapours was the first system that allowed direct experimental tests of these theories.

The theoretical studies of BEC started with London's hunch that there might be a connection between superfluidity in liquid helium and BEC. Superfluidity, a sudden transition to a state with extremely low viscosity, had been discovered by Allen and Misener [10] and independently by Kapitza [11] in 1938. Two astounding discoveries in regard to superfluidity in liquid helium are the existence of persistent currents, discovered by Reppy and Depatie in 1964 [12], where the rotation of superfluid helium in a container does not decay due to a lack of friction between the fluid and the walls of the container, and the existence of a critical velocity below which an obstacle moved through a superfluid does not experience any friction. This critical velocity was measured for the first time for a macroscopic object in liquid helium by Castelijns and co-workers in 2007 [13].

A first phenomenological explanation of a critical velocity in superfluidity was given by Lev Landau who explained the phenomenon in terms of the quantization of excitations in the fluid. It was not until 1947, however, that Bogoliubov described the ground state and fundamental excitations from first principles [14]. Bogoliubov's theory, even though not strictly valid for liquid helium due to the strong interactions in that system, showed that Bose-Einstein condensation can occur in the presence of interactions, as suggested by London, and that the low-lying excitations of the ground state in this system are phononic in nature. Soon theoretical studies of systems with more complex interactions followed, including Penrose and Onsager's arguments for the existence of BEC in liquid helium [15] published in 1956. Nevertheless, the theoretical study of weakly interacting systems continued. These studies include the ground and lowest excited states in dilute systems of bosons [16, 17] (1957), the nature of the phase transition [18, 19] (1958), and sound propagation at finite temperature [20] (1959). It was not until the achievement of BEC in dilute atomic gases, however, that a system with interactions that could well be described by a mean-field term was realized, allowing the direct testing of these theories.

Since BEC in atomic vapours had first been achieved in 1995 with rubidium [1], sodium [2], and lithium [21] many more atoms have been shown to undergo Bose-Einstein condensation. So far the atoms ^{1}H, ^{7}Li, ^{23}Na, ^{39}K, ^{41}K, ^{52}Cr, ^{85}Rb, ^{87}Rb, ^{133}Cs, ^{170}Yb, ^{174}Yb, and ^{4}He* (the helium atom in a metastable excited state) have been Bose condensed [22]. Dilute quantum gases are special since the particle density at the centre of a BEC is typically $10^{13} - 10^{15}\text{cm}^{-3}$, which is much lower than the density of molecules in air at room temperature (10^{19}cm^{-3}), or the density of liquids (of order 10^{22}cm^{-3}). This means that the interactions between BEC atoms are small allowing for an accurate description through mean-field theories. This has led to many interesting publications on excitations [23–25], interference [26, 27], coherence [28–30], and other quantum effects early on in the study of BEC. More recently BECs have been applied to precision measurements [31, 32] and quantum information processing [33], while fundamental research is still ongoing where the probing of ultra-cold atoms in optical lattices on the single atom level [34] provides a beautiful example.

While some progress has been made on the understanding and observation of a critical velocity of superfluidity in Bose-Einstein condensates and the question on how coherence in BEC forms from incoherent thermal clouds, these are still open problems today. This thesis is aiming to further investigate these phenomena.

1.2 This Thesis

This thesis is arranged as follows. In Chapter 2, following this introduction, basic BEC theory will be summarized. This includes a thermodynamic description of BEC which allows calculation of the transition temperature and the percentage of condensed atoms at a given temperature. Then, a mean-field approach will be shown which leads to the well known Gross-Pitaevskii equation, which describes many basic features of BEC, including the existence of vortices and solitons. After that, Bogoliubov's theory of BEC will be presented in short which allows us to calculate important ground state properties, such as the speed of sound and the chemical potential of the system, as well as the excitation spectrum of a BEC which will be needed for work on superfluidity in BEC that will be presented later on in this thesis. These basic theoretical concepts had been developed since the 1940s and are well summarized in various textbooks and review articles. The approach taken here mainly follows that taken by Pitaevskii and Stringari [35] but also draws on the textbook by Pethick and Smith [22] and the review article by Dalfovo [36].

In Chapter 3 the basics of experimental realization of BEC will be recapitulated with an emphasis on the implementation of techniques to create BEC in the atom chip apparatus at the University of Queensland (UQ), where the presented work was conducted. The first BEC with this apparatus was created in 2004 and the machine has been described in detail in [37], [38] and [39]. The chapter includes details about the atomic structure of the element used in our experiments, which is ^{87}Rb, the basics of laser cooling and trapping and their implementation in the apparatus at UQ. The discussion is then extended to magnetic trapping and the UQ atom chip, as well as the basics of evaporative cooling and absorption imaging, which are necessary to reach the low temperatures necessary for BEC and to gain information about the system.

Chapter 4 will deal with a new trap design developed at the University of Queensland as part of this project. After some preliminary remarks on the optical dipole force which provides the physical mechanism behind the trap, the design of the scanning beam trap will be given in detail. The initial motivation for the development of the scanning beam trap was to create ring traps in which persistent currents in BEC could be created similar to the experiments on persistent currents carried out on superfluid helium presented in [12]. These persistent currents in BEC are of interest as the situation in dilute atomic vapours is open to theoretical modelling which is not the case for liquid helium. Unfortunately, due to the optical access to the vacuum chamber the BEC is created in, these experiments could not be realized in the existing atom chip apparatus at UQ. However, as the design of the scanning beam trap allows the creation of nearly arbitrary two-dimensional potential surfaces, work on the trap was concluded and further experiments developed which would not be hampered by the optical access available. The trap makes use of an optical dipole trap that is scanned with a two-dimensional acousto-optic modulator (AOM), such that the atoms experience a time averaged potential. The design and first measurements on BEC in the scanning trap have been published in [40].

Chapter 5 presents details of our further investigation into condensation dynamics in a dimple trap, which builds on previous work from our group [39]. The dimple trap consists of a small optical potential that is superimposed upon a much larger magnetic trap. These experiments are of interest because the process by which a thermal cloud exhibits coherence properties when cooled through the BEC transition is still an open problem. While some early theoretical work on condensate formation gave quantitative predictions [41] these predictions differed from measurements done by Miesner *et al.* [42] even after the theorists revised their models [43–45]. Measurements at UQ have been performed to compare a new quantum kinetic model to experimental data with good success and the results have been published in [46]. Also presented are first results on the rethermalization of a BEC when a dimple potential is suddenly switched off, leaving the BEC to rethermalize in a much wider magnetic trap for which no theory exists so far.

Chapter 6 will present progress to date on an experiment to measure the critical velocity of superfluidity in BEC. Superfluidity and a critical velocity of superfluidity were first observed in liquid helium when cooled below the so called λ-point and the phenomenon was linked to Bose-Einstein condensation by Fritz London in 1938. In the early 1940s a phenomenological explanation was given by Lev Landau, according to whose theory the critical velocity should be identical to the speed of sound in the system. Shortly after BEC in dilute gases was achieved this critical velocity was measured in BEC and compared to the speed of sound of the system, where a discrepancy between the two was found [47]. After a more recent experiment also found a discrepancy between the critical velocity and the speed of sound in BEC [48] it received renewed theoretical attention. In those new simulations it was found that the critical velocity should be lower than the speed of sound in the system due to the existence of solitons which provide a means to dissipate energy [49]. It was found that the scanning beam trap was ideally suited to measure the critical velocity in BEC since it allows us to overcome the shortcomings of previous measurements which might have caused the discrepancies while enabling a setup that mimics very closely the original situation in liquid helium where an obstacle is moved through the liquid. Here I will present one-dimensional Gross-Pitaevskii calculations, which were carried out to find the right parameter space for the experiments but turned out not to be sufficient to observe the occurrence of solitons in the system. After that, I am going to present more complex simulations carried out by Chao Feng in which vortex rings and solitons can be demonstrated as a means of energy transfer. Finally, I am going to present the results to date on the attempt to measure the critical velocity using the scanning trap.

2

BEC Theory

Below a critical temperature a gas of identical bosons will exhibit a significant occupation of the system's ground state. This phase transition is referred to as Bose-Einstein condensation. The reason for this phase transition can be found in the distribution function followed by bosonic particles. This function was first proposed by Bose in 1924 to describe black-body radiation [5]. Einstein then built on Bose's work and extended the distribution function to include particles with mass [3]. The Bose-Einstein distribution function can be written as

$$N_i = \left[\exp\left(\frac{\epsilon_i - \mu}{k_B T}\right) - 1\right]^{-1}, \tag{2.1}$$

where N_i is the mean occupation number for a state with energy ϵ_i, k_B the Boltzmann constant and μ the chemical potential. Using the Grand Canonical description of thermodynamics the chemical potential can be related to the particle number N and temperature T of a system because of the fact that for massive particles, the total number of particles N is a conserved quantity. Because of this conservation law the total number of particles can be calculated as the sum of the particle numbers in individual energy levels

$$N = \sum_i N_i. \tag{2.2}$$

For high temperatures the quantum nature of this distribution can be neglected and the Bose-Einstein distribution turns into the Boltzmann distribution.

For low temperatures, however, quantum effects become important. When lowering the temperature, the chemical potential is raised to asymptotically approach the lowest possible energy value ϵ_0. The chemical potential cannot become larger than this value because otherwise the occupation numbers for the lowest energy levels would have to become negative. As a result of this rise in μ the occupation number in the lowest energy state increases. For

$\mu = \epsilon_0$ the occupation number in the ground state becomes significant and the temperature at which this happens is called the critical temperature T_c, which can be found using Eqns. (2.1) and (2.2).

In the following sections basic theoretical concepts for the description of Bose-Einstein condensates will be summarized. These concepts have been extensively researched and good textbooks and review articles on the subject are available. The summary given here will mainly follow the approach taken by Pitaevskii and Stringari [35] but also draws heavily on information found in [22] and [36]. First, a thermodynamic explanation will be given which can be used to calculate the critical temperature and the fraction of condensed atoms. Then, in a second step, a quantum mechanical description will be summarized which can be used to calculate the density profile, speed of sound and excitation spectrum of a Bose-Einstein condensate.

2.1 Thermodynamic Description Of BEC

In the following section, the thermodynamic properties of interacting bosons in anisotropic harmonic potentials will be discussed. These can be used to calculate the temperature for the quantum phase transition (i.e. the beginning of a significant occupation of the ground state) as well as the fraction of condensed atoms depending on the temperature. These results can be used to describe the experimental situation since the actual trapping potentials used in this work are harmonic in a first approximation. Replacing the summation in Eqn. (2.2) with an integral and substituting the expression for N_i from Eqn. (2.1)

$$N = \int_0^\infty \mathrm{d}\epsilon \quad g(\epsilon) n(\epsilon), \tag{2.3}$$

where the density of states $g(\epsilon)$ of energy ϵ for a harmonic potential is given by

$$g(\epsilon) = \frac{\epsilon^2}{2\hbar\bar{\omega}^3}, \tag{2.4}$$

and ω_i are the trap frequencies in $i = x,\ y,\ z$ direction with mean trapping frequency $\bar{\omega} = (\omega_x\omega_y\omega_z)^{1/3}$ [50]. This approximation does not take into account the ground state which has to be considered separately. Ignoring the ground state energy for a moment, the chemical potential can have a maximum value of zero. This is because the chemical potential has to be smaller than the ground state energy because otherwise the occupation numbers for the lowest energy state would have to become negative. The critical temperature can therefore be calculated from

$$\begin{aligned} N(T, \mu = 0) &= \int_0^\infty \mathrm{d}\epsilon \quad g(\epsilon)[\exp(\epsilon/[k_B T]) - 1]^{-1} \\ &= 2\zeta(3)\frac{1}{2\hbar\bar{\omega}^3}(k_B T)^3, \end{aligned} \tag{2.5}$$

where ζ is the Riemann zeta function. T_c can therefore be written as

$$T_c = \frac{\hbar\bar{\omega}N^{1/3}}{k_B\zeta(3)^{1/3}} \approx 0.94\frac{\hbar\bar{\omega}}{k_B}N^{1/3}. \tag{2.6}$$

At T_c the distribution given by Eqn. (2.1) is just able to contain all the particles. Upon further cooling this is no longer the case and those particles that do not fit into this distribution have to be contained in the ground state of the systems as this is the only state that is not accounted for in the equation.

From Eqn. (2.6) it can be seen that the critical temperature scales linearly with the mean trapping frequency $\bar{\omega}$ and as the cube root of the particle number N. Stronger trapping and more atoms will therefore lead to higher transition temperatures, something that is important to keep in mind for the experimental realization of BEC.

Below the transition temperature the distribution of particles in excited states is governed by Eqn. (2.5), independently of the total number of particles N_{tot}. This number is given by combining the number of thermal particles N_{therm} and the number of particles in the ground state N_0 as

$$N_{tot} = N_{therm} + N_0. \tag{2.7}$$

Using this and the knowledge from Eqn. (2.5) that the number of thermal particles scales as T^3, the relative occupation of the ground state for harmonic potentials can be written as [36]

$$\frac{N_0}{N_{tot}} = 1 - \left(\frac{T}{T_c}\right)^3. \tag{2.8}$$

The fraction of condensed atoms will therefore rise quickly once below T_c. At $T = 0.5 \cdot T_c$ for example, 87.5 % of particles will be in the ground state. This ensures that once below the critical temperature effects of the phase transition do become visible in the experimental realization of BEC.

2.2 Mean-Field Theory

A theory that describes Bose-Einstein condensation of dilute atomic gases needs to account for the fact that real atoms will have inter-atomic interactions. Unlike other many-body systems with strong inter-atomic interactions which make theoretical treatment hard, such as liquid helium for example, interactions in dilute atomic gases are weak making accurate theoretical modelling feasible through the use of a *mean-field* approach. In such an approach the effects on a particular atom from interactions with all the other atoms are considered by treating the atom in question as influenced by a mean-field which is created by all the other atoms.

To achieve such a theoretical description one has to remember that the time evolution of the field operator $\hat{\Psi}(\mathbf{r},t)$, in the Heisenberg representation, is exactly described by

$$i\hbar\frac{\partial}{\partial t}\hat{\Psi}(\mathbf{r},t) = [\hat{\Psi}(\mathbf{r},t),\hat{H}] = \left[-\frac{\hbar^2\nabla^2}{2m} + \mathrm{V}_{ext}(\mathbf{r},t) + \int c\mathrm{V}(\mathbf{r}'-\mathbf{r})\hat{\Psi}(\mathbf{r}',t)\mathrm{d}\mathbf{r}'\right]\hat{\Psi}(\mathbf{r},t), \quad (2.9)$$

where V_{ext} is an external potential and $\mathrm{V}(\mathbf{r}'-\mathbf{r})$ the interaction potential [35]. The field operators obey the commutation relations for bosons $[\hat{\Psi}(\mathbf{r},t),\hat{\Psi}^\dagger(\mathbf{r}',t)] = \delta(\mathbf{r}-\mathbf{r}')$. If only two-body interactions at low energies are considered, the s-wave scattering length a_s is sufficient to describe the physical properties of the interaction as all other interaction channels are frozen out. Therefore, it is possible to write

$$\mathrm{V}(\mathbf{r}-\mathbf{r}') = g\delta(\mathbf{r}-\mathbf{r}') \qquad \text{where} \qquad g = \frac{4\pi\hbar^2 a_s}{m} \quad (2.10)$$

In the *mean-field* description the field operator can now be identified with $\hat{\Psi}(\mathbf{r},t) = \Psi(\mathbf{r},t) + \theta(\mathbf{r},t)$, where $\Psi(\mathbf{r},t)$ is a complex function and can be viewed as a classical field representing the expectation value of the field operator and $\theta(\mathbf{r},t)$ describes fluctuations around this expectation value. For systems, like dilute atomic gases, where the scattering length a_s is much smaller than the mean interparticle spacing and where the wave function of the system can be written as a symmetrized product of single particle wave functions the condensate fraction can be described by the *mean-field* whereas the fluctuations only cause minor corrections that can safely be neglected. This situation is analogous to the situation in quantum electrodynamics where a large number of photons in the same quantum state allows the transition to classical electromagnetism because the non-commutativity of the field operators can be neglected and the electromagnetic field can be described by classical fields obeying the Maxwell equations. Using Eqns. (2.10) and (2.9) one gets to the Gross-Pitaevskii equation:

$$i\hbar\frac{\partial}{\partial t}\Psi(\mathbf{r},t) = \left(-\frac{\hbar^2\nabla^2}{2m} + \mathrm{V}_{ext}(\mathbf{r}) + g|\Psi(\mathbf{r},t)|^2\right)\Psi(\mathbf{r},t). \quad (2.11)$$

This equation is a non-linear Schrödinger equation, where the non-linearity is caused by the atomic interactions. It is this non-linearity that enables a rich amount of interesting physics in Bose-Einstein condensates of dilute atomic gases, such as the observation of solitons and vortices as well as four-wave mixing. Separating $\Psi(\mathbf{r},t) = \phi(\mathbf{r}) * \exp(-i\mu t/\hbar)$ one gets the time independent version of the Gross-Pitaevskii equation

$$\left(-\frac{\hbar^2\nabla^2}{2m} + \mathrm{V}_{ext}(\mathbf{r}) + g|\phi(\mathbf{r})|^2\right)\phi(\mathbf{r}) = \mu\phi(\mathbf{r}). \quad (2.12)$$

Here, the chemical potential μ gives the energy necessary to add another particle to the condensate, while the number of condensate atoms is given through the integral over the square of the wavefunction, because $|\phi(\mathbf{r})|^2 = n(\mathbf{r})$ gives the density of the condensate wavefunction. The sign of the inter-atomic interaction is determined through the s-wave scattering length a_s, which in the case of ^{87}Rb is positive, leading to a repulsive interaction. The fact that the interaction is repulsive stabilizes the Bose-Einstein condensate, amongst other things because it limits the density and therefore prevents a collapse as well as reducing the number of three-body losses.

2.2.1 The Thomas-Fermi Approximation

In general it is not possible to find an analytic solution for the Gross-Pitaevskii equation (2.11) due to the non-linearity. Because of this it is necessary to employ either numerical methods or approximations. In the following section the so called Thomas-Fermi approximation will be summarized. It assumes that the kinetic energy term in Eqn. (2.11) is much smaller than the potential energy term. This allows one to neglect the kinetic energy term and the local density can be calculated to be

$$n(\mathbf{r}) = |\phi(\mathbf{r})|^2 = \begin{cases} \frac{\mu - \mathrm{V}_{ext}(\mathbf{r})}{g} & \text{if} \quad \mu - \mathrm{V}_{ext} > 0, \\ 0 & \quad \text{otherwise.} \end{cases} \tag{2.13}$$

Using this the radius of the wavefunction can now easily be calculated by equating $\mu = \mathrm{V}_{ext}$:

$$r_i = \sqrt{\frac{2\mu}{m\omega_i^2}}, \qquad \text{with} \qquad i = x, y, z. \tag{2.14}$$

To calculate a value for r_i a value for the chemical potential has to be known. The normalization condition of $\phi(\mathbf{r})$ gives the relation between the chemical potential and the particle number. For harmonic trapping potentials [35]

$$\mu = \frac{15^{2/5}}{2} \left(a_s N \sqrt{\frac{m\omega}{\hbar}} \right)^{2/5} \hbar\omega. \tag{2.15}$$

All these results can be used to get information about the density distribution of Bose-Einstein condensates and therefore will be used as a basis for fits to images taken of the condensates.

2.3 Bogoliubov Theory Of The Weakly-Interacting Gas

As will be shown in a later chapter, to calculate the critical velocity of superfluidity in BEC it is necessary to know the speed of sound and the excitation spectrum of the system. This cannot be calculated from mean-field theory and it is therefore necessary to look at the full quantum system again. Since the full quantum system is hard to calculate, several approximations have been proposed by Bogoliubov in 1947. Firstly, it can be assumed that in a dilute gas the inter-particle spacing $d = n^{-1/3}$, given by the density $n = N/V$, is much larger than the range of the inter-atomic forces r_0. As a result, configurations with three or more interacting atoms can be neglected, leaving only pairs of interacting particles to be considered. Secondly, it can be assumed that the inter-particle spacing is always large enough to neglect specific details of the two-body interaction, using only the scattering amplitude to calculate interactions. Thirdly, only gases at temperatures well below the critical temperature for BEC, T_{c}, shall be considered so that the momenta p involved always satisfy the inequality

$$\frac{pr_0}{\hbar} \ll 1. \tag{2.16}$$

If all of these three conditions are satisfied, the scattering amplitude becomes independent of energy as well as of the scattering angle and can be replaced by the s-wave scattering length a_s. This parameter now describes all the physically relevant interaction properties of the gas.

2.3.1 Ground State Energy

The above mentioned approximations can now be used to calculate the ground state energy of the system. If we write the Hamiltonian of the system in terms of the field operators without the inclusion of external fields, we get [35]

$$\hat{H} = \int \left(\frac{\hbar^2}{2m} \nabla \hat{\Psi}^\dagger \nabla \hat{\Psi} \right) \mathrm{d}\mathbf{r} + \frac{1}{2} \int \hat{\Psi}^\dagger \hat{\Psi}^{\dagger\prime} V(\mathbf{r}' - \mathbf{r}) \hat{\Psi} \hat{\Psi}' \, \mathrm{d}\mathbf{r}' \, \mathrm{d}\mathbf{r}, \tag{2.17}$$

where $V(\mathbf{r})$ is the two-body potential. For a uniform gas in a volume V, the field operators can be written as

$$\hat{\Psi}(\mathbf{r}) = \sum_{\mathbf{p}} \hat{a}_{\mathbf{p}} \frac{1}{\sqrt{V}} \exp(i\mathbf{p} \cdot \mathbf{r}/\hbar), \tag{2.18}$$

where $\hat{a}_{\mathbf{p}}$ is the operator annihilating a single particle with momentum $\mathbf{p}$. Substituting (2.18) into (2.17) gives the Hamiltonian in terms of the single-particle creation and annihilation operators

$$\hat{H} = \sum \frac{p^2}{2m} \hat{a}^\dagger_{\mathbf{p}} \hat{a}_{\mathbf{p}} + \frac{1}{2V} \sum V_{\mathbf{q}} \hat{a}^\dagger_{\mathbf{p_1}+\mathbf{q}} \hat{a}^\dagger_{\mathbf{p_2}-\mathbf{q}} \hat{a}_{\mathbf{p_1}} \hat{a}_{\mathbf{p_2}}, \tag{2.19}$$

with $V_{\mathbf{q}} = \int V(\mathbf{r}) \exp[-\mathrm{i}\mathbf{q} \cdot \mathbf{r}/\hbar] \, \mathrm{d}\mathbf{r}$ and where the first summation is over $\mathbf{p}$ and the second summation is over $\mathbf{p_1}, \mathbf{p_2}$ and $\mathbf{q}$. Because the scattering of slow particles, where slow means approaching on a time scale below that of the trapping frequency of the potential, cannot be worked out using perturbation theory, the real microscopic potential with its short-range terms is now replaced with a soft potential V_{eff}. This approximation holds due to the diluteness condition, as a result of which the actual form of the two-body potential is not important, provided that the potential used gives the correct value of the s-wave scattering length.

Since only small momenta are involved in the solution of the many-body problem, only $q = 0$ values of the Fourier transform of V_{eff} are considered:

$$V_0 = \int V_{\mathrm{eff}}(r) \, \mathrm{d}\mathbf{r} \tag{2.20}$$

resulting in the Hamiltonian

$$\hat{H} = \sum \frac{p^2}{2m} \hat{a}^\dagger_{\mathbf{p}} \hat{a}_{\mathbf{p}} + \frac{1}{2V} V_0 \sum \hat{a}^\dagger_{\mathbf{p_1+q}} \hat{a}^\dagger_{\mathbf{p_2-q}} \hat{a}_{\mathbf{p_1}} \hat{a}_{\mathbf{p_2}}. \tag{2.21}$$

The most important step in Bogoliubov's theory however is the prescription to replace the operators $\hat{a}_0$ with a complex number [35]

$$\hat{a}_0 \equiv \sqrt{N_0} \tag{2.22}$$

in the Hamiltonian (2.21). While in the case of an ideal gas at $T = 0$ all atoms would be in the condensate and therefore $N_0 = N$, for dilute gases at finite temperatures the occupation numbers for states with momenta $\mathbf{p} \neq 0$ are finite but small. As a result, the operators $\hat{a}_{\mathbf{p}}$ and $\hat{a}^\dagger_{\mathbf{p}}$ with $\mathbf{p} \neq 0$ can in the first approximation be neglected and $\hat{a}_0$ be replaced with $\sqrt{N_0}$. Keeping in mind that $N_0 \approx N$ the ground state energy takes the form

$$E_0 = \frac{N^2 V_0}{2V}. \tag{2.23}$$

This result is strictly valid only for situations in which there are mainly condensed atoms, which is not the case for the work in this thesis and for many other experiments. However, the result is still useful as a first approximation as it turns out that it often describes the state of the condensed atoms very well, even in the presence of a thermal cloud. Yet, care should be taken, whenever there is a substantial thermal component.

Using the result of the Born approximation the parameter V_0 can be rewritten in terms of the scattering length a_s as $V_0 = 4\pi\hbar^2 a_s/m$, resulting in a ground state energy that can be expressed as

$$E_0 = \frac{1}{2} N n g, \tag{2.24}$$

where $n = N/V$ is the density of the gas and g is the interaction coupling constant

$$g = \frac{4\pi\hbar^2 a_s}{m}, \tag{2.25}$$

fixed by the s-wave scattering length a_s.

Using Eqn. (2.24) the pressure of a weakly interacting gas can be calculated to be

$$P = -\frac{\partial E_0}{\partial V} = \frac{g n^2}{2}. \tag{2.26}$$

Accordingly, the compressibility can be shown to be finite and

$$\frac{\partial n}{\partial P} = \frac{1}{g n}. \tag{2.27}$$

From the hydrodynamic relation

$$\frac{1}{mc^2} = \frac{\partial n}{\partial P} \tag{2.28}$$

the sound velocity in a dilute gas can be calculated to be

$$c = \sqrt{\frac{gn}{m}}. \tag{2.29}$$

Unlike the ideal gas case, it has to be remarked that the chemical potential is not equal to zero. Instead, the chemical potential can be calculated to be

$$\mu = \frac{\partial E_0}{\partial N} = gn \tag{2.30}$$

which is always positive. Combining this with Eqn. (2.29) we get an expression for the chemical potential in terms of the speed of sound c

$$\mu = mc^2. \tag{2.31}$$

Using Bogoliubov's approximation, it is therefore possible to find the speed of sound in a BEC which it turns out depends only on the interaction constant, the local density and the mass of the isotope used in an experiment. This speed of sound will be shown in a later chapter to be equal to the critical velocity of superfluidity in BEC according to Landau's theory of superfluidity. Yet, to get to that result it will be necessary to know the exact form of the excitation spectrum of a trapped Bose gas of dilute atoms which cannot be calculated using these approximations. The next section will therefore include higher order terms to calculate said excitation spectrum.

2.3.2 Excitation Spectrum

In order to calculate result (2.24) only single particle operators $\hat{a}_{\mathbf{p}}$ and $\hat{a}^{\dagger}_{\mathbf{p}}$ with momentum $\mathbf{p} = 0$ had been considered in Eqn. (2.21). If one wants to calculate the excitation spectrum it is necessary to include one-particle operators with $\mathbf{p} \neq 0$. By retaining all the quadratic terms in the particle operators (2.18) the Hamiltonian (2.17) can be rewritten as [35]

$$\hat{H} = \frac{V_0}{2V}\hat{a}^{\dagger}_0\hat{a}^{\dagger}_0\hat{a}_0\hat{a}_0 + \sum_{\mathbf{p}} \frac{p^2}{2m}\hat{a}^{\dagger}_{\mathbf{p}}\hat{a}_{\mathbf{p}} + \frac{V_0}{2V}\sum_{\mathbf{p}\neq 0}(4\hat{a}^{\dagger}_0\hat{a}^{\dagger}_{\mathbf{p}}\hat{a}_0\hat{a}_{\mathbf{p}} + \hat{a}^{\dagger}_{\mathbf{p}}\hat{a}^{\dagger}_{-\mathbf{p}}\hat{a}_0\hat{a}_0 + \hat{a}^{\dagger}_0\hat{a}^{\dagger}_0\hat{a}_{\mathbf{p}}\hat{a}_{-\mathbf{p}}). \tag{2.32}$$

As done previously $\hat{a}_0$ and $\hat{a}^{\dagger}_0$ can be replaced with $\sqrt{N}$ in the third term of Eqn. (2.32). Nevertheless, in the first term one has to work with higher accuracy using the normalization condition

$$\hat{a}^{\dagger}_0\hat{a}_0 + \sum_{\mathbf{p}\neq \mathbf{0}} \hat{a}^{\dagger}_{\mathbf{p}}\hat{a}_{\mathbf{p}} = N. \tag{2.33}$$

to get the approximation

$$\hat{a}_0^\dagger \hat{a}_0^\dagger \hat{a}_0 \hat{a}_0 = N^2 - 2N \sum_{\mathbf{p}\neq\mathbf{0}} \hat{a}_{\mathbf{p}}^\dagger \hat{a}_{\mathbf{p}}. \tag{2.34}$$

Where in the previous section the first-order Born approximation connected the scattering-length and the parameter V_0 to calculate the excitation spectrum it is now necessary to calculate a_s up to quadratic terms in V_0. From higher-order perturbation theory one can find (Landau and Lifshitz [51], §130)

$$a_s = \frac{m}{4\pi\hbar^2}\left(V_0 - \frac{V_0^2}{V}\sum_{\mathbf{p}\neq 0}\frac{m}{p^2}\right). \tag{2.35}$$

This yields V_0 with equivalent accuracy as

$$V_0 = g\left(1 + \frac{g}{V}\sum_{\mathbf{p}\neq 0}\frac{m}{p^2}\right), \tag{2.36}$$

where $V_0 = 4\pi\hbar^2 a_s/m$ previously. Equation (2.36) therefore re-normalizes the relationship between effective potential V_{eff} and the physical coupling constant $g = 4\pi\hbar^2 a_s/m$, where the matrix element $V_{\mathbf{q}}$ in Eqn. (2.19) has been replaced with the constant value V_0.

Substituting Eqns. (2.34) and (2.36) into the Hamiltonian (2.32) leads to the expression

$$\hat{H} = g\frac{N^2}{2V} + \sum_{\mathbf{p}}\frac{p^2}{2m}\hat{a}_{\mathbf{p}}^\dagger \hat{a}_{\mathbf{p}} + \frac{1}{2}gn\sum_{\mathbf{p}\neq 0}\left(2\hat{a}_{\mathbf{p}}^\dagger \hat{a}_{\mathbf{p}} + \hat{a}_{\mathbf{p}}^\dagger \hat{a}_{-\mathbf{p}}^\dagger + \hat{a}_{\mathbf{p}}\hat{a}_{-\mathbf{p}} + \frac{mgn}{p^2}\right). \tag{2.37}$$

It turns out that this expression is uniquely fixed by the coupling constant g.The Hamiltonian (2.37) is quadratic in the creation and annihilation operators and can be diagonalized using the Bogoliubov transformations, a set of linear transformations that uses a new set of operators, $\hat{b}_{\mathbf{p}}$ and $\hat{b}_{\mathbf{p}}^\dagger$, obeying the Bose commutation relations

$$\left[\hat{b}_{\mathbf{p}}, \hat{b}_{\mathbf{p}'}^\dagger\right] = \delta_{\mathbf{p}\mathbf{p}'}. \tag{2.38}$$

The linear transformations can be written as [35]

$$\hat{a}_{\mathbf{p}} = u_{\mathbf{p}}\hat{b}_{\mathbf{p}} + v_{-\mathbf{p}}^*\hat{b}_{-\mathbf{p}}^\dagger \tag{2.39}$$

$$\hat{a}_{\mathbf{p}}^\dagger = u_{\mathbf{p}}^*\hat{b}_{\mathbf{p}}^\dagger + v_{-\mathbf{p}}\hat{b}_{-\mathbf{p}}. \tag{2.40}$$

The commutation relations are satisfied if

$$|u_{\mathbf{p}}|^2 - |v_{-\mathbf{p}}|^2 = 1, \tag{2.41}$$

leading to

$$u_{\mathbf{p}} = \cosh\alpha_{\mathbf{p}}, \qquad v_{-\mathbf{p}} = \sinh\alpha_{\mathbf{p}}, \tag{2.42}$$

where the parameter $\alpha_{\mathbf{p}}$ can be chosen freely. For convenience $\alpha_{\mathbf{p}}$ will be chosen such that the diagonal terms $\hat{b}^{\dagger}_{\mathbf{p}}\hat{b}^{\dagger}_{-\mathbf{p}}$ and $\hat{b}_{\mathbf{p}}\hat{b}_{-\mathbf{p}}$ in the Hamiltonian (2.37) vanish. The explicit form of those coefficients can be found to be [35]

$$u_{\mathbf{p}}, v_{-\mathbf{p}} = \pm\left(\frac{p^2/2m + gn}{2\epsilon(p)} \pm \frac{1}{2}\right)^{1/2}, \tag{2.43}$$

where $\epsilon(p)$ is the Bogoliubov dispersion law for elementary excitations which has the form

$$\epsilon(p) = \left[\frac{gn}{m}p^2 + \left(\frac{p^2}{2m}\right)^2\right]^{1/2}. \tag{2.44}$$

A graph of this equation can be found in Fig. 2.1. The Hamiltonian (2.37) can now be written in terms of the Bogoliubov operators $\hat{b}$ and $\hat{b}^{\dagger}$ as

$$\hat{H} = E_0 + \sum_{\mathbf{p}} \epsilon(p)\hat{b}^{\dagger}_{\mathbf{p}}\hat{b}_{\mathbf{p}}, \tag{2.45}$$

where

$$E_0 = g\frac{N^2}{2V} + \frac{1}{2}\sum_{\mathbf{p}\neq 0}\left[\epsilon(p) - gn - \frac{p^2}{2m} + \frac{m(gn)^2}{p^2}\right] \tag{2.46}$$

is the ground state energy for independent quasi-particles having energy $\epsilon(\mathbf{p})$ and whose annihilation and creation operators are $\hat{b}$ and $\hat{b}^{\dagger}$, respectively. From Eqn. (2.44) it can be seen that for small momenta $p \ll mc$ the dispersion law of quasi-particles takes the phonon-like form

$$\epsilon(p) = cp \tag{2.47}$$

since the squared term in Eqn. (2.44) tends to zero much quicker than the linear term, where $c = \sqrt{gn/m}$ is the sound velocity as defined by Eqn. (2.29). It will later be shown that the minimum of the excitation spectrum (2.44), which is shown in Fig. 2.1, divided by the momentum p is not only identical to the speed of sound but also gives the superfluid critical velocity of a Bose-Einstein condensate according to Landau's theory of superfluidity.

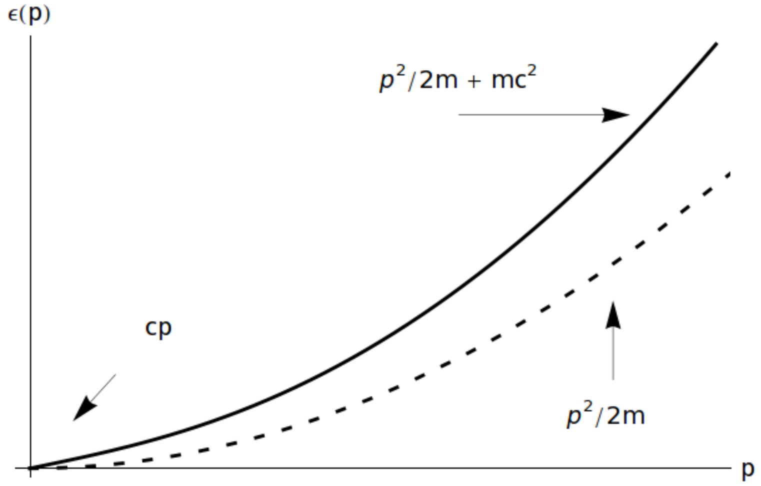

Figure 2.1: Excitation spectrum of a weakly interacting Bose gas. The solid line shows the energy dependence of an elementary excitation with the low energy limit indicating a phononic excitation [$\epsilon(p) = cp$] proportional to the speed of sound in the gas and the high energy limit where excitations behave almost like free particles [$p^2/2m + mc^2$]. The dispersion relation for free particles is shown as dashed line.

3

Experimental Realization Of BEC

Bose-Einstein condensates were created for the first time in 1995 almost 70 years after their prediction by Einstein. One reason for the long time lapse between prediction and realization is that techniques had to be developed to reach the low temperatures in the nanokelvin regime that are necessary to form Bose-Einstein condensates. Since even liquid helium temperatures of a few millikelvin are not low enough for dilute gases to undergo the BEC phase transition, laser cooling methods had to be employed to cool the atom clouds. However, even those cooling methods did not provide low enough temperatures so that a further non-radiative cooling step had to be developed. It was the evaporative cooling step that made Bose-Einstein condensation possible in conjunction with the technologies and techniques that had been developed earlier. Since the first realization of Bose-Einstein condensation standard techniques have emerged to create BEC. The following chapter will outline those standard techniques, such as magneto-optical trapping, molasses cooling, magnetic trapping, etc. and describe in some detail the implementation of said techniques in the apparatus used at the University of Queensland.

3.1 Rubidium 87

Bose-Einstein condensation has now been achieved with many elements, which have been listed in full above. However, sodium and rubidium, the first two elements that BEC was achieved with, are still most commonly used due originally to the availability of laser equipment and ease of operation. In the case of our lab, there is a history of experience with rubidium. This is why in our case the element of choice is ^{87}Rb, a non-stable isotope of rubidium (the only stable isotope is ^{85}Rb) with a very long nuclear lifetime of 4.88×10^{10} years [52]. Rubidium 87 is a good isotope to work with since it has an excitation frequency from the lowest to the second excited state (D2 line) at around 780nm where laser diodes are

Table 3.1: Physical properties of ^{87}Rb. Reproduced from [52].

Atomic Number	Z	37
Total Nucleons	$Z+N$	87
Relative Natural Abundance	η	27.83(2) %
Nuclear Lifetime	τ	4.88×10^{10}yr
Atomic Mass	m	$1.44316060(11) \times 10^{-25}$kg
Melting Point	T_M	39.31°C
Boiling Point	T_B	688°C
Nuclear Spin	I	3/2

Table 3.2: D_2 transition optical properties of ^{87}Rb. Reproduced from [52].

Frequency	ω_0	$2\pi \cdot 384.230$THz
Transition Energy	$\hbar\omega_0$	1.589eV
Wavelength (Vacuum)	λ	780.241nm
Wavelength (Air)	λ_{air}	780.032nm
Lifetime	τ	26.24ns
Decay Rate	Γ	38.11×10^6 s^{-1}
Recoil Temperature	T_{r}	361.96nK
Doppler Temperature	T_{D}	146μK

available. Also, like all alkalis it has a large vapour pressure at modest temperatures making the handling of rubidium in an ultra-high vacuum system relatively easy. A summary of some of the physical parameters of ^{87}Rb are shown in Table 3.1 while Table 3.2 shows some of the optical properties of the D_2 transition.

Rubidium has 37 electrons, only one of which is in the outermost shell. While this situation is easier to understand than that of atomic species with more than one electron in the outermost shell, it is still the case that atoms have more than two levels, and that in general light couples to more than two levels at the same time when taking into account fine and hyper-fine structure of the atom. Most importantly, there are decay channels in existence which allow atoms to leave the cycling transition used for laser cooling and trapping. As a result, as will be explained below, in addition to the light field driving the transition used for the cooling of the atoms, it is necessary to have a second light field. This light field is to return those atoms that use other decay channels to the desired cooling transition. The second light field is usually referred to as ‘repump’ transition. A level scheme of ^{87}Rb is shown in Fig. 3.1 including the hyperfine levels and with cooling and repump transitions indicated.

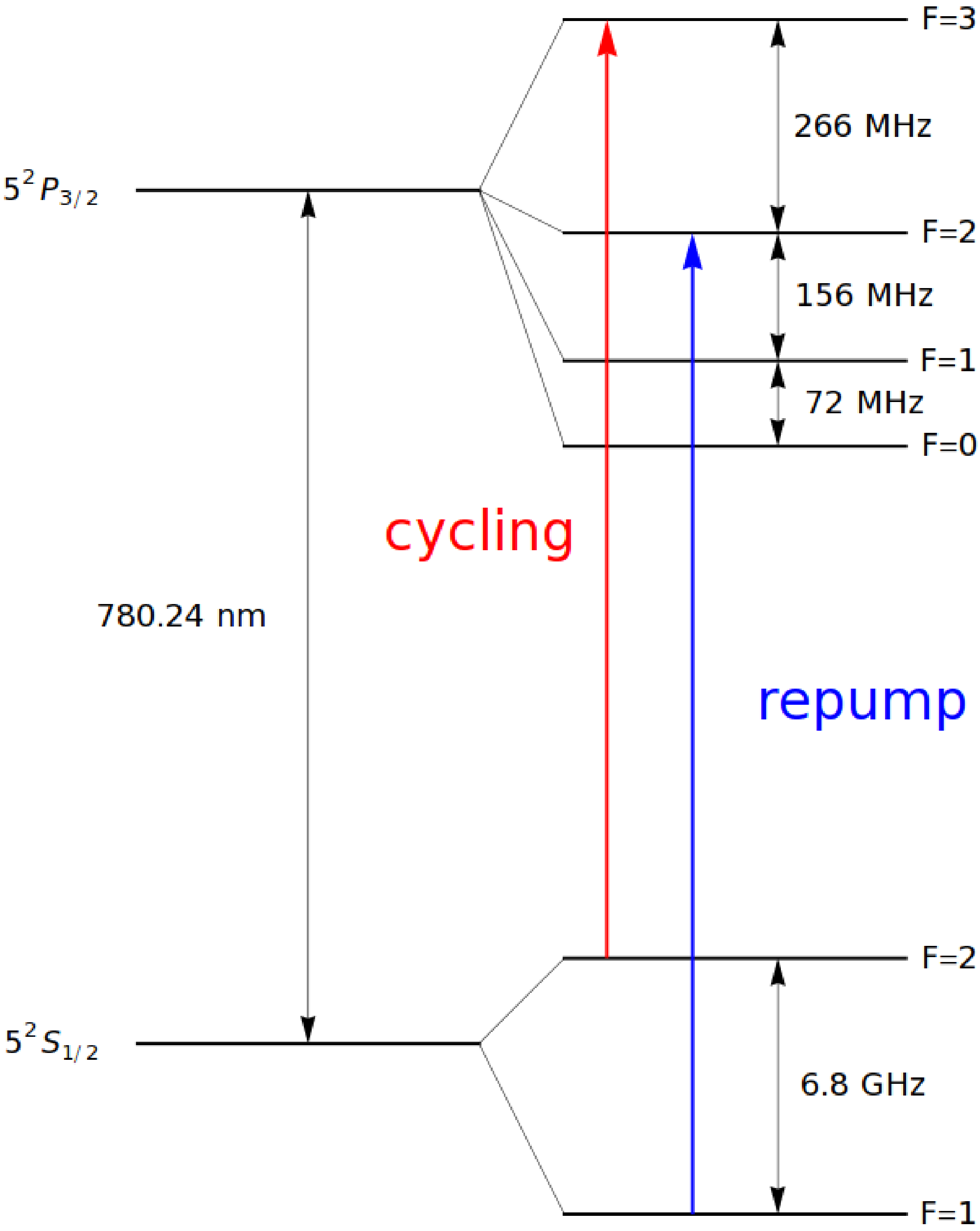

Figure 3.1: ^{87}Rb D_2 transition hyperfine structure, with frequency splittings and the cycling transition used for cooling indicated in red and the repump transition indicated in blue.

The rubidium source used in the system at the University of Queensland is that of a resistively heated alkali metal dispenser (SAES Getters). It consists of a small stainless steel container, not much thicker than a wire, which holds the rubidium. In this relatively compact source of alkali metal atoms the rubidium is in the form of a rubidium chromate with a reducing agent. Upon passing a current through the dispenser, it is heated to a threshold level of several hundred degrees Celsius, where a reduction reaction is started. Thanks to the threshold nature of this process fast switching of the atomic flux is possible. The current necessary to reach that onset of the reduction reaction is approximately 4A. After that, the flux increases with current until the limit of the dispenser is reached at approximately 10A.

This setup allows fast response times of the dispensers which can therefore be run in a pulsed mode. Typically, the dispensers are run for about 10s at a current of 7A, creating sufficient atom numbers for BEC. After turning the dispenser off the background pressure returns to the original UHV conditions within $10 - 15$s while the loading of the Magneto-Optical trap is started. More information on the dispenser system can be found in [37].

3.2 Vacuum Chamber and Atom Chip

To create a BEC an ultra high vacuum chamber is needed as every collision with background gases still at room temperature will lead to loss of rubidium atoms. In our case the science chamber is kept at a pressure below 10^{-10}mbar in order to minimize those collisions. Achieving and maintaining such low pressures is a significant challenge and the apparatus at the University of Queensland reaches those conditions. The techniques employed to achieve the necessary low pressures are described in detail in [37]. To be able to conduct the research described in this work it is necessary to keep the chamber connected to an ion pump at all times to compensate for virtual leaks, that is small amounts of gas that are trapped inside the vacuum chamber that have only a small, very low conductance path from where they are trapped to the experimental area.

Because ultra-cold atoms would heat up immediately after contact with any matter at room temperature, not only does the background gas has to be removed, but the atoms also have to be kept away from any external surfaces using the vacuum as a non-heat conducting layer of insulation. This is achieved by keeping them trapped in optical and magnetic potentials. Following a description of the atom chip which provides the magnetic fields necessary for magnetic trapping the basics of optical and magnetic trapping will be explained in later sections.

The magnetic fields used for magnetic trapping are provided by wires that are cut into a so called atomchip. Atomchips are planar devices that have wires patterned into them that carry currents to produce magnetic fields. If these magnetic fields possess local minima so called weak-field seeking states, that is states that minimize their energy when the magnetic fields are low, can be trapped in those minima. Through clever arrangements of the patterns on the chip and the switching of currents carried within these wires various potentials can be created. For a review of these devices see Fortagh *et al.* [53].

The chip used in our apparatus is an in-house design and consists of a piece of silver foil with a thickness of 125μm. The silver foil is polished to a mirror finish to be used for a surface MOT, explained in section 3.3.2, and glued onto a ceramic substrate. A schematic drawing of the chip layering is shown in Fig. 3.2. The wires are then cut into the silver foil using a CNC mill. This setup allows the trapping of atoms using modest currents of about 7A with the chip being mounted “upside down” (that is with the polished silver surface facing downwards) allowing room underneath the chip for a free-fall expansion of the atoms for imaging. A photograph of the chip before it was mounted in the vacuum cell is shown in Fig. 3.3 [37, 38].

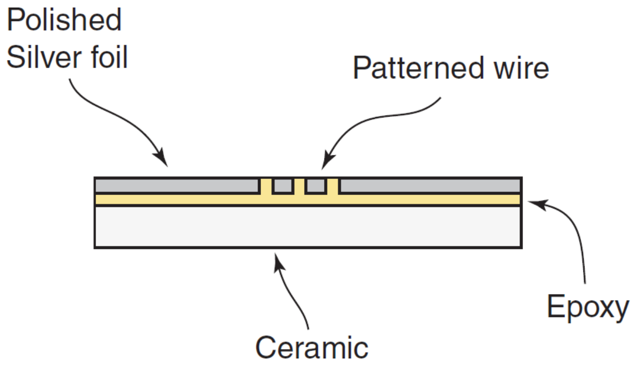

FIGURE 3.2: Schematic drawing of the layers of the UQ atom chip. A silver foil (grey) of 125μm thickness is glued onto a ceramic substrate with epoxy resin (yellow). Wires are then cut into the silver foil using a CNC mill. In the experimental setup the polished silver side will be facing down. Reproduced from [38].

The main wire on the chip is called the “Z-wire”, because its shape resembles the letter Z. When currents are passed through the Z-wire circular field lines around the wire are created. An external bias field can be used to cancel the field over a small region allowing the trapping of weak-field seekers. By choosing the strength of the bias field the distance between the chip and the trapped atom cloud can be controlled. The different fields necessary to create trapping on an atom chip are shown in Fig. 3.4 with the resulting field.

With this arrangement it is possible to create magnetic traps which can be considered harmonic for the low energy atoms used for experiments with trapping frequencies of $\omega_z = 2\pi \times 6.8$Hz along the axial dimension and $\omega_r = 2\pi \times 160$Hz in the radial dimension perpendicular to the middle segment of the Z-wire. More information on the atom chip including a characterization and technical details are found in Vale *et al.* [38].

3.3 Laser Cooling

The work horses of ultra-cold atom experiments are laser cooling techniques that use the mechanical effects of light on neutral atoms. The idea to use lasers to slow down atomic beams was first proposed in 1975 independently by Hänsch and Shawlow [54] and Wineland and Dehmelt [55]. Since then laser cooling has become a standard technique that is described in many text books (e.g. [56]). The following sections explain the principles of laser cooling which have led to the so called optical molasses, enabling the cooling of atom clouds in three dimensions. In section 3.3.2 the principles of the magneto-optical trap will be explained,

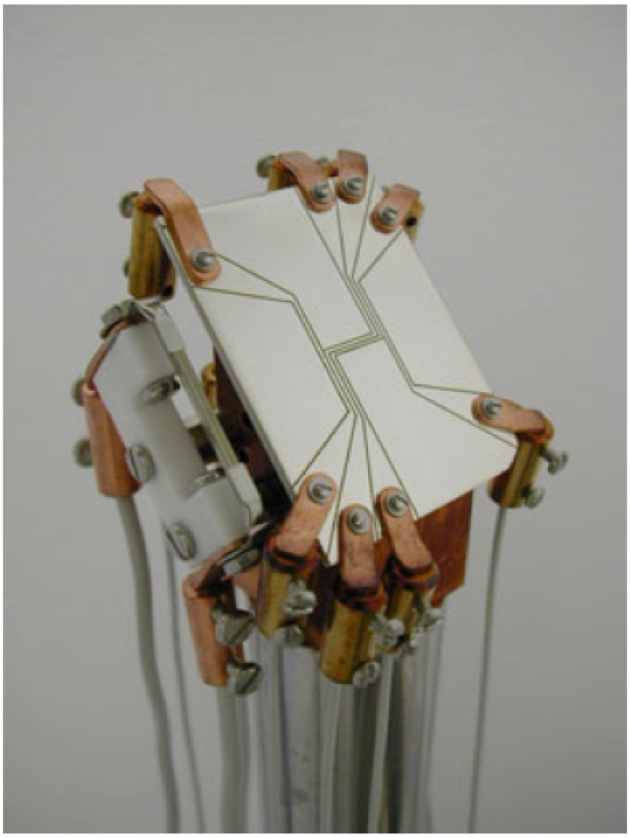

FIGURE 3.3: Photograph of the UQ atom chip before it was mounted in the vacuum cell. Clearly visible is the Z-shaped wire cut into the silver foil which creates the magnetic field used for trapping. Also shown are the copper tabs for electrical connection as well as the rubidium dispenser on the left hand side of the chip mount. Reproduced from [38].

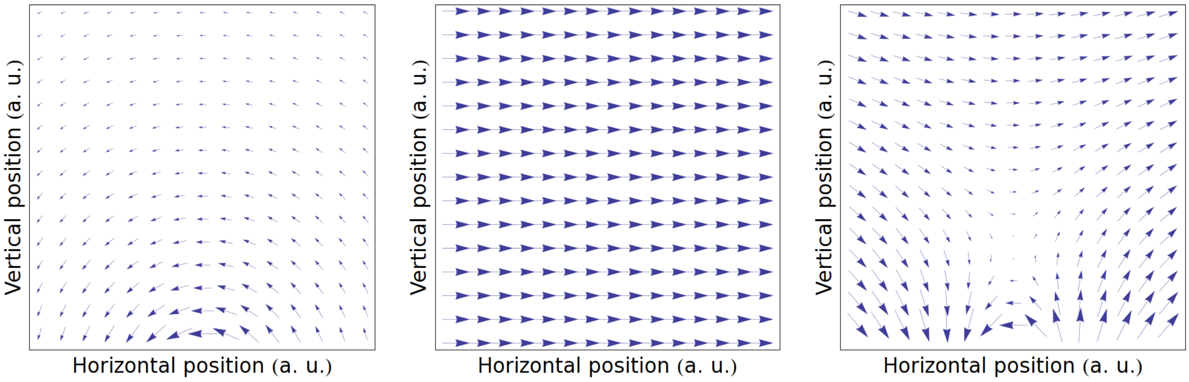

FIGURE 3.4: The total quadrupole trapping field (right) is created by the combination of the Z-wire field (left) and an external bias field (centre).

which also relies on the mechanical effects of light on neutral atoms.

3.3.1 Optical Molasses

Laser cooling relies on the radiation pressure that is exerted on atoms when they absorb light from a laser beam. An atom in its ground state travelling with a velocity v that absorbs a photon from a laser beam counterpropagating relative to its own motion is slowed by the recoil velocity $v_{\rm rec} = \hbar k/m$. Now in its excited state, the atom has to emit a photon before it is able to absorb again. Since the emission process is spontaneous rather than stimulated, the photon is emitted in a random direction with a symmetric average distribution. On average over many absorption and re-emission processes this means that the contribution from the emission averages to zero, while the contribution from the absorption gives a deceleration of $n \cdot \hbar k/m$, where n is the number of absorption and re-emission cycles. A schematic of that process is shown in Fig. 3.5.

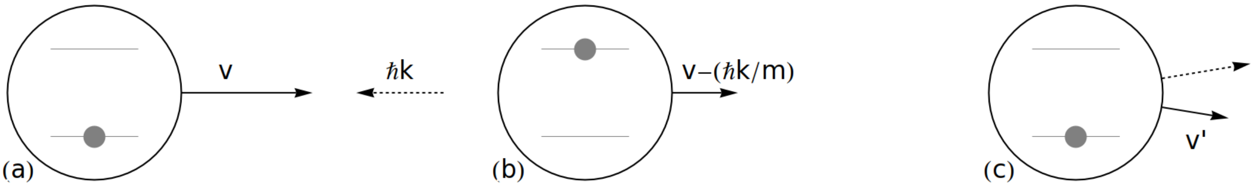

Figure 3.5: The principle of optical cooling. (a) An atom in its ground state travelling with velocity v with a counterpropagating laser beam with momentum $\hbar k$. (b) The atom absorbs a photon and is now in its excited state with its velocity reduced by $\hbar k/m$. (c) A photon is spontaneously emitted, returning the atom to its ground state generally leaving the atom with a lower velocity in the initial direction.

For ^{87}Rb, interacting with light at a wavelength of $\lambda = 780$nm, $v_{\rm rec} = 5.88$mm/s. Assuming a typical atom velocity of 10^6mm/s means that the absorption-emission cycle must occur about 1.7×10^6 times to bring an atom to complete rest.

Since rubidium is not a two level atom, but has two ground hyperfine levels ($F = 1$ and $F = 2$), laser excitation out of one hyperfine level can lead to an atom ending up in the other hyperfine level due to spontaneous decays. If this occurs the atom is no longer resonant with the laser light. The atom is therefore lost to the so called cycling transition because the linewidths of the transition and of the laser are much smaller than the ground state hyperfine separation, which in the case of ^{87}Rb is 6.8GHz. A solution to this problem is the use of a second beam, the so called repump laser, which drives a transition that returns the atoms to the initial cycling transition. In our case the cycling transition used is the $F = 2 \leftrightarrow F' = 3$ transition while the repump transition is the $F = 1 \leftrightarrow F' = 2$ transition as shown in Fig. 3.1.

For an atom travelling with velocity v to be in resonance with the incident light beam the frequency of the light has to be kv lower than the resonant frequency for an atom at rest. The light has to be red-shifted. This is due to the Doppler effect, which changes the apparent frequency for moving sources or receivers. If an atom has the right velocity to be in resonance with the incident light, it will be slowed down resulting in a change in the Doppler shift, until it is no longer in resonance with the incident light. In cases where neither the atomic resonance is tuned (by using magnetic fields) nor the laser frequency adjusted, only a certain velocity class of atoms will be addressed until that class of atoms is finally depleted.

To cool in three dimensions three mutually perpendicular pairs of red-detuned counterpropagating beams have to be set up (see Fig. 3.6). Atoms travelling towards a laser beam will see that light blue shifted, thus compensating for the initial red-shift. This means that atoms counterpropagating relative to the incident light beams will be in resonance while those copropagating will add a further red-shift moving even further out of resonance.

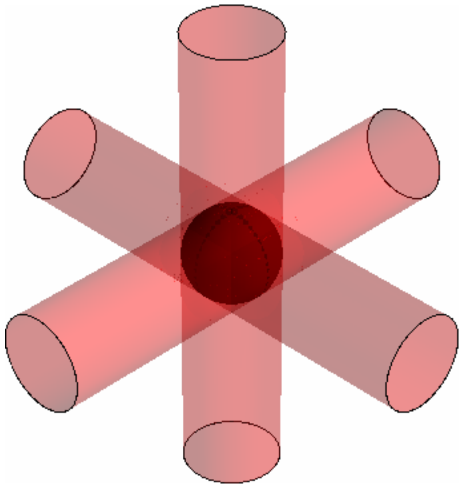

FIGURE 3.6: Three mutually perpendicular pairs of counterpropagating laser beams cooling atoms at their intersection.

The above described cooling mechanism works for atoms that are already slow enough to fall within the frequency range where the atoms are in resonance with the cooling light but ultimately reaches a temperature limit when the effects of the directional photon absorption and the non-directional photon emission by the excited atom exactly cancel. The temperature T_D when this is the case is called the Doppler cooling limit and is equal to [56]

$$T_\mathrm{D} = \frac{\hbar\Gamma}{2k_B}, \tag{3.1}$$

where Γ is the natural linewidth of the atomic transition. For ^{87}Rb the Doppler cooling limit is 146μK, which is well above the transition temperature T_c for BEC. Further cooling by optical methods is possible using other cooling mechanisms, such as Sisyphus cooling for example [57], but ultimately hits the recoil limit which stems from the momentum transfer imparted by the absorption of a single photon. Since the momentum of such a photon is $\hbar k$ and consequently its kinetic energy, referred to as the *recoil energy* $E_\mathrm{r} = (\hbar k)^2/2m$, every absorption of a photon gives rise to a thermal energy of order $T_\mathrm{r} = E_\mathrm{r}/k$. For ^{87}Rb this recoil limit is $T_\mathrm{r} = 362$nK, which is still above T_c so that other non-radiative cooling methods are necessary. One such cooling mechanism, evaporative cooling, will be explained in section 3.5.

3.3.2 Magneto-Optical Trap

The laser cooling mechanism described above only has a velocity dependent force on the atoms but not a spatially dependent one. This means that the optical molasses can only provide cooling but not trapping of neutral atoms. To achieve trapping the combined use of optical and magnetic fields is necessary. The most widely used type of trap for neutral atoms is the magneto-optical trap (MOT) which employs both optical and magnetic fields. It uses both inhomogeneous magnetic fields as well as radiative selection rules to exploit optical pumping and radiation pressure. An in depth description of MOTs can be found in [56] for example.

Trapping in a MOT works by keeping slow moving atoms in a quadrupole field that provides a linear field gradient from the origin. This ensures that together with the spontaneous light force a restoring force towards the origin acts on a wide range of atomic velocities. inhomogeneous magnetic field $B = B(z) \equiv Az$. Such a magnetic field can be produced in several ways. In our setup we first apply a magnetic quadrupole field created by external wires before moving to a so called “U-wire” MOT. In a U-wire MOT the magnetic gradient field required is produced by a wire which is bent in a “U” shape, whereas the usual arrangement for a MOT is to use external field coils in an anti-Helmholtz configuration. The external MOT coils were chosen for initial capturing of atoms as the field minimum can be positioned a relatively large distance from the mirror surface of the chip, thus allowing for a larger capturing region. The fields are produced by modest currents of about 8A, creating field gradients of 19 G/cm in the axial and 9.8 G/cm in the radial direction. After the MOT has been created using the external MOT coils the current through the MOT coils is ramped down while the current through the U-wire and bias coils is ramped on leading to a compression of the MOT. Limited by the heat conduction of the U-wire, a current of 20A can be passed through the U-wire for less than 5s. Together with a pair of bias coils in a Helmholtz configuration, with a current of 1.1A which produces a bias field of 10G, the U-wire current is sufficiently high to produce a steep quadrupole field with a field minimum 3mm from the centre of the wire [37]. A fluorescence picture of a U-wire MOT with approximately 3×10^7 atoms is shown in Fig. 3.7. To take the picture an image is taken while the MOT and repump lasers are on. The light scattered by the atoms during the trapping and cooling process is enough to get a fluorescence image of the atom cloud.

To understand the principle of the MOT it is easiest to look at the 1D case which can then be extended to three dimensions by analogy. This case is depicted in Fig. 3.8. In a simple atomic scheme where a transition from a ground state with $F_g = 0$ to an excited state with $F_e = 1$ is used, the degeneracy of the m_F sublevels will be lifted in the presence of a magnetic field. Due to the Zeeman effect the excited state will then have three components which can be addressed by beams of differing circular polarization. Due to the selection rule that $\Delta m_F = +1$ (-1) for σ^+ (σ^-) light beams the atoms will have a preferred direction they absorb photons from. This is shown in Fig. 3.9.

In addition, due to the presence of the magnetic field, the laser beams will be detuned by δ from the zero field atomic resonance. Due to the Zeeman shift the excited state with

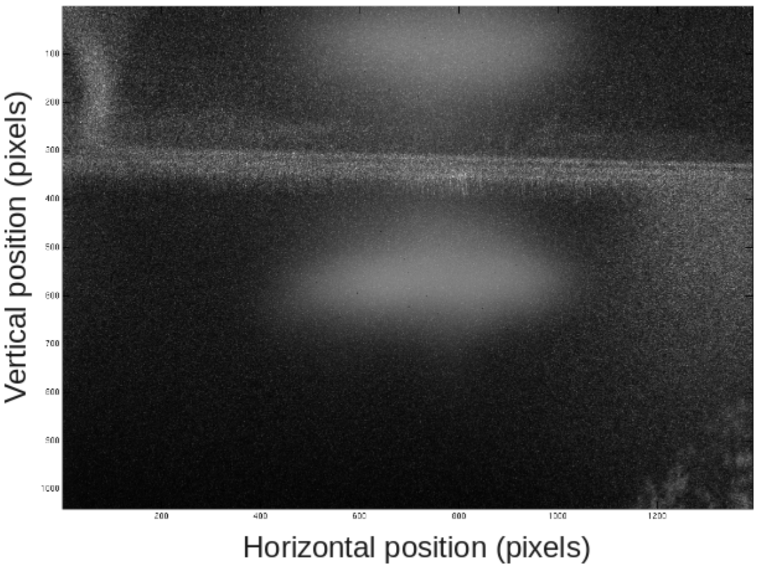

Figure 3.7: Fluorescence image of the U-wire MOT with approximately 3×10^7 atoms. Also visible is the reflection of the MOT on the chip surface (top part of the image) and the light reflected off the wires on the chip. The width of one pixel is 4.7μm.

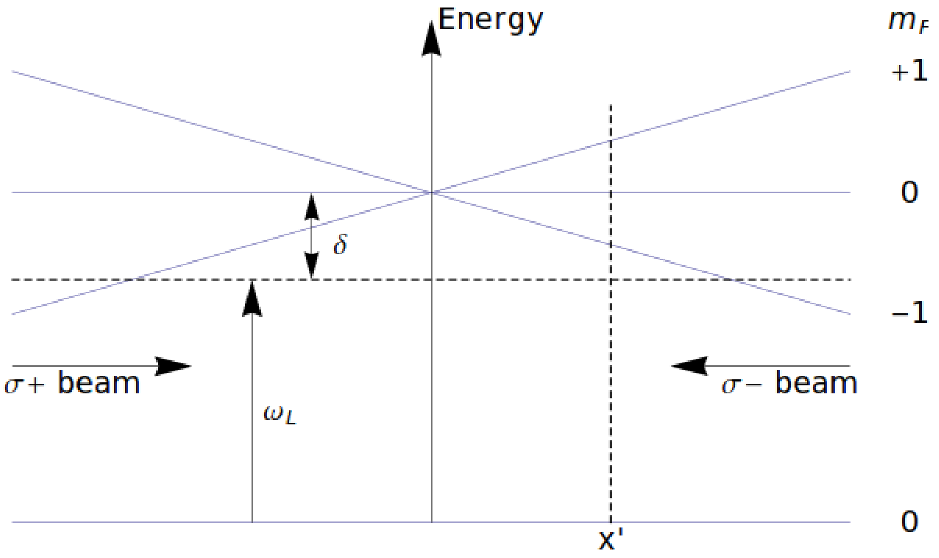

Figure 3.8: Arrangement for a MOT in 1D. The horizontal dashed line represents the laser frequency seen by an atom at rest in the centre of the trap. An inhomogeneous field causes a Zeeman splitting such that atoms at $x = x'$ are more in resonance with the σ^- beam incident from the right hand side than the σ^+ beam. This leads to a force on the atoms towards the centre of the trap.

$m_F = +1$ will be shifted up for $B > 0$ while the state with $m_F = -1$ is shifted down and the the state with $m_F = 0$ remains unchanged. By changing δ the x-position where the atom comes into resonance with the light field can be tuned, effectively choosing a capture area for the MOT. Should the arrangement be chosen such that the incident beam from the right

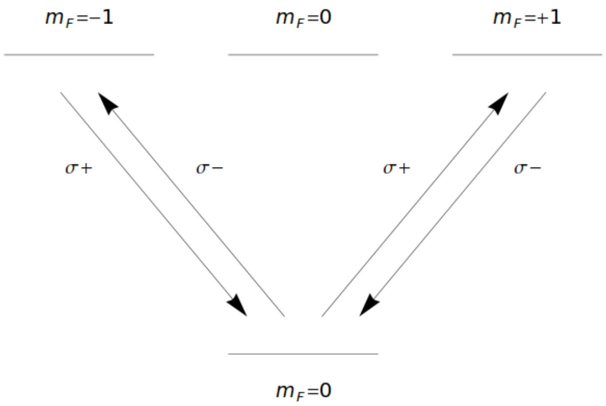

FIGURE 3.9: Allowed transitions for σ^+/σ^- polarized light, based on the fact that for σ^+ (σ^-) light $\Delta m_F = +1$ (-1) to conserve angular momentum.

is σ^- polarized (and the incident beam from the left σ^+ accordingly) then more light will be scattered from the σ^- beam effectively pushing the atoms to the left should an atom be to the right of the field zero crossing as depicted in Figure 3.8.

This situation creates a position dependent force field, creating compression. In addition, since the laser light is detuned below the atomic zero field resonance cooling takes place at the same time as explained in section 3.3.1. By using three pairs of perpendicular beams instead of one pair the scheme is easily extended to three dimensions.

Because of the atomchip an arrangement where the MOT beams are provided by six independent counterpropagating beams that are pairwise orthogonal, as shown in Fig. 3.6, is not possible. Instead a so called surface or mirror MOT arrangement is used. In that case one pair of counterpropagating beams propagates below the chip surface, while another pair of beams is reflected off the chip surface. If one of the laser beams reflected off the chip is σ^+ polarized while the other is σ^- polarized the six counterpropagating beams are realized as shown in Fig. 3.10.

3.4 Magnetic Trapping

In order to circumvent the Doppler and recoil cooling limits of laser cooling of atomic samples explained in detail in section 3.3.1, non-radiative cooling mechanisms are needed. One such mechanism is evaporative cooling. While the main purpose of magnetic traps is to provide confinement for the atomic cloud it is also used to provide a dark trapping of pre-cooled atoms and compression in order to achieve high collision rates for effective evaporative cooling. Magnetic trapping was first achieved in 1985 in the group of W.D. Phillips [58] and since then it has become a standard technique in the production of Bose-Einstein condensates.

The following section will describe the principles of magnetic trapping and show some measurements taken with the apparatus at the University of Queensland.

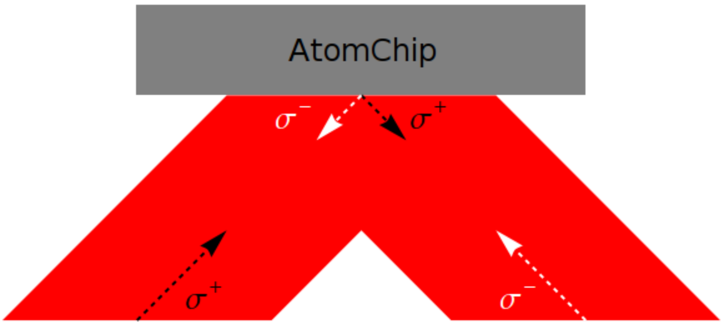

FIGURE 3.10: Schematic drawing of the beam arrangement for a surface or mirror MOT. The arrangement ensures that there is a pair of σ^+/σ^- beams in every direction provided that there is one pair of counterpropagating beams underneath the chip perpendicular to the beams reflected off the mirror surface.

3.4.1 Principles Of Magnetic Trapping

The interaction of a magnetic dipole with external fields is given by [59]

$$\vec{U}_{\text{mag}} = -\vec{\mu}_m \cdot \vec{B} = -\mu_m B \cos\theta, \tag{3.2}$$

where $\vec{\mu}_m$ is the magnetic dipole moment of the atom and $\vec{B}$ describes the external field and θ is the angle between the magnetic moment and the external field. The magnetic moments for atoms with an unpaired electron, such as alkali atoms, are of the order of a Bohr magneton. In a classical description θ is constant due to the rapid precession of μ_m around the magnetic field axis. In a quantum mechanical description, however, the energy levels in an atom are given by the Zeeman splitting

$$E(m_F) = g\mu_B m_F B, \tag{3.3}$$

where g is the g-factor and m_F the quantum number of the z-component of the angular momentum F. This means that the classical term $\cos\theta$ has to be replaced by a factor m_F/F. The classical picture of a constant angle θ is now equivalent to the system remaining in one well defined m_F quantum state.

Due to the fact that Maxwell's equations do not allow magnetic field maxima in free space, atom traps require a local minimum of the magnetic field strength. It also means that only certain m_F states can be trapped in magnetic traps. These states are called weak-field seekers and in the case of ^{87}Rb these would be the states with $F = 1$ and $m_F = -1$ and $F = 2$, $m_F = 2$.

3.4.2 The Magnetic Trap At UQ

With our apparatus we routinely generate magnetic trapping of samples down to Bose-Einstein condensation temperatures. Fig. 3.11 shows a fluorescence image of a MOT with approximately 3×10^7 atoms and an absorption image of a magnetic trap with approximately 6×10^6 atoms shortly after they have been transferred from the MOT to the magnetic trap. The two distinct spots that can be seen in both images are the imaged cloud itself (bottom) and its reflection off the atom chip. The top image of the magnetic trap was taken using absorption imaging explained in detail in section 3.6, while the bottom image of the MOT was taken using fluorescence imaging where the light of the MOT beams scattered off the atoms is captured on a CCD camera. Also shown are the density cross sections of MOT and magnetic trap. No evaporative cooling has been applied to the magnetic trap shown. The life time of the atoms in the magnetic trap is sufficient to apply evaporative cooling through the BEC transition. Shown in Fig. 3.12 is a measurement of the lifetime in the magnetic trap with a $1/e$ lifetime of 11s. The lifetime was determined by measuring the number of atoms in the magnetic trap after a number of varying hold times and fitting an exponential decay curve, where the time constant of the decay is taken to be the lifetime.

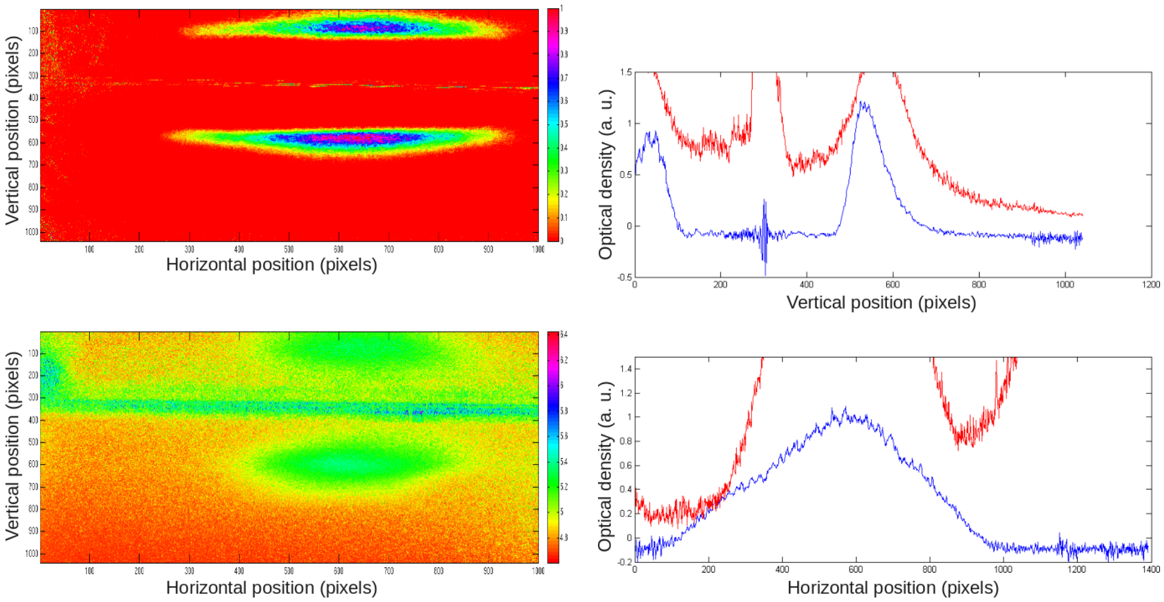

Figure 3.11: Fluorescence image of a MOT with approximately 3×10^7 atoms (top left) and absorption image of a magnetic trap with approximately 6×10^6 atoms (bottom left). The two visible spots in both pictures are the atom cloud itself (bottom) and its reflection off the atom chip (top). On the right hand side vertical (top) and horizontal (bottom) cross sections are shown which combine information from both images shown on the left in one graph with the fluorescent light intensity of the MOT shown in red and the optical density of the magnetic trap shown in blue. The width of one pixel is 4.7μm.

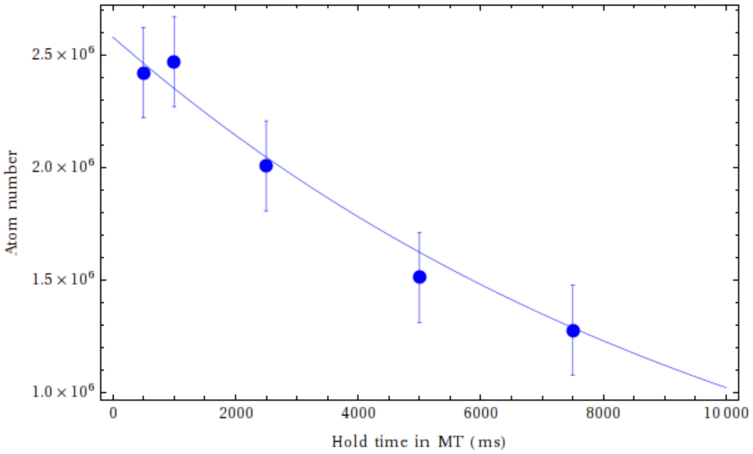

FIGURE 3.12: Lifetime measurement in the magnetic trap. The trap has a $1/e$ lifetime of 11s.

3.5 Evaporative Cooling

Since laser cooling reaches physical limits, ultimately the recoil limit, which for ^{87}Rb is 362nK, non-radiative cooling mechanisms are necessary to further cool samples pre-cooled by laser cooling. One such mechanism is evaporative cooling.

The idea behind evaporative cooling is to selectively remove atoms with an energy higher than the average energy of the sample. The selective removal can be done by lowering the depth of the trap, therefore allowing higher energy atoms to escape while atoms with an energy lower than the trap depth will remain trapped. Elastic collisions in the trap can then lead to a rethermalization of the sample which will lead to a lower average temperature. Figure 3.13 shows the Maxwell-Boltzmann distribution for different temperatures where the probability to find particles with a certain kinetic energy is plotted as a function of particle energy for different temperatures. It can be seen that lower temperatures have the probability maximum at lower kinetic energies, meaning that the temperature can be reduced by cutting off the high energy tail of the distribution and successive rethermalization.

In our experiment the atoms are trapped in a magnetic trap. To lower the trap depth it would be possible to reduce the magnetic field strength. However, reducing the magnetic field strength with the precision necessary for evaporative cooling is a hard task. Therefore, we use the so called rf-knife technique [60]. Since the degeneracy of different m_F sublevels is lifted in a magnetic field and since only some states are trapped it is possible to selectively flip the spin state of an atom from a trapped state to an untrapped state based on its kinetic energy as depicted in Figure 3.14. The figure shows the three different m_F sublevels that exist for atoms in an $F = 1$ state with their degeneracy lifted by a magnetic field. An initial radio frequency ω_i is on resonance with the $m_F = -1 \rightarrow m_F = +1$ hyperfine transition flipping atoms with enough energy from the trapped $m_F = -1$ to the untrapped $m_F = +1$ state. The frequency is then lowered in a frequency sweep to a final radio frequency of ω_f which determines the lowest energy of atoms that will be transferred to the untrapped state. This process allows cooling below the critical temperature of Bose-Einstein condensation.

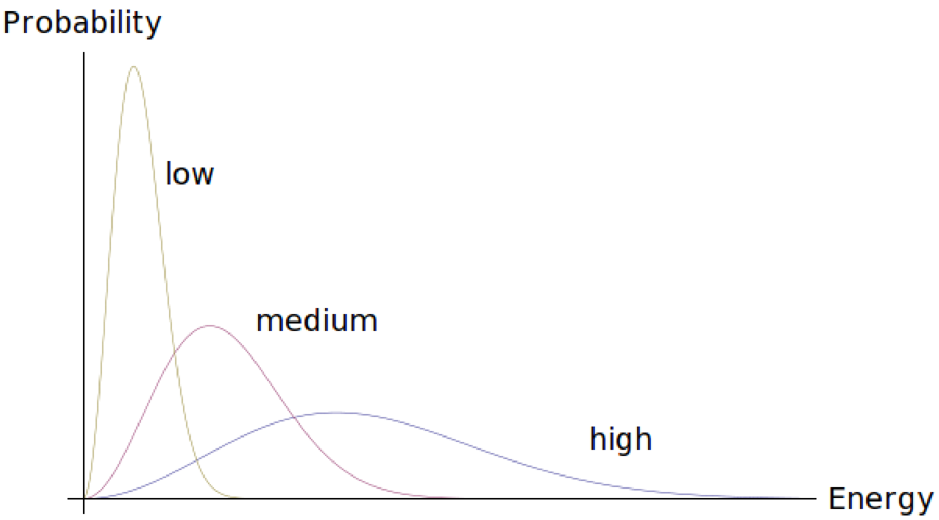

FIGURE 3.13: Maxwell-Boltzmann distribution showing the energy dependence of the probability to find a particle with a certain energy for different temperatures (labeled as "low", "medium" and "high").

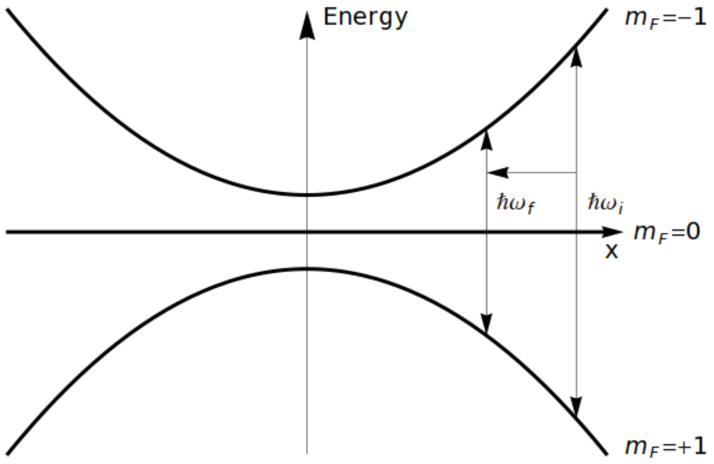

FIGURE 3.14: Energy in a harmonic trap for different m_F sublevels. Indicated is the rf-frequency sweep that selectively removes particles with an energy higher than the rf-cut off energy $\hbar\omega_\mathrm{f}$.

3.6 Imaging

To obtain information about Bose gases they have to be probed in some way. Contact probes cannot be used because of the small size of the sample as well as the very cold temperatures these samples are at which would heat up immediately upon contact with any room temperature (or even liquid nitrogen temperature) probe. To get around this the absorption of resonant light is used to cast a shadow onto a CCD camera from which information about the sample can be inferred. To reduce the effects of noise a sequence of three images is taken. One image is taken while the imaging beam is turned on and has the shadow cast by the atomic cloud in it. A second image is taken with the imaging laser on but without the atoms present and a third image is taken with all laser light sources turned off so as to account for the electronic dark noise produced by the camera. The final image is then calculated as

$$I = \frac{A_{\text{with}} - B}{A_{\text{without}} - B}, \tag{3.4}$$

where A_i are arrays containing the intensity distribution with and without the atoms present and B is the intensity array of the dark image. The sequence of images taken are shown together with the processed image in Fig. 3.15.

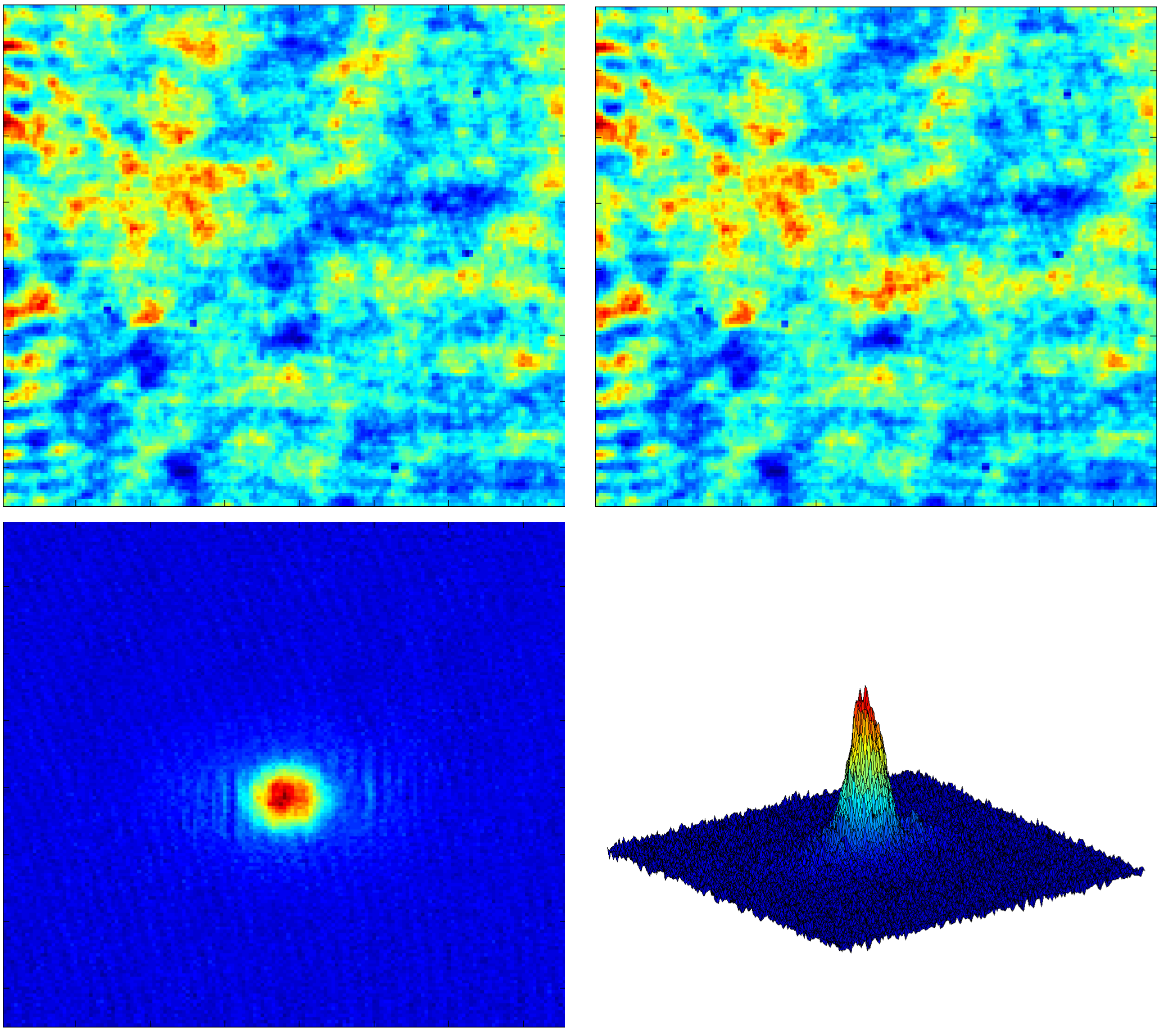

FIGURE 3.15: Series of images taken to gain information about the atomic cloud through absorption imaging. One picture contains the shadow cast by the atom cloud (top left) and one has the laser light on but no atoms present (top right). A third picture shows the processed image of a BEC with thermal cloud (bottom left) and a fourth picture shows a 3D rendering of that processed image (bottom right).

To get information about atom number, temperature and condensate fraction it is necessary to fit a bimodal distribution to the atom cloud after a time-of-flight where all trapping potentials are switched off. The time-of-flight is necessary because the features that are to be observed are often too small to be resolved directly. Giving the atom cloud time to expand enlarges the cloud as well as many of the observable features making optical probing possible. The bimodal fit is necessary to get information about both parts of the atomic cloud, the thermal atoms as well as the condensate atoms.

Thermal atoms above the BEC transition temperature have a time-of-flight density distribution that is described by [59]

$$n_{\mathrm{tof}}(\mathbf{r},t) = \frac{1}{\lambda_{\mathrm{dB}}} g_{3/2}\left(\exp\left(\frac{\mu - mr^2/2t^2}{k_B T}\right)\right), \tag{3.5}$$

where λ_{dB} is the thermal de Broglie wavelength of the atoms and $g_{3/2}(z)$ is the Bose function $g_j(z) = \sum_i z^i/i^j$. It can be seen that the density distribution has a Gaussian shape that depends on the temperature T. The temperature can therefore be calculated by fitting a Gaussian shape to the thermal fraction of the atom cloud.

According to the Thomas-Fermi approximation described in section 2.2.1 the shape of the atom cloud at zero temperature follows the shape of the trapping potential. For most traps this shape can be approximated by a harmonic trap resulting in an inverse parabola. Fitting an inverse parabola to the condensate atoms and comparing the number of atoms in the parabola and the Gaussian thermal cloud, the condensate fraction can be calculated. Figure 3.16 shows the processed image of a BEC with thermal background together with a cross section through the atom cloud with the bimodal function fitted.

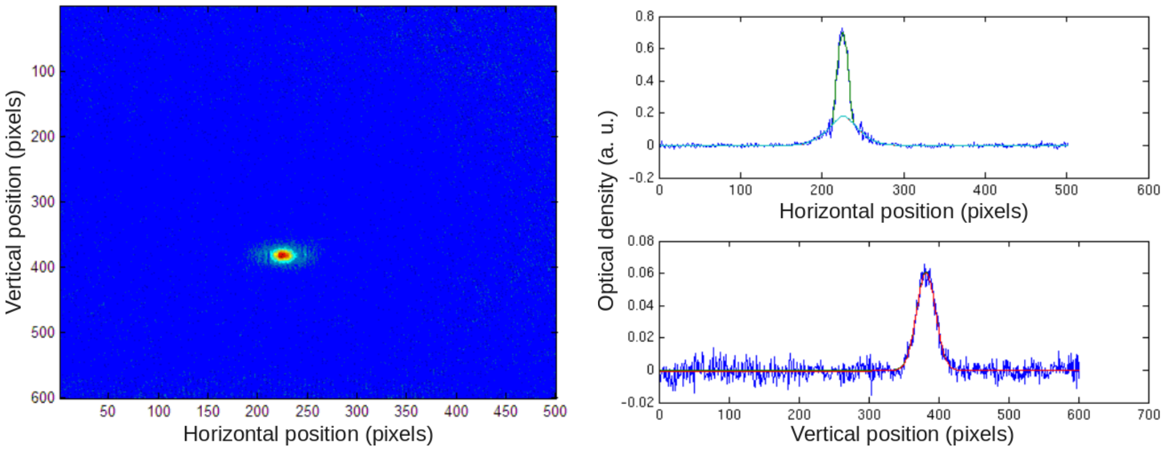

FIGURE 3.16: Processed image of a BEC with thermal cloud (left) and cross section through the atom cloud with the bimodal fit used to determine temperature and condensate fraction (right). In the horizontal cross section the dark blue line shows the data points, while the cyan line shows a Gaussian fit to determine the thermal background and the green line shows an inverse parabola fit to the BEC. In the vertical cross section the blue line shows the data points, while the red line shows a Gaussian fit to the data. The size of one pixel is 4.7μm.

To implement the absorption imaging the atoms are pumped into the ground state of the cycling transition ($F = 2$) using the repump laser while it is simultaneously illuminated with a resonant light beam pointing straight at the camera, the duration of the imaging pulse being on the order of 60μs. Where the beam hits the atom cloud photons will be absorbed and re-emitted into a solid angle of 4π leaving a shadow on the CCD camera provided that the CCD camera is not saturated. After that a "background" image is taken without any atoms present so that the optical density can be calculated.

In our apparatus the atoms are imaged by a lens of diameter of 25mm placed at a distance of 100mm from the atom cloud. Given a numerical aperture of $NA = 0.13$, the resolution of the system defined as the minimum separation that two points need to have to still be resolved as individual points is $0.61 \times \lambda/NA = 4\mu$m. Since the pixel size of our camera is 4.7μm $\times 4.7\mu$m and the fact that a dark pixel is required between any two bright pixels, features have to be of the size of $\approx 10\mu$m to be resolved by our system. More information on the imaging system can be found in [39].

4

Optical Trapping

Methods for storing particles have often served as key points in experimental progress. Trapping particles allows one to spend more time probing or manipulating them than would be possible for an untrapped particle. For charged particles such as ions the strong Coulomb interaction can be used to trap particles in electric or electromagnetic fields. For neutral atoms this is not possible. Nonetheless, it has become experimentally routine to prepare samples in the microkelvin regime where the remaining kinetic energy of particles is low enough so that weaker mechanisms than the strong Coulomb interaction can be used for trapping. Those mechanisms include radiation-pressure traps such as the MOT described in section 3.3.2 and magnetic traps which have been covered in section 3.4. A third option that will be discussed in more detail in this chapter is the use of the optical dipole force for trapping. Traps that rely on the optical dipole force were pioneered by Arthur Ashkin, who was the first to report the detection of gradient forces in 1970 [61]. Since then a whole new field has emerged with so called optical tweezers, that is apparatuses that allow the manipulation of transparent objects up to tens of micrometers in size without physically touching a sample. This has also led to the use of gradient forces of light in the manipulation of cold atom samples.

Optical dipole traps rely on a induced electric dipole interaction with far-detuned light, a mechanism that is much weaker than the mechanisms mentioned above. Typically traps have a depth below one millikelvin. The far-detuning ensures that the optical excitation is kept extremely low such as not to suffer from the same light induced processes such as photon scattering for example that limit the use of radiation-pressure traps. In those the single-photon recoil energy limits the temperature to 362nK for ^{87}Rb which is above the BEC transition temperature T_c.

The main focus of this chapter will be the presentation of the scanning beam trap developed at the University of Queensland as part of this project. The scanning beam trap allows us to create nearly arbitrary two-dimensional potential landscapes which can be either static or dynamic depending on the experimental requirements. The trap uses a two-dimensional AOM to spatially scan a tightly focused laser beam that attracts atoms to its focus. When moved slowly the atoms can be made to adiabatically follow the path of the laser beam for transport purposes. Rather than using the trap to move atoms the scanning beam trap has focused on the rapid scanning of a laser beam which means that the atoms experience a time averaged potential that depends on the scanned beam path. The initial motivation for the development of the scanning beam trap was the desire to create ring traps which can be created by scanning the beam in a circular path. In those ring traps we would be able to create persistent currents, which have been observed in superfluid helium and which could help to further the understanding of superfluidity in BEC. Unfortunately, due to restrictions on the optical access in our BEC setup it was not possible to follow this research idea. Nevertheless, we decided to proceed with the development and study of the scanning beam trap, as through its versatility the scanning beam trap can be used for other interesting research. In our case the trap turned out to be perfectly suited to create line traps with a moving obstacle which can be used to study the critical velocity of superfluidity in BEC. The progress on this research will be presented in Chapter 6. Also several other research ideas using the scanning beam trap have been proposed such as the controlled creation of vortices [62] or the use in a quantum information protocol using Rydberg atoms [63]. We are convinced that through its versatility it will find many more uses in cold atom research in the future.

This chapter will proceed as follows. First, the optical dipole force will be explained which provides the physical mechanism behind optical trapping. Then, the explanation of the optical dipole force will be followed by a section on the propagation of Gaussian laser beams in free space as well as through lens systems. This is because the basis of the optical traps is formed by a Gaussian laser beam that needs to be shaped according to the experimental requirements. In a third section the actual trap designs for the two optical dipole traps used in the experiments will be presented. I will present details on the optical dimple trap used for experiments on condensate formation and rethermalization presented in Chapter 5 of this thesis, followed by details of the scanning beam trap.

4.1 Dipole Force

Neutral atoms interact with light fields in a conservative as well as a dissipative way. The dissipative interaction stems from atoms first absorbing and subsequently spontaneously emitting photons. As opposed to the absorption, the spontaneous emission of photons has no preferred direction so that after a couple of cycles of absorption and emission a mean momentum transfer in the direction of the $\vec{k}$-vector of the incident light field takes place, leading to a dissipative force on the atoms as used in the MOT and optical molasses. The conservative part of the interaction stems from an induced dipole moment in the atom which interacts with the intensity gradient of the inducing field. The semi-classical oscillator model offers a good description of this process.

4.1.1 The Oscillator Model

If an atom, here described by a two-level system, is placed in a light field, described by the classical field vector $\vec{E}$, the field will induce an atomic dipole moment $\vec{d}$ which is driven with the frequency ω of the light field. The amplitude of the dipole moment is then connected to the amplitude of the driving field via [64]:

$$\vec{d} = \alpha(\omega)\vec{E}. \tag{4.1}$$

In this equation $\alpha(\omega)$ describes the complex polarizability of the atom which is dependent on ω. Using this the interaction potential can be written as

$$U_{dip} = -\frac{1}{2}\langle d\vec{E}\rangle = \frac{1}{2\epsilon_0 c}\Re(\alpha)I, \tag{4.2}$$

where the angle brackets denote the time average over fast oscillating terms. The factor of 1/2 in Eqn. (4.2) accounts for the fact that we are dealing with an induced rather than a permanent dipole moment and the field irradiance can be written as $I = 2\epsilon_0 c|E|^2$. From this it can be seen that the potential is directly proportional to the irradiance I as well as the real part of α, which describes the in-phase component of the dipole oscillation. The dipole force can now be written as the gradient of a potential [64]

$$\vec{F}_{\mathrm{dip}}(\vec{r}) = -\nabla U_{\mathrm{dip}}(\vec{r}) = \frac{1}{2\epsilon_0 c}\Re(\alpha)\nabla I(\vec{r}). \tag{4.3}$$

The scattering rate on the other hand is proportional to the imaginary part of the polarizability and is given by

$$\Gamma_{\mathrm{Sc}} = -\frac{\langle d\vec{E}\rangle}{\hbar\omega} = \frac{1}{\hbar\epsilon_0 c}\Im(\alpha)I(\vec{r}). \tag{4.4}$$

To calculate the polarizability α we make use of Lorentz' ansatz of a classical damped oscillator with resonance frequency ω_0 and damping rate Γ_{damp}:

$$\alpha(\omega) = 6\pi\epsilon_0 c^3 \frac{\Gamma_{\mathrm{damp}}/\omega_0^2}{\omega_0^2 - \omega^2 - \imath(\omega^2/\omega_0^2)\Gamma_{\mathrm{damp}}}. \tag{4.5}$$

Another approach to calculating the polarizability uses a semi-classical approach in which the atom is described as a two-level system. Ignoring saturation effects this approach yields the same result that is given by the classical calculation. In this case it has to be noted that the damping rate has to be calculated as the dipole matrix element between the ground and the excited state [64]

$$\Gamma_{\mathrm{damp}} = \frac{\omega_0^3}{3\pi\epsilon_0\hbar c^3}|\langle e|\mu|g\rangle|^2, \tag{4.6}$$

where μ is the dipole operator $\mu = -q_{\mathrm{e}} r$, with q_{e} the electric charge of an electron. It is interesting to note that this equation is true for every neutral particle in an oscillating electric field. Henceforth looking at the case of far detuned light fields with a low saturation and therefore low scattering rate, means that Eqn. (4.5) is a good approximation. For this case the dipole potential and scattering rate can be written as [64]

$$U_{\mathrm{dip}}(\vec{r}) = -\frac{3\pi c^2}{2\omega_0^3}\left(\frac{\Gamma}{\omega_0 - \omega} + \frac{\Gamma}{\omega_0 + \omega}\right) I(\vec{r}) \tag{4.7}$$

$$\Gamma_{\mathrm{Sc}}(\vec{r}) = \frac{3\pi c^2}{2\hbar\omega_0^2}\left(\frac{\omega}{\omega_0}\right)^3 \left(\frac{\Gamma}{\omega_0 - \omega} + \frac{\Gamma}{\omega_0 + \omega}\right) I(\vec{r}). \tag{4.8}$$

$\Gamma = 1/\tau$ in this case describes the lifetime of the atomic energy level. Using the rotating-wave approximation [65], which transforms into a frame of reference rotating with the coordinate system, one can on average neglect the fast oscillating counter-rotating terms, leading to [64]

$$U_{\mathrm{dip}}(\vec{r}) = \frac{3\pi c^2}{2\omega_0^3}\frac{\Gamma}{\Delta} I(\vec{r}) \tag{4.9}$$

$$\Gamma_{\mathrm{Sc}}(\vec{r}) = \frac{3\pi c^2}{2\hbar\omega_0^2}\left(\frac{\Gamma}{\Delta}\right)^2 I(\vec{r}), \tag{4.10}$$

where $\Delta = \omega - \omega_0$. Dividing Eqns. (4.9) and (4.10) gives a simple relationship between the dipole potential and the scattering rate

$$\hbar\Gamma_{\mathrm{Sc}} = \frac{\Gamma}{\Delta} U_{\mathrm{dip}}. \tag{4.11}$$

In summary to this part it should be pointed out that this leads to two major design considerations for optical traps

1. *Sign of the detuning:* Light with a wavelength longer than that of the atomic resonance (red detuned, $\Delta < 0$) results in the sign of the potential being negative and therefore leads to an attractive potential while light with a wavelength shorter than that of the atomic resonance (blue detuned, $\Delta > 0$) creates a repulsive potential. In the case of a red detuned beam the atoms will therefore feel a force towards the maximum intensity of the light field.

2. *Intensity vs. scattering:* Since the dipole potential scales as I/Δ while the scattering rate scales as I/Δ^2, it is desirable to work with large detunings compensating for the lower potential depth with higher field intensities. This will minimize losses due to light scattering while providing a sufficiently deep potential.

4.1.2 Dressed State Description

An alternative option is to describe the two-level atom together with a quantized light field. This has become known as “dressed state” picture which is described in more detail in [66]. Starting from a two-level atom with energy $|g\rangle = 0$ in its ground state and energy $|e\rangle = \hbar\omega_0$

in its excited state, where ω_0 is the atomic resonance frequency, and a light field with n photons, which each add an energy $\hbar\omega_l$, where ω_l is the frequency of the light field, therefore possessing a total energy $(n+1/2)\hbar\omega_l$, the energy for the uncoupled system is simply the sum of the two energies. The hamiltonian of the atom can be written as $H_{\mathrm{A}} = \hbar\omega_0|e\rangle\langle e|$, while the hamiltonian for the light field has the form $H_{\mathrm{L}} = \hbar\omega_l(a^\dagger a + 1/2)$, where $a^\dagger$ and a are the usual creation and annihilation operators. The hamiltonian for the uncoupled system can therefore be written as

$$\tilde{H} = H_{\mathrm{A}} + H_{\mathrm{L}}. \tag{4.12}$$

Taking the interaction between the atom and the light field into account adds another term, H_{AL}, describing the atom-light interaction to the hamiltonian (4.12) such that

$$H = H_{\mathrm{A}} + H_{\mathrm{L}} + H_{\mathrm{AL}}. \tag{4.13}$$

This interaction can be modelled as a dipole, resulting in $H_{\mathrm{AL}} = -\vec{d}\vec{E}_l$, where $\vec{d}$ is the dipole operator and $\vec{E}_l = \sqrt{\frac{\hbar\omega_l}{2\epsilon_0 V}}\vec{\epsilon}_l(a + a^\dagger)$ describes the quantized field with ϵ_0 the vacuum permittivity, V the mode volume and $\vec{\epsilon}_l$ the laser polarization.

The interaction term leads to a shift in the atomic eigenstates which are now given by a linear combination of the original eigenstates $|g\rangle$ and $|e\rangle$. The new eigenstates of the system are now [66]

$$|1, n-1\rangle = \cos\theta|e, n-1\rangle + \sin|g, n\rangle, \tag{4.14}$$

$$|2, n-1\rangle = -\sin\theta|e, n-1\rangle + \cos|g, n\rangle, \tag{4.15}$$

with θ describing the mixing angle which is determined by the Rabi frequency and the detuning between ω_l and ω_0.

Using a multi-level atom in the hamiltonian 4.13 instead of a two-level system and applying second order perturbation theory results in a matrix element for the energy shift of the i-th state (when the unperturbed energy level is $\mathcal{E}_i$) given by [64]

$$\Delta E_i = \sum_{i \neq j} \frac{|\langle j|H_{\mathrm{AL}}|i\rangle|^2}{\mathcal{E}_i - \mathcal{E}_j} \tag{4.16}$$

for the two-level atom this can be simpyfied to [66]

$$\Delta E = \pm\frac{|\langle e|\mu|g\rangle|^2}{\Delta}|E|^2 = \pm\frac{3\pi c^2}{2\omega_0^3}\frac{\Gamma}{\Delta}I, \tag{4.17}$$

where Eqn. (4.6) was used and the plus (minus) sign in the equation is describing the ground (excited) state. Comparing this result to Eqn. (4.9) it can easily be seen that the result is equal to that given by the semi-classical approach, when assuming an effective dipole potential $U_{\mathrm{dip}} = \Delta E$.

4.2 Propagation Of Gaussian Beams

To describe the optical system used in the setup it is first necessary to introduce the concept of Gaussian beams and their propagation. Using these concepts it is possible to calculate the most important properties of laser beams such as beam size, focal position or intensity distribution. A detailed explanation can be found in [67].

A Gaussian beam is a solution to the Helmholtz equation

$$\frac{\partial^2 E_i}{\partial x^2} + \frac{\partial^2 E_i}{\partial y^2} - 2\imath k \frac{\partial E_i}{\partial z} = 0 \tag{4.18}$$

in the paraxial approximation ($|\partial E_i / \partial z^2| \approx 0$).

Assuming that the beam is propagating along its z-axis, and at its focal position has a diameter of $2w_0$ and a wavefront radius $R_0 = \infty$, then the propagation of the beam can be fully described by the complex beam parameter $q(z)$, a complex number that allows the calculation of the beam properties at any given point along its propagation through an optical system, provided that the initial beam parameter is known. The width w_0 is called the "beam waist".

The evolution of the complex beam parameter can be derived as follows [67]. Considering a uniform spherical wave with wave vector $k = 2\pi/\lambda$,propagating from a source with coordinates x_0, y_0, z_0 which is observed at the coordinates x, y, z, where the distance $z - z_0$ between the source and the observation point is sufficiently large, the field at the observation coordinates can be written as

$$\begin{aligned} u(x, y, z) = & \frac{1}{z - z_0} \exp\left[-\imath k \frac{(x - x_0)^2 + (y - y_0)^2}{2(z - z_0)}\right] = \\ & \frac{1}{R(z)} \exp\left[-\imath k \frac{(x - x_0)^2 + (y - y_0)^2}{2R(z)}\right], \end{aligned} \tag{4.19}$$

where $R(z) = z - z_0$ is the radius of curvature of the spherical wave in the plane z. Setting x_0 and y_0 to zero for simplicity and converting the axial position of the source point, z_0, into a complex number by subtracting it from an arbitrary quantity we call q_0. This is equivalent to replacing the radius of curvature $R(z) = R_0 + z - z_0$ by the complex quantity, the complex beam parameter, $q(z) = z - (z_0 - q_0)$. Equation (4.19) can now be written as

$$u(x, y, z) = \frac{1}{q(z)} \exp\left[-\imath k \frac{x^2 + y^2}{2q(z)}\right]. \tag{4.20}$$

The exponent in this equation can be separated into real and imaginary parts by first separating the complex beam parameter into real and imaginary parts as

$$\frac{1}{q(z)} \equiv \frac{1}{q_{\mathrm{re}}(z)} - \imath \frac{1}{q_{\mathrm{im}}(z)}. \tag{4.21}$$

The spherical wave equation now becomes

$$u(x,y,z) = \frac{1}{q(z)} \exp\left[-\imath k \frac{x^2+y^2}{2q_{\mathrm{re}}(z)} - k\frac{x^2+y^2}{2q_{\mathrm{im}}(z)}\right]. \tag{4.22}$$

which can be transformed into its more common form

$$u(x,y,z) = \frac{1}{q(z)} \exp\left[-\imath k \frac{x^2+y^2}{2R(z)} - \frac{x^2+y^2}{2w^2(z)}\right], \tag{4.23}$$

by setting the real part $q_{\mathrm{re}}(z) = R(z)$ and the imaginary part $q_{\mathrm{im}} = k/2w^2(z) = \pi w^2(z)/\lambda$. The propagation of the complex beam parameter can be calculated as [67]

$$\frac{1}{q(z)} \equiv \frac{1}{R(z)} - \frac{\imath\lambda}{\pi w^2(z)}, \tag{4.24}$$

where $w(z)$ is the beam radius in the x-y-plane at position z, where the beam irradiance has dropped to its $1/e^2$ value and $R(z)$ is the beam's radius of curvature at position z. It can be shown that

$$w(z) = w_0\sqrt{1+\left(\frac{\lambda z}{\pi w_0^2}\right)^2} \tag{4.25}$$

$$R(z) = z\left[1+\left(\frac{\pi w_0^2}{\lambda z}\right)^2\right]. \tag{4.26}$$

The length over which the beam radius $w(z)$ increases by a factor of $\sqrt{2}$ is called the Rayleigh length, z_R, which is given by

$$z_R = \frac{\pi w_0^2}{\lambda}. \tag{4.27}$$

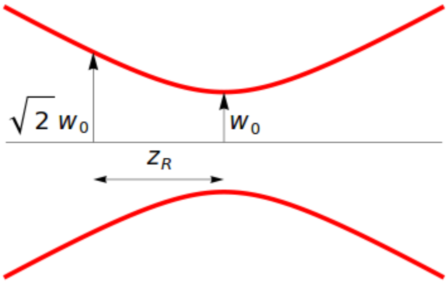

FIGURE 4.1: Beam shape of a Gaussian laser beam around its focus. The beam radius (waist) given by w_0 and the Rayleigh length z_R at which the beam has widened to $\sqrt{2}w_0$ are indicated.

To describe the propagation of the beam the well known ABCD formalism, which is widely used in ray optics, can be used where the new complex beam parameter q_f can be calculated from a known previous beam parameter q_i via

$$\begin{pmatrix} q_f \\ 1 \end{pmatrix} = \mathcal{N} \begin{pmatrix} A & B \\ C & D \end{pmatrix} \begin{pmatrix} q_i \\ 1 \end{pmatrix} \tag{4.28}$$

where $\mathcal{N}$ is a normalization constant chosen to keep the second component of the vector describing the Gaussian beam as 1. Expanding Eqn. (4.28) according to the standard rules of matrix multiplication gives the system of equations

$$q_f = \mathcal{N}(Aq_i + B) \tag{4.29}$$

$$1 = \mathcal{N}(Cq_i + D) \tag{4.30}$$

and subsequent division of Eqns. (4.29) and (4.30) eliminates the normalization constant and gives the commonly used form [67]

$$q_f = \frac{Aq_i + B}{Cq_i + D}. \tag{4.31}$$

The ABCD matrix for free propagation along a distance z can be written as

$$\begin{pmatrix} A & B \\ C & D \end{pmatrix} = \begin{pmatrix} 1 & z \\ 0 & 1 \end{pmatrix} \tag{4.32}$$

leading to a evolution of the complex beam parameter described by

$$q_f = q_i + z. \tag{4.33}$$

Similarly, the matrix for a thin lens of focal length f can be written as

$$\begin{pmatrix} A & B \\ C & D \end{pmatrix} = \begin{pmatrix} 1 & 0 \\ -\frac{1}{f} & 1 \end{pmatrix} \tag{4.34}$$

leading to a beam parameter evolution of

$$\frac{1}{q_f} = \frac{1}{q_i} - \frac{1}{f}. \tag{4.35}$$

To propagate the complex beam parameter through a more complicated optical system the ABCD matrices have to be multiplied in reverse order according to the rules of normal matrix multiplication. The final ABCD matrix for a system of three lenses with focal lengths f_1, f_2 and f_3, and free propagation along the distances z_{12} and z_{23} between those lenses, like the one used to focus the beam into our setup for example, would therefore look like this:

$$M_{ABCD} = \begin{pmatrix} 1 & 0 \\ -\frac{1}{f_3} & 1 \end{pmatrix} \begin{pmatrix} 1 & z_{23} \\ 0 & 1 \end{pmatrix} \begin{pmatrix} 1 & 0 \\ -\frac{1}{f_2} & 1 \end{pmatrix} \begin{pmatrix} 1 & z_{12} \\ 0 & 1 \end{pmatrix} \begin{pmatrix} 1 & 0 \\ -\frac{1}{f_1} & 1 \end{pmatrix}. \tag{4.36}$$

With these tools it is possible to design a lens system that delivers the desired beam parameters, such as final beam waist, incorporating the restrictions placed upon such a system such as minimum distance between final lens and focal position.

4.3 Trap Design

In the following sections the design of the light sheet and the scanning beam trap will be presented. In addition, a novel way for producing ring traps will be discussed. However, before describing the optical dipole traps used in our setup an overview over single beam optical dipole traps will be given which are the basis for any optical dipole trap design.

Single Beam Optical Dipole Traps

Optical dipole traps use laser beams that are red-detuned with respect to the atomic transition of the atoms. As a result the atoms are drawn towards the maximum of the irradiance distribution of the laser beam, that is the focus. The irradiance profile of a Gaussian laser beam of power P propagating along the z-direction follows the irradiance distribution

$$I(r,z) = \frac{2P}{\pi w^2(z)} \exp\left(-2\frac{r^2}{w^2(z)}\right), \tag{4.37}$$

where r describes the radial coordinate and $w(z)$ is the spot size defined in section 4.2. Since $U_{\mathrm{dip}}(r,z) \propto I(r,z)$, the optical potential follows directly from the irradiance distribution of the laser beam, as is evident from Eqn. (4.9).

The potential at point (0,0) is referred to as the trap depth U_0 and is often given in units of temperature

$$T = \frac{U_0}{k_B}. \tag{4.38}$$

For the case that the thermal energy of the trapped atoms is much smaller than the trap depth, it is possible to approximate the optical potential as a harmonic oscillator. The radial and axial trapping frequencies, ω_r and ω_z, defined in accordance with Fig. 4.2 as the trapping frequencies in the x and y direction or the z direction respectively, are important parameters to characterize the trap and the ratio of trapping frequencies gives the aspect ratio of the trap. The dipole potential can be written as [64]

$$U_{\mathrm{ODT}} \simeq -U_0\left[1 - 2\left(\frac{r}{w_0}\right)^2 - \left(\frac{z}{z_R}\right)^2\right], \tag{4.39}$$

while the radial and axial trapping frequencies can be written as

$$\omega_r = \sqrt{-\frac{4U_0}{m\omega_0^2}} \qquad \text{and} \qquad \omega_z = \sqrt{-\frac{2U_0}{mz_R^2}}, \tag{4.40}$$

where m in the previous equations is the mass of the atoms. The aspect ratio is calculated as

$$\frac{\omega_r}{\omega_z} = \sqrt{2}\frac{z_R}{w_0} = \sqrt{2}\frac{\pi w_0}{\lambda}, \tag{4.41}$$

where λ is the wavelength of the laser beam. From Eqn. (4.41) it is evident that it is the ratio of beam waist to laser wavelength that determines the aspect ratio which will always be greater than one. Consequently, a single beam trap will always be cigar shaped. To reduce asymmetry of the condensate and stop the spread of atoms along the beam axis of the trapping beam a light sheet as described in the following section can be used together with a single beam optical dipole trap, as is done in our scanning beam trap design described in section 4.3.2.

4.3.1 Light Sheet

A light sheet is used for the condensation dynamics experiments where it creates the Gaussian dimple potential that is added to the harmonic potential formed by the magnetic trap. This type of potential is used as it allows for the modification of phase-space densities and thereby allows to start the condensation process where a thermal cloud turns into a coherent matter wave without further cooling of the atomic sample. The process by which a thermal cloud that is inherently incoherent develops coherence properties is not yet fully understood and of significant interest. More details on the use and significance of optical dimple potentials will be given in chapter 5. the light sheet is also used in the scanning beam experiments where the light sheet provides trapping in the axial direction of the scanned beam where the trapping provided by the scanned beam itself is weak. We speak of a light "sheet" because the beam is focused in one dimension only while the other dimension is expanded (see Fig. 4.2). Currently the beam has waists in horizontal and vertical directions of $w_{\mathrm{x}} = 11\mu\mathrm{m}$ by $w_{\mathrm{z}} = 220\mu\mathrm{m}$ in the plane of the atoms. Given that the vertical size of the atom cloud is less than $10\mu\mathrm{m}$ the intensity of the light sheet in the long direction can be well approximated to be constant so there is no contribution to the trapping potential.

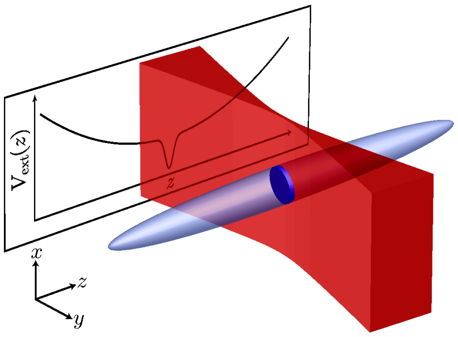

FIGURE 4.2: Schematic of a light sheet intersecting a cigar shaped atom cloud with the potential created by overlapping the light sheet with a magnetic trap indicated. Reproduced from [46].

As a light source a 840nm ECDL diode laser head in a Toptica DL100 laser is used. This laser has no further frequency stabilization since any shifts in frequency are negligible given the total detuning of more than 50nm. The power, however, is actively controlled by a single-pass AOM working in conjunction with a proportional-integral (PI) controller. A user's guide and circuit diagrams for the PI controller can be found in [39].

The emitted laser beam is cleaned up by a single mode polarization maintaining fibre after which the control AOM is positioned. After that the light goes through a cylindrical lens that provides the necessary astigmatism. An adjustable mirror to control the final position of the laser beam relative to the atoms is placed before a last lens that focuses the beam in the plane of the atoms. Figure 4.3 shows a schematic of the light sheet optics and electronics.

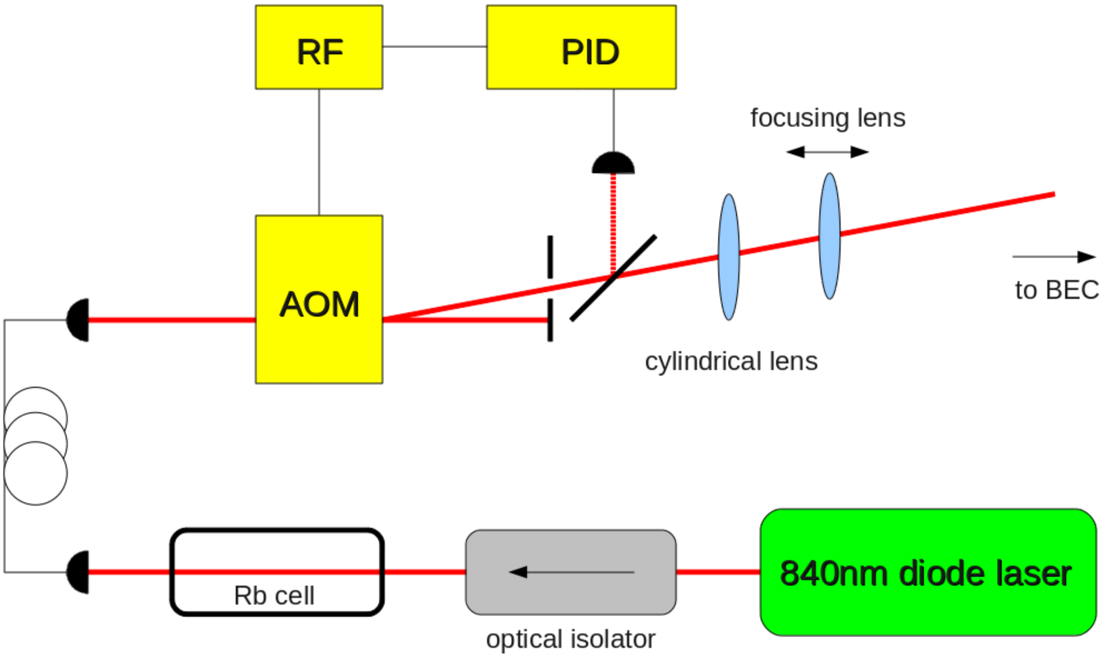

Figure 4.3: Schematic of the light sheet optics and electronics. 840nm light from a Toptica DL100 laser goes through an optical isolator to prevent back scattering into the laser diode before going through a glass cell with rubidium vapour which acts as filter for all resonant light. After that the beam profile is cleaned up by a polarization maintaining fibre before going through an AOM to actively control the light intensity. A cylindrical lens widens the beam in one direction before it is focused down at the position of the atom cloud.

With the setup described above, a maximum usable power of 4.4mW can be reached before the glass cell, which corresponds to a maximum trap depth in this configuration of more than 1.5mK, deep enough to trap BEC with a transition temperature in our setup of below 250nK.

4.3.2 Scanning Beam Trap

This section will describe the scanning beam trap developed at the University of Queensland which allows for the creation of versatile two dimensional potential landscapes. This trap consists of a far red-detuned laser beam which is tightly focused at the position of the atoms. This laser beam is then spatially scanned using a two-dimensional AOM. When scanned fast enough, that is with a scanning frequency much faster than the frequency of the trap (in the experiments presented here this means scanning faster than 30KHz), the atoms experience a time averaged potential the shape of which depends on the beam path chosen for the scanning. By changing the beam path in successive scans the trap can be used to create dynamic potentials.

In order to properly describe the scanning trap the light source and the electronics for the trap will be discussed before the section will be concluded by giving the optical design of the scanning trap. The majority of this section has been published in [40].

Laser And Electronics

The light source used for the scanning beam trap is a single mode IPG fibre laser (YLR-5-1064-LP) with a maximum output power of 5W at a wavelength of 1064nm. Due to losses at the AOMs this gives a usable power of about 1W before the glass cell which contains the BEC. After leaving the fibre laser the light travels through a control AOM connected to a PID controller for noise cancellation as well as computer control of the laser power. To be able to scan the beam spatially the light is then sent through a two-dimensional AOM (IntraAction, DTD-274HD6), which has two crystals mounted perpendicularly with respect to their diffraction directions. Since diffraction in the crystals follows the Bragg condition

$$d \sin\theta_B = m\lambda, \tag{4.42}$$

where d is the lattice spacing and m the diffraction order, it is possible to change the diffraction angle θ_B in the horizontal as well as vertical direction allowing an arbitrary scan of the beam in two-dimensions. The lattice spacing is controlled by choosing the RF frequency that drives the AOM. The relationship between the diffraction angle and the RF frequency F can be written as [68]

$$\theta_B = \frac{\lambda F}{2v}, \tag{4.43}$$

with $\lambda = \lambda_0/n$ the light wavelength inside the crystal, v the acoustic velocity of the RF wave, and F the RF frequency.

It is convenient that the 2D-AOM we are using works at a relatively low RF frequency of 27MHz. Because of this it is easy to use off the shelf RF generation electronics which can be bought at reasonable prices. In our case the RF frequencies are generated by two independent computer controlled PCI cards (Spincore, PulseBlasterDDS-I-300) which have 1024 programmable frequency and 1024 programmable amplitude registers. In each of these registers an independent value for the frequency (amplitude) of the RF can be stored with a resolution of 1mHz (0.0001 times the maximum amplitude), therefore allowing for a maximum resolution in the frequency spacing of $\Delta f/1024$, where Δf is the scanning range of RF used in a specific experiment. In our case the scanning range was usually below 2MHz resulting in a RF frequency resolution of 2KHz. The fact that frequency and amplitude registers are independent means that the same frequency can be adjusted in amplitude should that need arise. This was used for the proposed critical velocity experiments described below. Addressing these registers desired sequences determining the beam path can be written with a maximum length of 32k words. The cards have a scanning range from DC to 50MHz, which is far above the 27MHz centre frequency of the 2D-AOM, in mHz steps. The speed of frequency changes is given by the maximum time resolution of 13.3ns.

Beam Shaping

The laser used for trapping, an IPG fibre laser running at a wavelength of 1064nm, provides a collimated beam output of $w_0 = 2.5$mm ($1/e^2$ level) which has to be re-sized to clear AOM apertures, not exceed maximum power densities within AOM crystals, and to provide the desired focal size at the position of the BEC. For this the beam is first scaled down by a factor of 5 using a $f_1 = 150$mm : $f_2 = 30$mm telescope to clear the aperture of the control AOM. After that the beam is expanded by a factor of 2.5 using a $f_3 = 16$mm : $f_4 = 40$mm telescope to reduce the power density in the 2D-AOM. This beam of $w = 1.25$mm is then going through a lens system consisting of three lenses of focal lengths $f_5 = 40$mm, $f_6 = 200$mm and $f_7 = 150$mm which create the final spot size at the location of the BEC. An image of the beam focus is shown together with cross sections in x and y directions in Fig. 4.5. Restrictions that had to be taken into consideration are the maximum beam size before the chamber which has to be able to clear a 2" MOT mirror mounted under a 45 deg angle, and the distance between the final focusing lens (external to the vacuum) and the BEC, which has to be larger than $\sim$ 130mm. A schematic of the whole setup with the optics and electronics can be found in Fig. 4.4.

Using the Gaussian beam formalism from section 4.2 and the equations describing the dipole force from section 4.1 we obtain the parameters listed in Table 4.1 for our single beam trap.

Time Averaged Potentials

While it is possible to slowly move the laser beam in order to have the atoms adiabatically follow the position of the laser beam, in the design used in our experiments the beam is scanned at a frequency much higher than one the atoms can respond to, in our case more than 30KHz, creating a time averaged potential in two dimensions. This procedure is similar to the original Time Orbiting Potential (TOP) magnetic traps developed by Petrich *et al.* in their original quest for BEC [69]. Time-averaged optical traps have been realized before, in particular in references [70–72] which all used blue-detuned beams for trapping thermal atoms.

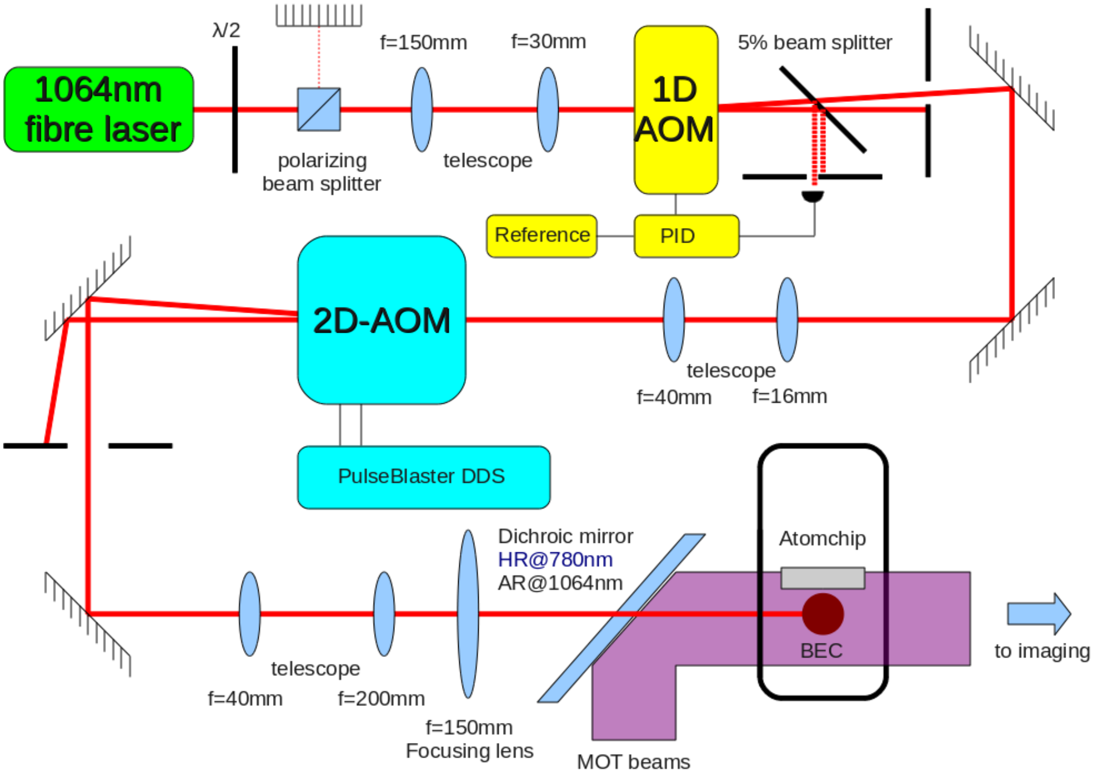

FIGURE 4.4: Schematic of the optics and electronics to control the scanning beam trap. The light of an 1064nm IPG fibre laser is intensity controlled by a PID circuit (indicated in yellow) and then put through a 2D-AOM for scanning in two directions controlled by two PulseBlasterDDS PCI cards (indicated in cyan). Also shown are various lenses for beam shaping including the final lens providing a spot size of 18.5μm in the plane of the atom cloud.

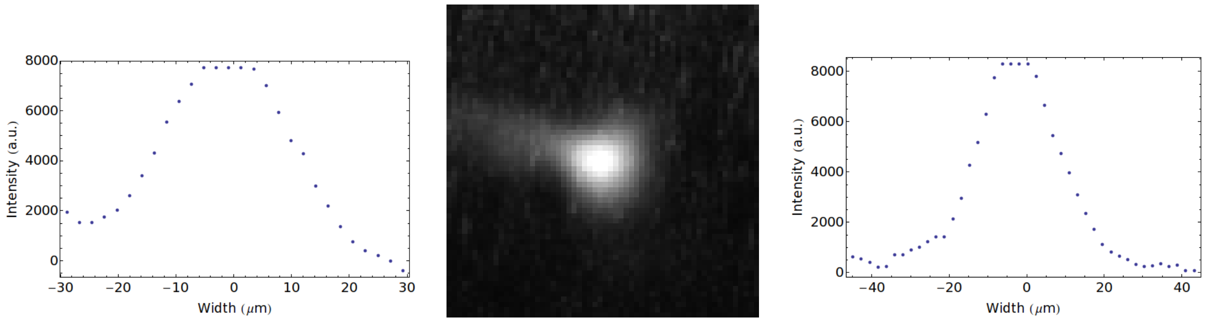

FIGURE 4.5: Image of the focus of the scanning beam trap (centre) with cross sections in x (left) and y (right) direction.

In cases where complex potentials are created the atoms in the trap would usually experience a trapping potential less than 50% of the time. To test the effect of time-averaging on a BEC, and to investigate what constitutes scanning frequencies "much higher" than the

Table 4.1: Parameters of our single beam optical dipole trap.

Parameter	Value
wavelength	1064nm
beam waist w_0	18.5μm
Rayleigh length z_R	1.01mm
max trap depth U_0	243μK
max radial trapping frequency ω_r	2.63KHz
max axial trapping frequency ω_z	34Hz
aspect ratio	77

trapping frequencies involved, at which heating is expected, the following experiment was conducted.

A thermal cloud close to the critical temperature T_c was created in a cigar-shaped magnetic trap [40]. Trapping frequencies of this trap were 160Hz ×6.8Hz. A dimple potential with a beam waist of 11μm was then overlapped with the cigar shaped trap, crossing the middle of the long axis of the BEC. For a dipole trap of depth 250μK this resulted in the formation of a BEC with a condensate fraction of 15.3%. Subsequently, the same experiment was conducted with a laser beam that was modulated with an on/off duty cycle of 20%, increasing the potential depth by a factor of five to ensure the trap had the same time-averaged depth. The frequency of the modulation was then varied and the condensate fraction measured to study the effect on the atom cloud. Results of these measurements are shown in Fig. 4.6. It was found that above a frequency of 30KHz the condensate fraction approached the same value as for the initial DC optical trap. This value is about 7 times the trapping frequency of the dimple trap of about 4KHz. Scanning frequencies of this order are therefore found to be sufficiently high to be considered time-averaged when ultra-cold atoms are considered.

4.3.3 A Novel Way To Create Ringtraps

Static Toroidal Traps

One of the applications proposed for the scanning beam trap described in the previous section is the creation of ring traps to be used with ultra-cold atoms. There have been a number of proposals and demonstrations to create ring traps over the last ten years. These traps are interesting because they can be used to create Sagnac type atom interferometers as well as possessing a multiply connected geometry that is important, when one is trying to create persistent currents for example. Previous proposals include magnetic traps [73–75], rf-dressing [76] and optical methods using spatial light modulators [77]. One feature that most of these proposals have in common is that they tend to be large, resulting in increased sensitivity for e.g. Sagnac interferometry, but are problematic when smaller rings are desired as for example for the study of superfluidity. In particular lack of homogeneity of the potential

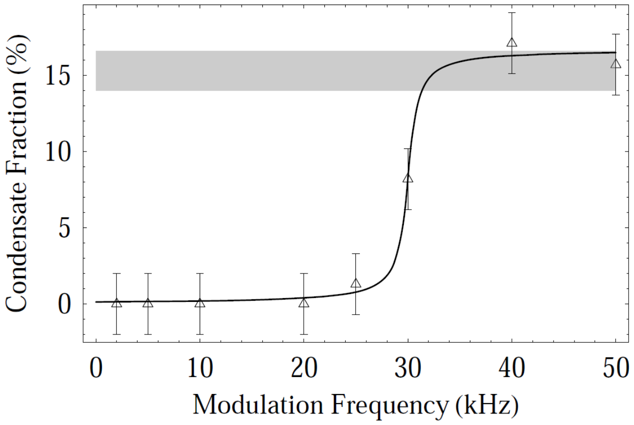

FIGURE 4.6: Condensate fraction of a BEC in a magnetic trap with an optical dipole trap superimposed run with a 20% on/off duty cycle. Initial condensate fraction without dipole trap was 15.3% and is indicated in grey. The line through the data points acts only as a guide to the eye.

over the whole area of the ring and the problem of forming a multiply-connected condensate delocalized over the whole ring structure can cause problems in these large rings.

Recently, Ryu *et al.* [78] reported the first observation of a persistent current in a multiply connected BEC in a magnetic potential which has been plugged with a blue detuned optical dipole potential. However, the lifetime of the superflow was limited to 10s due to a drift of the magnetic trap relative to the optical potential. Furthermore, the trap depth of the ring varied around the torus. Even though this variation was less than the chemical potential of the BEC, for a careful study of superfluidity it is desirable to have a more constant potential depth about the entirety of the ring.

To achieve such stable ring traps we developed the following strategy. If a far red-detuned laser beam is rapidly scanned in space, applying orthogonal sine wave modulations 90 deg out of phase in respect to each other to the AOM frequencies, the deflected beam follows a circular path. If that scanning is done fast enough the atoms will experience a time-averaged potential in the shape of a toroid. Unfortunately, changing the angle of deflection, which is done by changing the rf frequency, changes the diffraction efficiency of the AOM resulting in an uneven light intensity distribution over the ring and therefore a variation in potential depth around the torus. Since that variation in intensity with deflection angle is deterministic, a feed forward technique can be employed to compensate for it. If this intensity distribution is measured on a photo diode fast enough to resolve individual scans of the ring an intensity profile of the ring can be created. Mixing this profile with the rf signal driving one of the AOMs allows the intensity profile to be evened out since the deflection efficiency does depend on the acoustic power P of the rf driving the AOM like [68]

$$I = I_0 \sin^2 \sqrt{\eta} \qquad \text{with} \qquad \eta = \frac{\pi^2}{2\lambda_0^2} M \frac{L}{H} P, \tag{4.44}$$

where I_0 is the incident light irradiance, M is the acousto-optic figure of merit for the crystal,

L and H are the length and height of the acoustic beam and λ_0 is the wavelength of the incident beam. For small η the small angle approximation can be employed so that the light intensity after the AOM can be considered proportional to the rf power P. Figure 4.7 shows a schematic of the feed forward technique to control the light distribution.

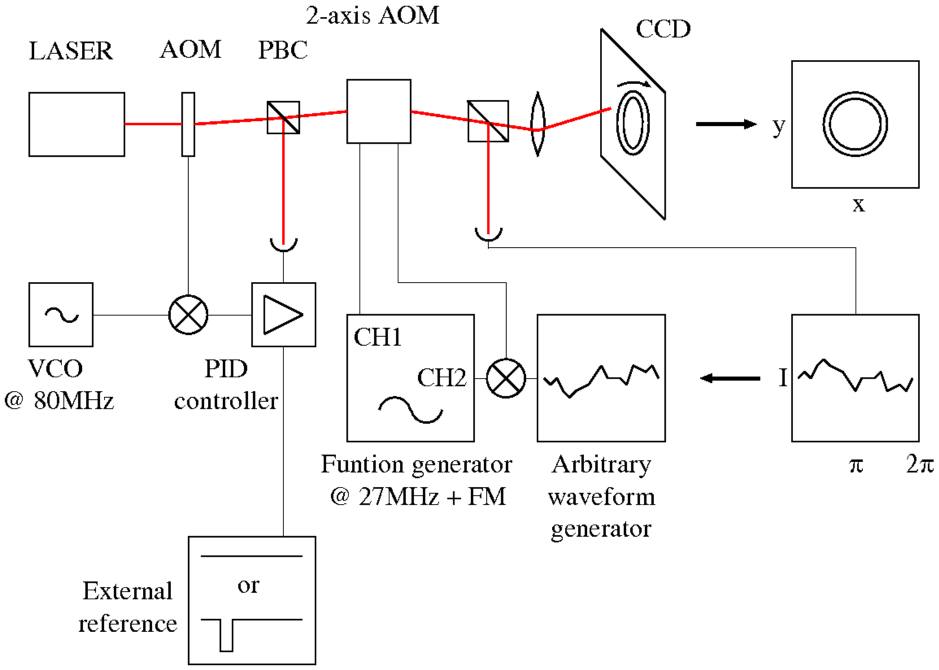

Figure 4.7: Feed-forward technique to cancel the effect of different diffraction efficiencies depending on the angle of deflection. When the intensity locked laser beam is scanned it is imaged on a CCD camera and some part of it is deflected onto a photo diode. The photo diode gives an intensity profile that is then inverted and mixed with the rf signal that drives the AOM. Extra modulation of the intensity over the ring can be accomplished with an additional signal to the intensity lock.

Using this technique we demonstrated how a toroidal trap might be realized. For these the laser beam was focused to a spot size of 25μm and then scanned to create a ring radius of 44μm. The scanning speed used was 51KHz, well above any trapping frequencies in our experiment. When the ring profile was measured on a fast photo diode intensity fluctuations about the ring were less then 1.5%. After that level of correction no correlation between the noise and the initial intensity fluctuations or the frequency modulation of the rf were observed. From this we conclude that the remaining noise level is due to electronic noise rather then the scanning process. It should be noted that using a feedback system would be preferable but electronically far more complicated as this would require a relatively high frequency feedback system.

It was noted before that the aim is to suppress fluctuations of the optical potential well below the level of the chemical potential of the BEC. In the Thomas-Fermi approximation for a condensate in a ring trap with a trapping frequency of ω_z in the z-direction the chemical potential can be calculated as [40]

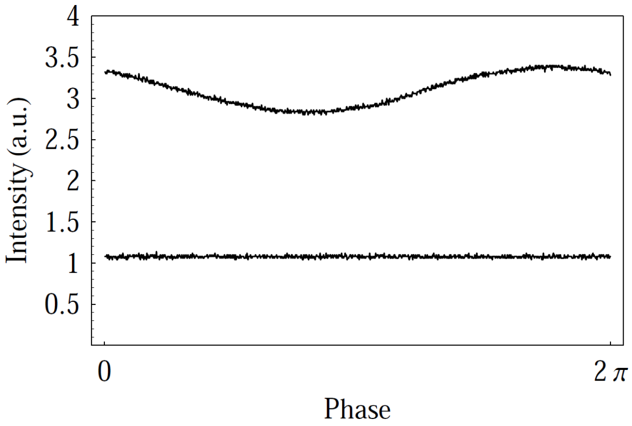

FIGURE 4.8: Intensity profiles of the rings without (top curve) and with (bottom curve) feed-forward. Corresponding CCD images are shown in Fig. 4.10, where the first image shows the uncorrected and the second image the corrected ring.

$$\mu = \hbar\sqrt{\omega_r\omega_z}\sqrt{\frac{3Na_s}{4a}}, \tag{4.45}$$

where a is the ring radius.

For the case of a trap with beam waist $w_0 = 25\mu\text{m}$, ring radius $a = 44\mu\text{m}$, optical power $P = 5\text{W}$ and at a wavelength of 1064nm, we get a resulting trap depth of 479nK, and therefore a corresponding variation in trap depth of 7.2nK. The trapping frequency in the radial direction of such a trap is $\omega_r = 2\pi \cdot 83\text{Hz}$ and assuming a trapping frequency in z-direction of $\omega_z = 2\pi \cdot 350\text{Hz}$ with $2 \cdot 10^5$ atoms in the BEC one gets a chemical potential of $\mu = 36\text{nK}$. By comparing the variation in trap depth of 7.2nK to the chemical potential of 36nK it can be seen that the intensity fluctuations around the toroid are much smaller than the chemical potential of the BEC making such a trap a feasible tool for the investigation of ultra-cold gases, since the chemical potential gives the energy scale below which the BEC remains basically undisturbed.

In general, for a static beam with spatial irradiance $I(\mathbf{r})$ and detuning Δ the optical dipole potential is given by Eqn. (4.9). Using a two dimensional irradiance profile $I(x, y) = \frac{2P}{\pi w^2}\exp\left(\frac{-2(x^2+y^2)}{w^2}\right)$ scanned in a ring with radius a, the resulting radial dependent average intensity can be written as

$$I(r) = \frac{4P}{w^2}\exp\left(\frac{-2(r^2+a^2)}{w^2}\right)\mathcal{I}_0(\zeta), \tag{4.46}$$

where $\mathcal{I}_0(\zeta)$ denotes the modified zeroth-order Bessel function with $\zeta = 4ar/w^2$ and w the beam waist of the focused beam trap. Since the trap minimum occurs at $r = a$, we can approximate $I(r)$ by a series expansion around a up to the quadratic term as

$$I(r) \approx I(a) + \frac{I''(a)}{2}(x-a)^2. \tag{4.47}$$

Using the fact that $\frac{\partial}{\partial z}\mathcal{I}_0(z) = \mathcal{I}_1(z)$ and the harmonic approximation $U = \frac{m}{2}\omega_r^2(x-a)^2$ we can now solve for ω_r and obtain the radial trapping frequency as [40]

$$\omega_r = \sqrt{\frac{2\kappa}{m} P \exp\left(-\frac{4a^2}{w^2}\right)\left[\frac{64a^2}{w^6}(\mathcal{I}_0(\zeta) - \mathcal{I}_1(\zeta)) - \frac{8}{w^4}(\mathcal{I}_0(\zeta) + \mathcal{I}_1(\zeta))\right]}, \tag{4.48}$$

with $\mathcal{I}_n$ the modified n-th order Bessel functions and $\kappa = -\frac{3\pi c^2}{2\omega_A}\frac{\Gamma}{\Delta}$, where ω_A is the optical transition frequency of the atom. We find that $\omega_r \propto 1/\sqrt{a}$ for a much larger than the beam waist. A graph of Eqn. (4.48) is shown in Fig. 4.9.

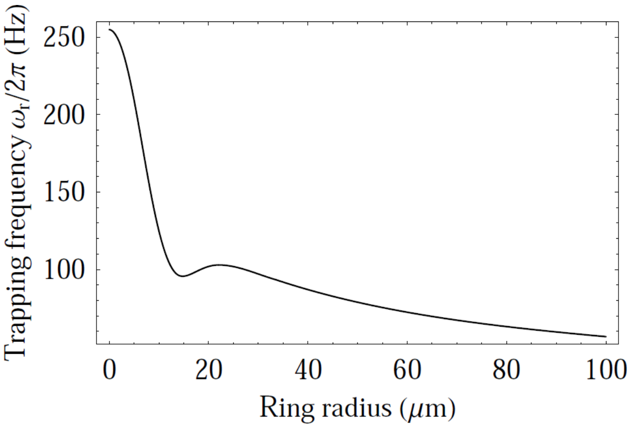

FIGURE 4.9: Trapping frequency as a function of ring size for a beam waist of 25μm.

Arbitrary And Dynamic 2D Potentials

As well as adding a correction signal, it is possible to add an extra modulation signal that is also synchronized with the rf-modulation frequency f_S. For a constant signal this results in a static and arbitrary irradiance modulation on top of the 2D potential. This can be done by using the reference input of the irradiance lock of the setup. To show the feasibility of this method to produce various other 2D trapping geometries, a horse shoe shape and a ring lattice with five lattice sites have been created and stabilized as shown in Fig. 4.10. The slight variation in irradiance that can be observed in this figure even after the correction signal is added is due to the fact that the imaging program used auto scaling, thereby making variations visible that would not have been visible in the image without the correction signal applied. Further reduction in irradiance variation is possible by applying several iterations of the correction step to the signal.

Furthermore, it is possible to create 2D potentials that vary with time, for example by introducing a small difference between the frequency of the rf modulation and the frequency of the extra intensity modulation frequency f_e in such a way that the pattern rotates with the difference of the two frequencies, $|f_d = f_s - f_e|$. In this manner, for example, a ring lattice can be slowly rotated with excellent control over all trapping parameters. This could

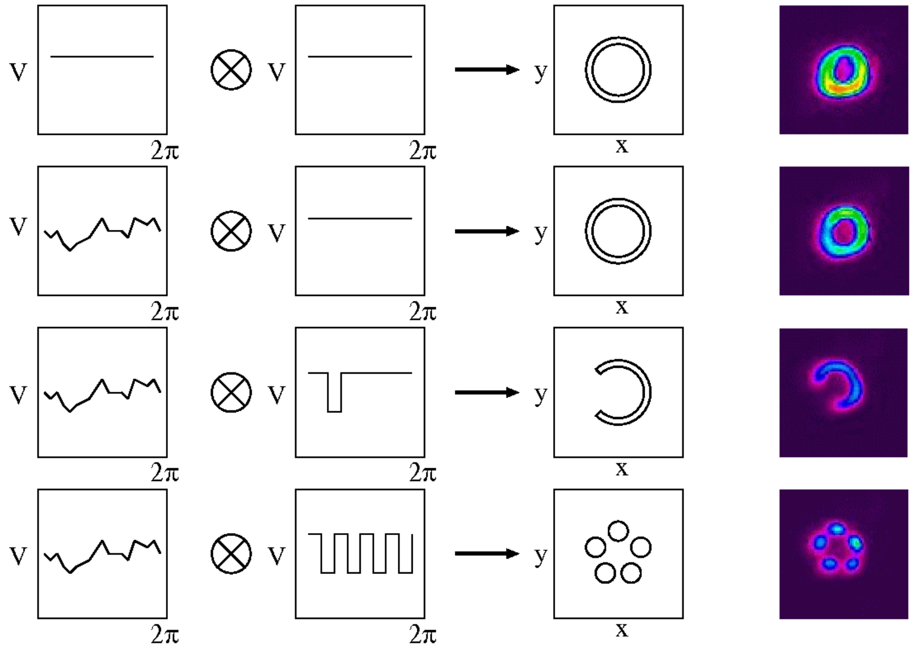

FIGURE 4.10: Different possible waveforms for the function generator controlling the feed-forward technique (left row) and the function generator controlling the PID circuit (second row from left) with resulting patterns schematically (second row from right) and imaged on a CCD camera (right row). The top pattern shows a uniform distribution for both function generators resulting in a ring with non-uniform light distribution. For all the other cases the first generator is used to cancel the effects of different diffraction efficiencies and the second generator to create patterns of laser power leading to a uniform ring, horse shoe and ring lattice, respectively. The size of the images is $330 \times 330\mu$m.

be used to initiate persistent currents as suggested in [77]. Another method of introducing angular momentum to the system would consist in a dip in laser power, which effectively acts like a little barrier, that is slowly moved around the ring to stir the BEC, similar to the technique used to stir a BEC with a blue-detuned laser beam (e.g. [79]).

In a similar fashion we can arbitrarily adjust the shape and the depth of the potential as a function of time, where the spacial resolution is limited by the waist of the laser focus. The temporal resolution is merely limited by the ratio between size of the laser beam in the AOM crystal and the speed of sound in the crystal or by the electronics used, which for both is better than 100μs.

5

Condensation Dynamics In A Dimple Trap

The dynamics of condensation of Bose-Einstein condensates is an open problem in the field of ultra-cold atoms. The process by which a thermal cloud that is inherently incoherent develops coherence properties is not yet fully understood and of significant interest. First quantitative predictions were made in 1997 by Gardiner *et al.* [41], when a rate equation for the growth of a condensate from a super-critical thermal vapour was derived. Experiments were performed by Miesner *et al.* [42] that found good qualitative but no quantitative agreement with the theory. Even after Gardiner and co-workers used improved formalisms [43–45] their numerical calculations did not give quantitative agreement with the experiment. This discrepancy has remained unresolved. Since then experiments have shifted their focus from the condensate growth dynamics to how phase coherence and long range order develop in a growing condensate, often by looking at the formation of quasi-condensates. Quasi-condensates are atomic clouds that form condensates of differing phases during condensate formation, often in elongated traps. The formation of these quasi-condensates was studied by Köhl and co-workers in 2002 [80] and compared to calculations by Davis *et al. [81].* Good qualitative agreement was found and for some parameters the theory did fit the data well, while for other parameters initial quasi-condensate growth predicted by theory was faster than observed. Experiments done in 2007 by Hugbart *et al.* [82] using momentum Bragg spectroscopy on an elongated Bose-Einstein condensate which was created by shock cooling, that is rapidly cooling through T_c with an rf-knife, showed quantitative agreement between quantum kinetic theory and their data except for an unexpected time delay. Unlike the experiments presented in this thesis the atomic cloud got cooled through the phase transition, while the experiments presented here create the condensate without further cooling by increasing the phase-space density at a constant temperature which is initially just above T_c. In the same year Ritter *et al.* [83] investigated the formation of long-range order in quasi-condensates by studying the first-order spatial correlation function $G^{(1)}(r,r') = \langle \Psi^\dagger(r)\Psi(r')\rangle$ (where $\Psi^\dagger$ and Ψ denote the creation and annihilation operators of the atomic fields) and found that atomic density increased in a spatially homogenous way, while coherence developed first at the center of the trap and then spread to the edges. No quantitative theoretical study was presented with this work. The creation of the quasi-condensate investigated again worked by shock-cooling through T_c. Finally, the most recent study was published in 2008 by Weiler *et al.* [84] where the spontaneous formation of vortices was studied, when an atomic cloud is evaporatively cooled through T_c. It was found that numerical calculations where able to predict the growth in condensate atoms as well as the number of vortices present which decayed over time. However, all these recent studies cool the atomic clouds through the transition temperature to study the formation of condensate growth, coherence and long-range order, while the results presented in this trap are closer to those experiments performed by Miesner *et al.* in 1998. In the work presented here an atomic cloud is prepared just above T_c and then no further cooling takes place, while a condensate forms simply due to the application of a dimple potential which increases the phase-space density.

To further the understanding of condensate growth dynamics the following chapter will first describe a theory of thermodynamics and formation dynamics of Bose-Einstein condensation in a dimple trap which was developed by fellow PhD student Michael Garrett [46]. In this theory the equilibrium thermodynamics of both a sudden and a quasistatic turn-on of a dimple potential are compared to a semiclassical description of a condensate and thermal gas. Based on measured initial equilibrium conditions, final equilibrium conditions are calculated using semiclassical Hartree-Fock theory. The condensate formation dynamics following the sudden turn-on of a dimple potential are then compared to a quantum kinetic model of condensate growth. In a second section, previous experimental work will be summarized and in a third section our measurements are compared to the theoretical models. The final section of this chapter reports preliminary results on rethermalization dynamics of a Bose-Einstein condensate in a different trapping geometry for which there is currently no theory available.

5.1 Theory

A first series of experiments conducted by Dr. Adrian Ratnapala applied dimple potentials (see Fig. 5.1 also Fig. 4.3) of various depths and measured the resulting equilibrium temperatures and condensate fractions for a wide and a narrow dimple, as well as for both quasistatic and sudden turn-on of the dimple potential. It was shown that for a dimple of appropriate depth condensate formation without further cooling of the atom cloud could be achieved and that an optimal dimple depth exists where the condensate fraction is maximized. To explain these measurements a theoretical model was developed by fellow PhD student Michael Garrett [46] in which final equilibrium thermodynamics of a condensate and thermal gas are calculated in a strictly non-dynamical Hartree-Fock theory to predict the evolution of a Bose gas. The theory incorporates full meanfield interactions of both the condensate and the thermal cloud as well as three-body loss processes. Good agreement between theory and experiment were observed.

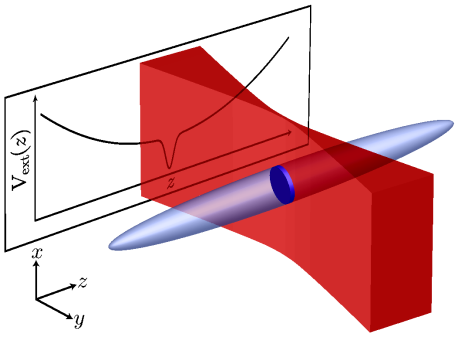

FIGURE 5.1: Schematic diagram of a light sheet intersecting a cigar shaped atom cloud with the potential created by overlapping the light sheet with a magnetic trap indicated. The optical potential creates a small dimple in the much stronger harmonic magnetic trap. Reproduced from [46].

5.1.1 Equilibrium Thermodynamics

At equilibrium, the thermal cloud is well described by the Bose-Einstein distribution

$$f_{BE}(\epsilon_{\rm th}(\mathbf{r},\mathbf{p})) = \left[\exp\left(\frac{\epsilon_{\rm th}(\mathbf{r},\mathbf{p})-\mu}{k_BT}\right)-1\right]^{-1}, \tag{5.1}$$

where $\epsilon_{\rm th}(\mathbf{r},\mathbf{p})$ describes the excitation energy, that is the amount of energy needed to add an atom of momentum $\mathbf{p}$ at position $\mathbf{r}$, which in the semiclassical Hartree-Fock approximation is given by the expression

$$\epsilon_{\rm th}(\mathbf{r},\mathbf{p}) = \frac{p^2}{2m} + V_{\rm ext}(\mathbf{r}) + g[2n_0(\mathrm{r}) + 2n_{\rm th}(\mathrm{r})], \tag{5.2}$$

with m the atomic mass, and g the meanfield interaction strength, proportional to the s-wave scattering length a_s as used previously. The factors of 2 in Eqn. (5.2) stem from the 'direct' and 'exchange' interaction terms present in a thermal cloud, where particles in states $|i\rangle$ and $|j\rangle$ have two interaction pathways, either $|i\rangle \rightarrow |i\rangle$ and $|j\rangle \rightarrow |j\rangle$ or $|i\rangle \rightarrow |j\rangle$ and $|j\rangle \rightarrow |i\rangle$ as indicated in Fig. 5.2. The factor of two only appears in the case of interactions between thermal atoms since for condensate atoms $|i\rangle = |j\rangle$ as all atoms are in the same state.

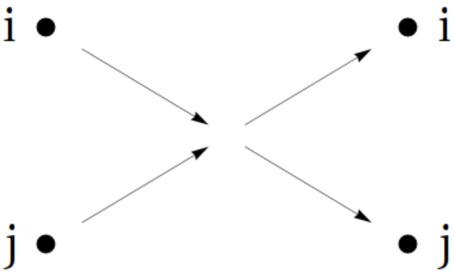

FIGURE 5.2: 'Direct' and 'exchange' interactions between thermal atoms in states $|i\rangle$ and $|j\rangle$, where 'direct' interactions are those interactions with $|i\rangle \rightarrow |i\rangle$ and $|j\rangle \rightarrow |j\rangle$, and 'exchange' interactions are those with $|i\rangle \rightarrow |j\rangle$ and $|j\rangle \rightarrow |i\rangle$.

The external potential $V_{\text{ext}}(\mathbf{r})$ together with the meanfields generated by the thermal cloud and condensate constitute the effective potential affecting the atoms in the thermal cloud. The density of the thermal cloud can be calculated by integrating Eqn. (5.1) in momentum space as

$$n_{\text{th}}(\mathbf{r}) = \int \frac{d\mathbf{p}}{(2\pi\hbar)^3} f_{BE}(\epsilon_{\text{th}}(\mathbf{r},\mathbf{p})), \tag{5.3}$$

while the density of the condensate is calculated using the Thomas-Fermi approximation,

$$n_0(\mathbf{r}) = \begin{cases} \left(\mu - [V_{\text{ext}}(\mathbf{r}) + 2gn_{\text{th}}(\mathrm{r})]\right)/g & \text{if} \quad \mu - V_{\text{ext}} > 0, \\ 0 & \text{otherwise.} \end{cases} \tag{5.4}$$

For given μ and T this can be solved self-consistently since the density of both thermal cloud and condensate fraction depend on the meanfields created by themselves and each other. To make comparison to experiments easier the total atom number N rather then the chemical potential will be specified, since the chemical potential is not an experimentally measured quantity. With this substitution, for given N and T a value of μ can be calculated that is consistent with the densities of both the condensate and the thermal cloud as well as the normalization condition that the total number of atoms be conserved

$$N = \int d\mathbf{r}[n_0(\mathrm{r}) + n_{\text{th}}(\mathrm{r})]. \tag{5.5}$$

Using the densities and chemical potential interesting thermodynamic quantities, such as total entropy and total energy, can be calculated as well as the condensate fraction N_0/N.

The total energy consists of a kinetic component K, a component for the external potential V and an interaction term I such that the total energy $E = K + V + I$, where the individual components can be calculated as

$$K = \int \frac{d\mathbf{r}d\mathbf{p}}{(w\pi\hbar)^3} \frac{p^2}{2m} f_{BE}(\epsilon_{\text{th}}(\mathbf{r},\mathbf{p})), \tag{5.6}$$

$$V = \int d\mathbf{r} V_{\text{ext}}(\mathbf{r})[n_0(\mathbf{r}) + n_{\text{th}}(\mathbf{r})], \tag{5.7}$$

$$I = \frac{g}{2} \int d\mathbf{r}[n_0^2(\mathbf{r}) + 4n_0(\mathbf{r})n_{\text{th}}(\mathbf{r}) + 2n_{\text{th}}^2(\mathbf{r})], \tag{5.8}$$

where the different factors of 1, 2 and 4 in Eqn. (5.8) are again due to the different possible interaction pathways between thermal atoms and condensate atoms, depending on whether the interaction is between a thermal atom and a thermal atom (factor 2), a thermal and a condensate atom (factor 4) or between two condensate atoms (factor 1) [85]. The total entropy S is given by

$$\begin{aligned} S = k_B \int \frac{d\mathbf{r}d\mathbf{p}}{(2\pi\hbar)^3} \frac{p^2}{2m} & \left[f_{BE}(\epsilon_{\text{th}}(\mathbf{r},\mathbf{p})) + 1\right] \cdot \ln\left[f_{BE}(\epsilon_{\text{th}}(\mathbf{r},\mathbf{p})) + 1\right] \\ & - f_{BE}(\epsilon_{\text{th}}(\mathbf{r},\mathbf{p})) \ln\left[f_{BE}(\epsilon_{\text{th}}(\mathbf{r},\mathbf{p}))\right]. \end{aligned} \tag{5.9}$$

Using the initial temperature and atom number from the experiment, initial entropy S_i and energy E_i are calculated before dimple turn-on. Then the final equilibrium temperature and condensate fraction after dimple turn-on are calculated using the same theory. In the case of the quasistatic turn-on the the assumption is made that the system evolves isentropically, such that the equation can be solved for a final temperature where $S = S_i$. For the case of a sudden turn-on on the other hand, the initial densities are used to calculate the energy added to the system when suddenly turning on the dimple,

$$\Delta E = -\int d\mathbf{r} A e^{-2(z/w)^2} [n_0(\mathbf{r}) + n_{\mathrm{th}}(\mathbf{r})], \tag{5.10}$$

where A is a factor describing the dimple depth, which is proportional to laser power and w is the beam waist of the laser beam. After solving Eqn. (5.10) for the final temperature for which $E = E_i + \Delta E$, the condensate fraction can be determined.

5.1.2 Quantum Kinetic Theory

In a second series of experiments the actual condensation dynamics were investigated. For these experiments the dimple is turned on suddenly and the system is then allowed to evolve for various times before the condensate fraction is measured. This is done for both wide and narrow dimples for two different fixed dimple depths. To describe these experiments a truly dynamic theory is needed which in this case is quantum kinetic theory. In particular the ergodic Boltzmann equation was used, which incorporates two-particle collisions, the condensate mean-field and three body losses [85]. To my knowledge this is the first experiment in which a single-component condensate is formed without evaporatively cooling across the transition temperature for Bose-Einstein condensation.

Initially the thermal Bose gas in the magnetic trap is in an equilibrium state. This state in the initially purely harmonic potential is then turned into a highly non-equilibrium state when the additional Gaussian dimple potential is switched on. To calculate the condensation dynamics it is first necessary to calculate the corresponding energy densities $n(\epsilon, t = 0)$, at the moment when the dimple is first turned on but no further evolution has happened yet. This energy density is then evolved in time to find a final state, using an ergodic quantum Boltzmann equation, which is described in further detail in [45, 86].

The Boltzmann transport equation, a partial differential equation that describes phase space evolution of a distribution function $f(\mathbf{r}, \mathbf{p}, t)$, serves as a starting point for the ergodic quantum Boltzmann equation (EQBE). To get to the EQBE two additional assumptions have to be made. First, the quantum nature of elastic two particle collisions has to be taken into account. This is done via the incorporation of Bose-enhancement factors, which account for the fact that bosonic particles are more likely to occupy states that are already occupied. These Bose-enhancement factors are described in more detail in Appendix C of reference [46]. Second, to make numeric calculations possible the ergodic assumption has to be invoked. What this assumption says is that on average every particle will spend the same amount of time in all areas of phase space given a long enough time frame. For the large many-body system that is a BEC this means that instead of the three parameters space, momentum and time, the distribution function will only depend on energy and time:

$$f(\mathbf{r}, \mathbf{p}, t) = f(E(\mathbf{r}, \mathbf{p}, t), t). \tag{5.11}$$

It has to be noted though that the energy still depends on space and momentum. The EQBE then describes the evolution of the density of energy states

$$n(\epsilon, t) = \int \frac{d\mathbf{r} d\mathbf{p}}{(w\pi\hbar)^3} \delta(\epsilon - \epsilon_{\mathrm{th}}(\mathbf{r}, \mathbf{p}, t)) f(\mathbf{r}, \mathbf{p}, t) = g(\epsilon, t) f(\epsilon, t), \tag{5.12}$$

where $f(\epsilon, t)$ describes the energy distribution and $g(\epsilon, t)$ the density of states given by

$$g(\epsilon, t) = \int \frac{d\mathbf{r} d\mathbf{p}}{(w\pi\hbar)^3} \delta(\epsilon - \epsilon_{\mathrm{th}}(\mathbf{r}, \mathbf{p}, t)). \tag{5.13}$$

It has to be pointed out that $\epsilon_{\mathrm{th}}(\mathbf{r}, \mathbf{p}, t)$ is the same semiclassical excitation energy used in Eqn. (5.2) only that the the mean-field contribution of the thermal cloud is neglected. Setting $n_{\mathrm{th}} = 0$ is necessary to make the equation computationally tractable. It has to be noted though that this approximation is used only for calculating the effective potential felt by the atoms since the contribution by the thermal atoms is small. For the calculations of all other quantities $n_{\mathrm{th}} \neq 0$. The same is true for the calculation of the mean-field of the condensate, which again uses the Thomas-Fermi approximation similar to Eqn. (5.4) only neglecting the mean-field contribution of the thermal cloud. More information on this process and the implementation of the effects of three body losses as well as two particle collisions are found in [46].

5.2 Measurements On Equilibrium Thermodynamics

In a first series of experiments the predictions of semiclassical Hartree-Fock theory are compared to measurements taken with a wide and a narrow dimple. (Some of these results are already reported in [39].) In both cases condensate fraction and temperature are plotted as a function of dimple depth for both a sudden and a quasistatic turn-on. The only fitting parameters used in the theoretical predictions are the initial temperature and atom number (as described in section 5.1.1), which were derived from experimental measurements and constrained to lie within measurement uncertainties.

The measurements start with a thermal cloud of $N = (6.25 \pm .25) \times 10^5$ atoms in a magnetic trap at an initial temperature of $T_i = (215 \pm 2)$nK just above $T_c = 215$nK, as calculated from the ideal gas transition given by Eqn. (2.6). The atom numbers and temperatures are obtained from absorption images as described in section 3.6. The uncertainties are obtained from multiple measurements under the same conditions taking the standard deviation in the measurements to be the uncertainty. Onto this initial situation a red-detuned 840nm laser beam is applied which intersects the magnetic trap at the centre as shown in Fig. 5.1. This laser is turned on either suddenly or in a quasistatic fashion, which means that the state of the condensate is a succession of equilibrium states. This is very similar to an adiabatic process where no heat is exchanged between the system under investigation and its surroundings only that a quasistatic process might allow some small exchange of heat under certain circumstances but has to stay reversible. The laser beam is focused in one dimension to a focal size of 32μm for the wide and 11μm for the narrow dimple ($1/e^2$ half-widths). This compares to a thermal cloud length of $\sim 400\mu$m in the axial direction. In the other direction a cylindrical lens is used to expand the beam to a size of 350μm for the wide and 220μm for the narrow dimple which compares to a cloud width of 6μm. This means that the intensity can be well approximated to be constant in this dimension and therefore the contribution to the trapping potential from the added dimple in that direction can be neglected.

To make sure the dimple is ramped on in a quasistatic fashion the power is ramped on at a rate of 70nK/s before being held constant to give the condensate time to equilibrate for about 300ms. For the sudden turn on the potential is ramped up in less than 100μs and then held constant for 1s. The difference in equilibration times given to the condensate before imaging results from the fact that the sudden turn on is a much more violent process than the quasistatic turn on, therefore requiring more time to reach equilibrium. The fact that equilibrium was reached was verified by taking measurements for longer wait times after the potential turn on without observing any change. Measurements were performed with a time of flight of 20.3ms after all trapping potentials have been switched off. Information about the temperature is gained from fits to the thermal wings of the resulting distribution while the condensate fraction is determined from a bimodal fit to a density cross section of the cloud.

For the wide dimple it is found that both the adiabatic and the sudden turn-on show good agreement between theoretical predictions and experiment. Data points consist of four measurement averages and the error bars in Figure 5.3 are statistical errors. Best fits were achieved using $N = 6.5 \times 10^5$ and $T_i = 216$nK. It can be seen that the results for the adiabatic and the sudden turn-on are almost indistinguishable which stems from the fact that only a small fraction of the thermal cloud would be drawn into the dimple because of its very low depth of only about 210nK.

For the narrow dimple case shown in Figure 5.4 it is found that the quasistatic case shows good agreement between theory and experiment. In the case of a sudden turn-on, however, the condensate fractions predicted by theory are smaller than those actually measured in the experiment. The initial conditions for those measurements were $T_i = (160 \pm 2)$nK and $N = (2.60 \pm .15) \times 10^5$ for the quasistatic case, while the initial conditions for the sudden turn-on are $N = (2.10 \pm .15) \times 10^5$ and $T_i = (168 \pm 2)$nK as given by the experiment. Since the measurements of the sudden turn-on case do show significant disagreement between theory and experiment it is much harder to find good initial conditions for the calculations. The best fit shown is for $N = 2.25 \times 10^5$ and $T_i = 166$nK and it can be seen that no good agreement between theory and experiment is found for the sudden turn-on case within the experiments uncertainties even though better fits can be obtained using values of N and T_i outside allowed error bars. One possible explanation for the discrepancy between calculated

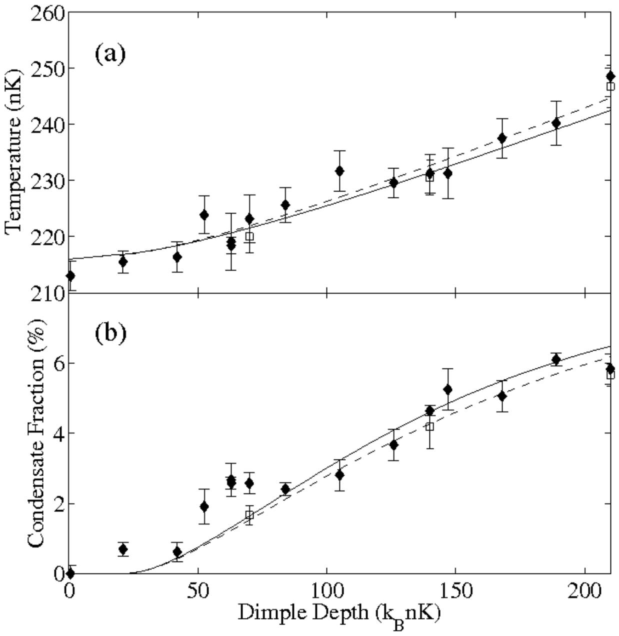

FIGURE 5.3: Temperature (a) and condensate fraction (b) plotted versus dimple depth to compare theory and experiment in a wide dimple potential. Data for a quasistatic turn-on is shown by solid lines and diamonds, data for a sudden turn-on by dashed lines and squares. All experimental data points are averages over four measurements and the error bars are statistical errors.

and observed condensate fractions is that the density of the gas might not be fixed during the turn-on. This would be the case if the turn-on time was not sufficiently quick, leaving the atom cloud enough time to adjust to the change in the potential. This would mean that the sudden turn on would actually have to be considered “slow“. Since the measured values fall in between what is predicted by the two theoretical curves shown, it would make sense to assume that intermediate conditions are the cause of the unexpected behaviour. Physically, a slower turn-on time would lead to a reduced increase in total energy and therefore to a reduced increase in temperature and hence to a larger condensate fraction compared to the prediction of the model. This is also what is observed in the experiment. To verify if this is the case, however, a fully dynamical treatment of the situation would be necessary. This is unfortunately beyond the scope of the semiclassical theory presented here.

An interesting feature found in the narrow dimple experiments is the fact that there is an optimal depth for condensate formation. In the case of the quasistatic turn on around 750nK and in the sudden turn-on case somewhere between 400nK and 800nK where the theoretical prediction puts that optimum at around 400nK. The situation can be explained as follows.

In the situation where the dimple is not yet turned on the energy of the ground state would be slightly above the chemical potential as the cloud is still thermal slightly above T_c (see Fig. 5.5). As the cloud is still above the critical temperature no condensation occurs at this point. Upon turning on a very weak dimple the added dimple potential initially only acts as a perturbation to the harmonic trap which means that to a first approximation both the

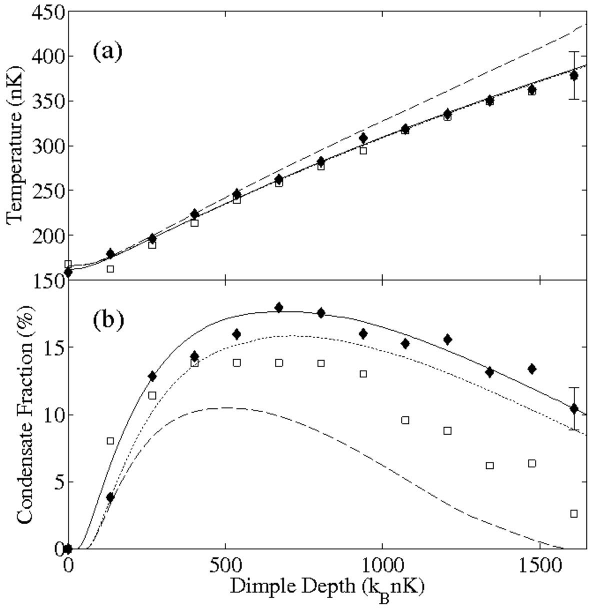

FIGURE 5.4: Temperature (a) and condensate fraction (b) plotted versus dimple depth to compare theory and experiment in a narrow dimple potential. Data for a quasistatic turn-on is shown by solid lines and diamonds, data for a sudden turn-on by dashed lines and squares. All experimental data points are single measurements except for one four data point measurement at dimple depth $A/k_B = 1610$nK to show the standard deviation of the mean.

chemical potential and the ground state energy will remain unchanged while the translational ground state is ever so slightly lowered. When lowering the dimple potential further the energy of the ground state will be lowered and when this energy approaches the chemical potential, which will remain largely unchanged, an onset of condensation can be observed as the phase space density is increased leading to condensate formation. The condensate will start to grow for deeper dimple depths until a depth is reached such that a significant fraction of the atoms will be in the dimple resulting in changes in μ and T that can no longer be ignored. Once the depth is deep enough almost all of the atoms will be in the dimple where no further condensate fraction develops. This is due to the fact, that the dimple in its centre can be approximated as a harmonic trap which is simply compressed in comparison to the harmonic potential formed by the magnetic trap but does not have an increased phase space density as compared to the magnetic trap. It is well known that simply compressing a harmonic trap does not change the phase space density [87]. This is because while the density is increased that effect is counteracted by an increase in temperature such that the product of the density and the de Broglie wavelength $n\lambda^3$ remains constant. Without the increase in phase space density, however, no further condensate fraction is formed.

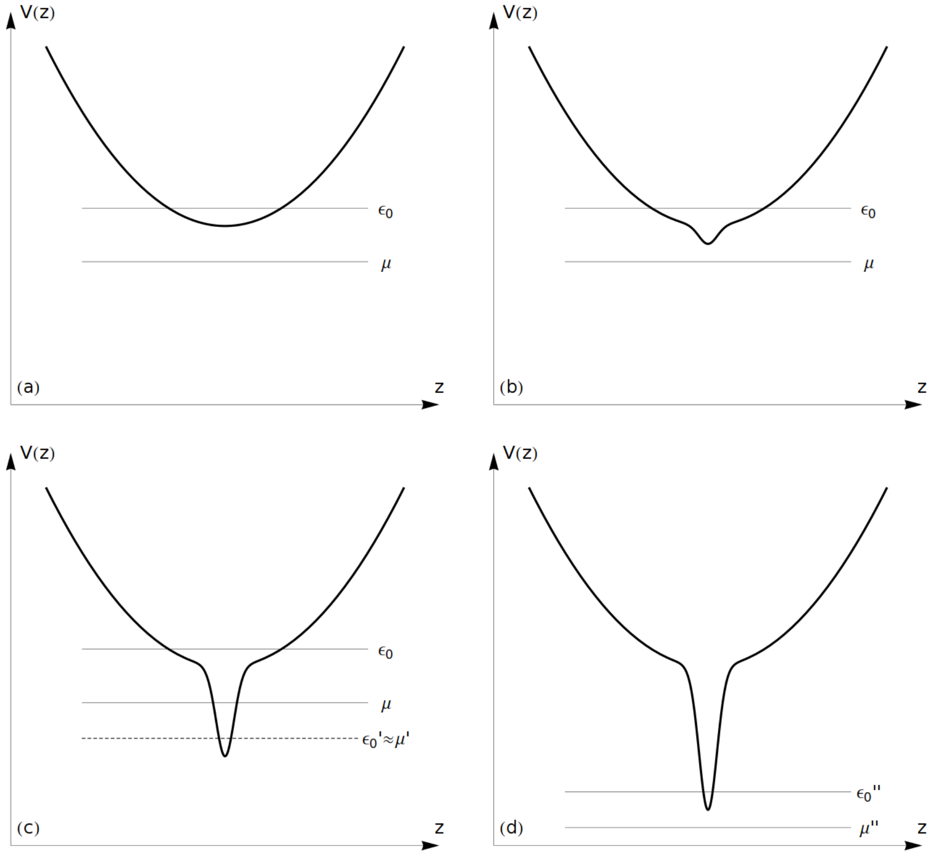

FIGURE 5.5: (a) Before the dimple is turned on the atoms are confined by a purely magnetic potential with the chemical potential μ well below the ground state energy of the trap ϵ_0, as the system is above T_c. (b) When a shallow dimple is turned on it acts as a perturbation to the harmonic trap leaving both μ and ϵ_0 basically unchanged. (c) When the dimple reaches a sufficient depth the new ground state energy ϵ_0' is shifted much further than the chemical potential μ', which remains nearly constant. A condensate starts to form for $\epsilon_o' \approx \mu'$. (d) When all the atoms are in the dimple the dimple bottom can be approximated by another harmonic potential thus leading to compression of the thermal cloud but not increasing phase space density. The situation mirrors that in (a) with μ'' well below the new ground state energy of the trap ϵ_0''.

5.3 Measurements On Condensation Dynamics

In a further series of experiments the predictions of quantum kinetic theory are compared to measurements taken with a wide and a narrow dimple. In both cases condensate fraction is plotted depending on the time since the sudden turn on of the dimple potential for both a wide and a narrow dimple potential that is suddenly switched on. The only fitting parameters used in the theoretical predictions are the initial temperature and atom number (as described in section 5.1.2), which were derived from experimental measurements and constrained to lie within measurement uncertainties.

The results for the wide dimple measurements are shown in Fig. 5.6. For the measurements we begin with a thermal cloud of $N = (6.25 \pm 25) \times 10^5$ atoms at a temperature of $T_i = (215 \pm 2)$nK. The dimple is ramped up in less than 100μs and then kept constant. During these varying times the condensate has time to equilibrate for up to 1s before imaging. The data points are averages over four measurements and the two curves are for dimple depths of 70nK (solid line and diamonds) and 140nK (dashed line and squares) respectively. We find good agreement between theory and experiment for both dimple depths. Best fits are obtained for $N = 6.10 \times 10^5$ and $T_i = 216$nK.

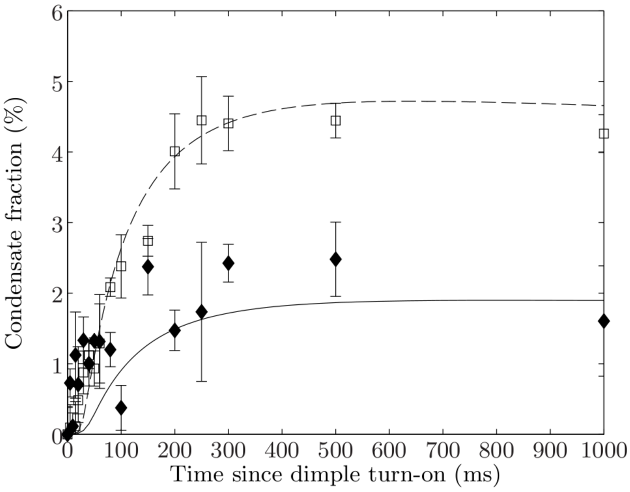

Figure 5.6: Condensate fraction plotted versus equilibration time to compare quantum kinetic theory and experiment in a wide dimple potential. Data for a dimple depth of 70nK is shown by solid lines and diamonds, data for a dimple depths of 140nK by dashed lines and squares. All experimental data points are averages over four measurements and the error bars are statistical errors.

Measurements for a narrow dimple are shown in Fig. 5.7. The measurements begin with a thermal cloud of $N = (1.87 \pm 7) \times 10^5$ atoms at $T_i = (154 \pm 6)$nK. The dimple is again ramped up in less than 100μs to a depth of 660nK before keeping the dimple depth constant for varying equilibration times of up to 1s before imaging. Data points are again four measurement averages with statistical errors as indicated.

Best fits in Fig. 5.7 were achieved using $N = 1.94 \times 10^5$ and $T_i = 148$nK. Generally good agreement is found between experimental results and theoretical predictions even though there is a slight discrepancy in condensate formation rates, where the rate predicted by theory is slower than what is observed in the experiment. This could be due to non-ergodicity when turning on the dimple potential since the ergodic hypothesis applies only to equilibrium systems. It states that in an ergodic system at equilibrium one assumes that over sufficiently long times, a system will spend time in all accessible microstates, with the time spent in each microstate being proportional to the statistical probability of that state. When the dimple potential is suddenly turned on, the system is very far from equilibrium, so it will also behave non-ergodically until it has reached a new equilibrium. Equilibrium is therefore a necessary but not sufficient condition for ergodicity. When projecting the pre-dimple

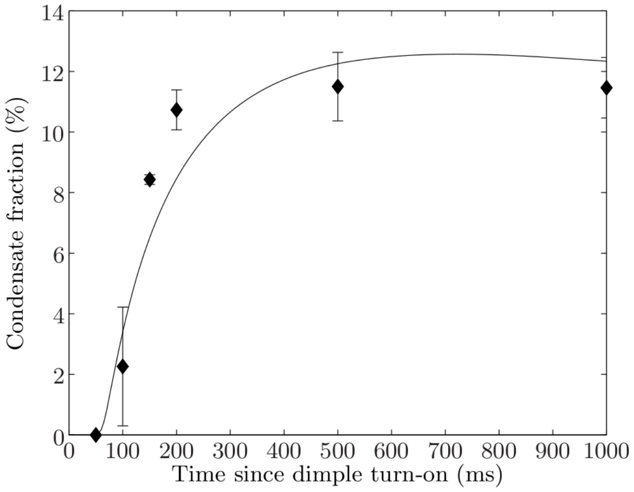

FIGURE 5.7: Condensate fraction plotted versus equilibration time to compare quantum kinetic theory and experiment in a narrow dimple potential. Data is shown for a dimple depth of 660nK. All experimental data points are averages over four measurements and the error bars are statistical errors.

phase space using the density of states after dimple turn-on a shift in energy densities is caused that is highly dependent on position. This in turn means that the state of the system after dimple turn-on is a non-equilibrium, non-ergodic state stretching the bounds of validity for the ergodic assumption. Condensate fraction at final equilibrium, however, is in good agreement which is consistent with the results of equilibrium thermodynamics where a discrepancy between theory and experiment was found ony for dimple depths above 700nK (see Fig. 5.4). A feature that is found for the narrow dimple case that was not observed in the case of wide dimples is a delay in condensate formation of about 50ms which is correctly predicted by theory.

5.4 Measurements On Rethermalization Dynamics

In a further experiment we are able to report preliminary results on the rethermalization of Bose-Einstein condensates in different trapping geometries for non-zero temperature. For these experiments a BEC was created in a magnetic trap with trapping frequencies of 160Hz ×6.8Hz. Then, a light sheet with a beam waist of 11μm intersecting the long axis of the magnetic trap was adiabatically turned on to create a dimple potential. This situation was used as the starting point for the actual experiment which consisted in a sudden switch-off of the dimple potential and subsequent evolution in the magnetic trap for varying hold times. After the equilibration time the atom clouds were imaged after a time of flight of 13.54ms. Measurements were taken for two different dimple depths of 805nK and 1340nK.

There is currently no theory for these experiments since the quantum kinetic energy approach presented in section 5.1.2 cannot be used. This is because quantum kinetic theory treats the energy distribution of the atoms by dividing the number of atoms into different bins with energy range E to $E + \Delta E$, where the bin (and only that bin) with the lowest energy, $E = 0$, represents the condensate. This is equivalent to treating the condensate as a steady-state equilibrium wavefunction (e.g. the Thomas-Fermi profile), neglecting collective modes such as solitons, vortices or breathing modes for example. Since these collective modes are expected to play a dominant role in the rethermalization process, quantum kinetic theory cannot be used to model it. The theory that could model these experiments would have to encapsulate both non-equilibrium condensate dynamics and a changing occupation of the condensate since the number of condensate atoms will vary with temperature. One such example is the Stochastic Projected Gross-Pitaevskii Equation (SPGPE) [88, 89], however, the SPGPE does not encapsulate the non-equilibrium dynamics of the thermal cloud which it simply describes by a temperature and chemical potential. While these could be made time dependent to gradually shift from the initial to the final state this means that the thermal cloud has to be assumed to be in a quasi-equilibrium with the BEC which might not be the case.

Plotting the condensate fraction depending on the hold time in the magnetic trap after dimple turn-off we observe a breakdown of the initial condensate fraction and a subsequent revival (see Figs. 5.8 and 5.10). The breakdown happens on a very short time scale $<$ 10ms for both dimple depths. The revival happens on a time scale of about 150ms for both dimple depths. Therefore, we assume that rethermalization is dependent on collision processes within the BEC which happen on a time scale of the order of the inverse trapping frequency of the magnetic trap in which the rethermalization process takes place. Taking the inverse of the observed rethermalization time results in a trapping frequency for the long axes of the magnetic trap of about 6.6Hz, which agrees well with the expected trapping frequency of the magnetic trap in that direction of 6.8Hz.

The temperature curves show a steady rise to a temperature above the initial temperature. The fact that the final temperature is higher than the initial temperature is consistent with the fact that by removing the dimple potential suddenly, energy is added to the condensate, which after some equilibration time would add to the temperature of the condensate.

Condensate fractions are calculated by fitting a Thomas-Fermi profile to the peak in the intensity cross section through the density peak in the absorption images and comparing the number of atoms in the Thomas-Fermi profile to a normal distribution fitted to the thermal atoms visible in the cross section. Temperatures of the condensate are calculated from the spread of the normal distribution. Cross sections of the absorption data with Thomas-Fermi and Gaussian fits are shown in Fig. 5.9 for condensates held in the magnetic trap for 0ms, 50ms, 100ms and 1000ms after turning off a dimple potential of 805nK depth. Fitted curves are in good agreement with the absorption data.

When the dimple is removed and the condensate is left to rethermalize in the magnetic trap, two different excitations are expected. On the one hand a centre-of-mass oscillation is to be expected since the alignment between the magnetic trap and the dimple, even though done carefully, will not be perfect leading to a sloshing of the atomic cloud in the new trapping

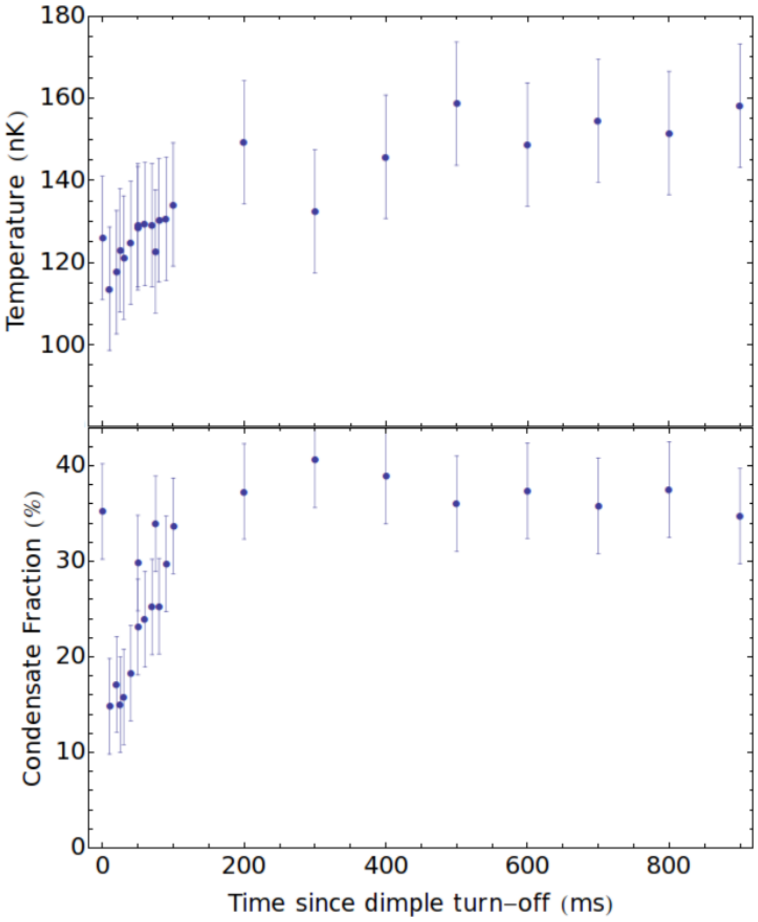

FIGURE 5.8: Temperature and condensate fraction plotted versus time after dimple turn-off to study the rethermalization dynamics of non-zero temperature BEC. The data set shown was taken with a dimple depth of 805nK. All data points are averages over three measurements and the error bars are statistical errors.

geometry with the trapping frequency of the remaining trap. To check for centre-of-mass movement the expectation value of the condensate position, $\langle z\rangle = \sum_i z_i \mathrm{OD}_i$, was calculated, where z is the position on the camera in pixels and OD_i is the optical density at position z. A plot of the expectation value of the position can be found in Fig. 5.11. It can be seen that the condensate moves from its initial position in the dimple to the centre of the remaining magnetic trap in the first 100ms. No oscillation is observed. One possible reason for this could be damping due to the thermal cloud. However, no proof for this assumption can be presented. To verify this assumption measurements with lower thermal fractions would have to be performed to see if an oscillation occurs when the condensate is more pure.

On the other hand a form oscillation is expected as the atom cloud will start to expand when released from the tight trapping provided by the dimple until it reaches the walls of the magnetic trapping potential where it will be reflected. These form oscillations can be clearly observed in a one-dimensional GPE calculation that shows the BEC in the magnetic trap after the dimple is turned off. The expected amplitude for the in-trap case is of the

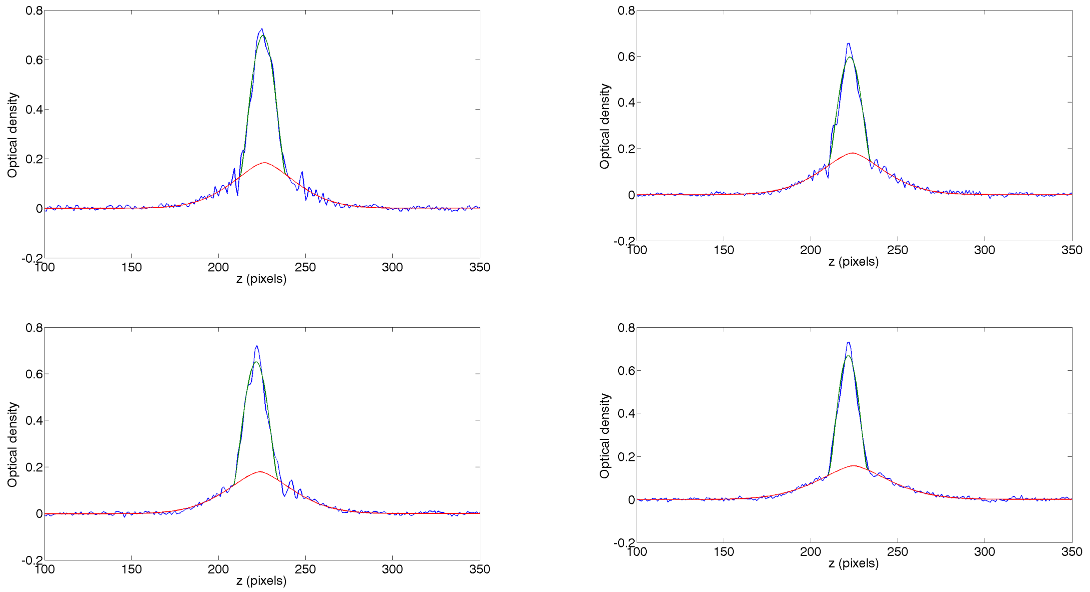

Figure 5.9: Cross sections of atomic clouds in a magnetic trap 0ms (top left), 50ms (top right), 100ms (bottom left) and 1000ms (bottom right) after switching off an optical dimple potential of 805nK depth (blue line). Also shown are a parabolic Thomas-Fermi fit to the peak of the intensity distribution (green) as well as a Gaussian fitted to the thermal gas (red). One pixel on the camera corresponds to 4.7μm.

order of an increase in Thomas-Fermi width by a factor of 48 as shown in Fig. 5.13 before the magnetic trap is switched off. To check for this form oscillation a plot of the Thomas-Fermi width is shown in Fig. 5.12 with a sinusoidal fit to the data. Contrary to what was expected the plot shows no form oscillations with an amplitude as big as expected from the in-trap calculations. A sinusoidal best fit to the data points gives an oscillation frequency of 4.6Hz with an amplitude of 1.1μm as opposed to the expected oscillation with the trapping frequency of the magnetic trap of 6.8Hz. However, fits corresponding to a range of frequencies around 4.6Hz are possible, such that the oscillation period could be within the uncertainty limits of the experiment. The difference in oscillation amplitude was initially thought to be another sign that the thermal cloud might play an important role by damping the form oscillations, however, no decay in the amplitude is visible making damping by the thermal cloud unlikely.

In the rethermalization experiments the BEC is released from a tight trapping potential in the dimple into a wider trapping potential provided by the magnetic trap before a free expansion without any remaining trapping potentials. Given the dramatic change in trapping geometry, the situation warrants further investigation. A possible explanation for the lack of agreement between observed and expected oscillations in the magnetic trap is that, depending on the phase of the oscillation at the time of release of the condensate, oscillations happening in the magnetic trap might falsify the width of the condensate after free expansion. To check whether this is the case a theory devised by Y. Castin and R. Dum is used which allows us to calculate the size of BECs in time dependent traps and after free

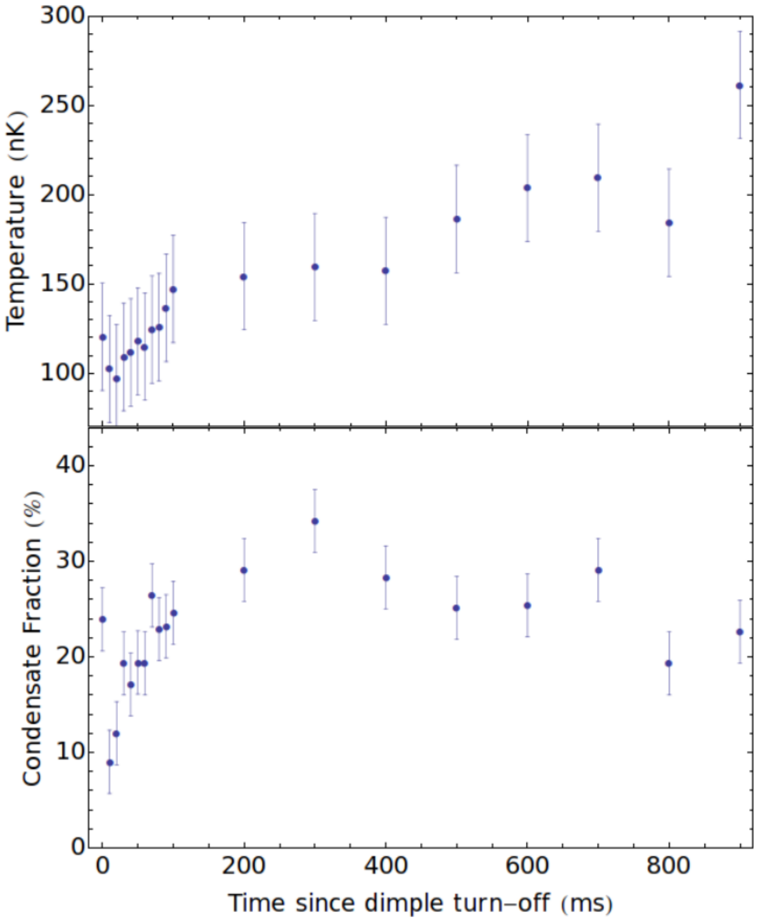

FIGURE 5.10: Temperature and condensate fraction plotted versus time after dimple turn-off to study the rethermalization dynamics of non-zero temperature BEC. The data set shown was taken with a dimple depth of 1340nK. All data points are averages over three measurements and the error bars are statistical errors.

expansion [90].

Castin and Dum provide a theory that allows one to calculate the width of a Bose-Einstein condensate in time dependent traps from first principles. For their theory they assume that once released from a tighter trapping geometry into a wider trap or into free expansion a BEC will expand self-similar in a Thomas-Fermi shape until hindered by the walls of a remaining trapping potential. They derive a time evolution for the classical radii R_i where the density of the Thomas-Fermi profile vanishes that scales as [36]

$$R_i(t) = R_i(0)b_i(t) = \sqrt{\frac{2\mu}{m\omega_{0i}^2}}b_i(t). \tag{5.14}$$

The trapping potential in direction $i = x$, y, z is described by the trapping frequency at time t, ω_i, (where ω_{0i} denotes the trapping frequency at time $t = 0$) and the scaling parameter in direction i, b_i, evolves according to coupled differential equations

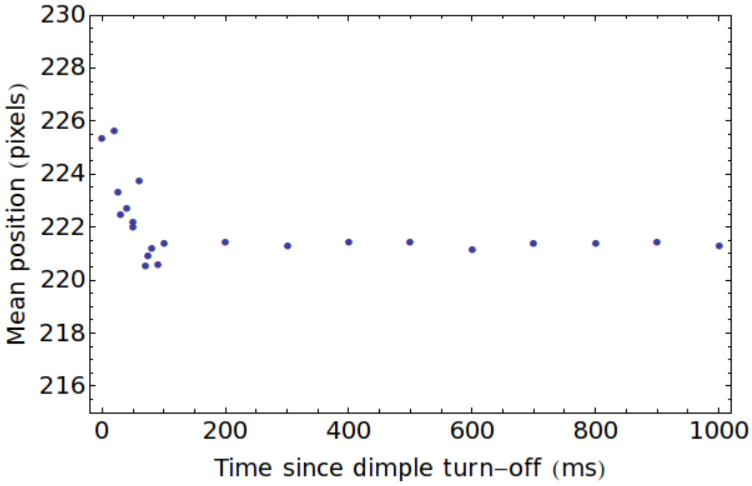

FIGURE 5.11: Expectation value of the condensate position plotted versus time after dimple turn-off for a dimple depth of 805nK to check for centre-of-mass movement of the condensate. The condensate moves from its initial position in the dimple to the centre of the magnetic trap which was slightly misaligned compared to the dimple position. One pixel on the camera corresponds to 4.7μm.

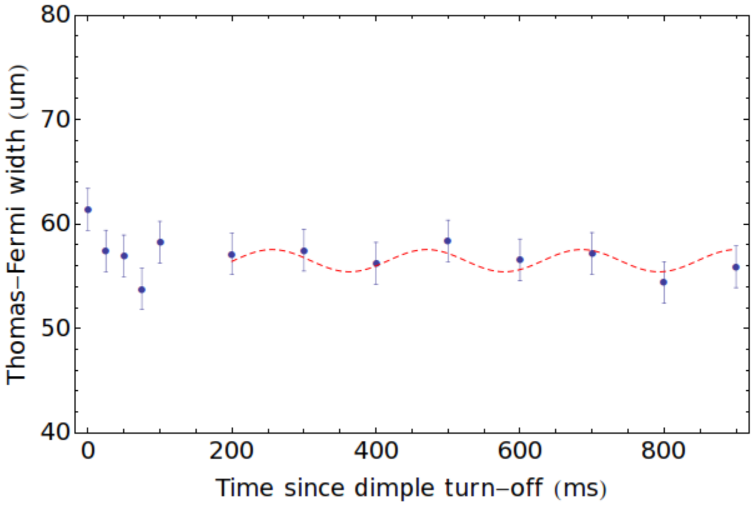

FIGURE 5.12: Thomas-Fermi width of the condensate plotted versus time after dimple turn-off for a dimple depth of 805nK to check for form oscillations of the condensate. Also shown in red is a sinusoidal fit disregarding the first data points after dimple turn-off. Expected were shape changes with an oscillation frequency of the order of the trapping frequency of the magnetic trap (6.8Hz) and an amplitude of order factor 50 change in Thomas-Fermi width. Observed is an oscillation with a frequency of 4.6Hz and an amplitude of 1.1μm.

$$\ddot{b}_i + \omega_i^2 b_i - \frac{\omega_{0i}^2}{b_i b_x b_y b_z} = 0. \tag{5.15}$$

Using these equations Castin and Dum provide an analytic solution for the width of a condensate after release from a harmonic trap including free expansion [90]. The situation in the rethermalization experiments proves more complicated and no analytic solution could be found so that the set of differential equations had to be solved numerically. For this the scaling parameters b_i were calculated after turning off the dimple potential, holding the condensate in the magnetic trap for varying hold times and a free expansion. An example of the results of such a calculation is shown in Fig. 5.13. The parameters for Fig. 5.13 were chosen to match those of the experiment, that is a magnetic trap with trapping frequencies $\omega_z = 6.8$Hz and $\omega_{x,y} = 160$Hz, which is overlapped with an additional potential created by a laser beam with a trapping frequency in z-direction of $\omega_l = 240$Hz. The laser beam is turned off at time $t = 0$ and the oscillation of the scaling parameters in the axial (z) and radial (x, y) direction of the elongated trap can be observed in the magnetic trap until the magnetic trap is turned off and the BEC left to free expansion after time $t = 0.5$ms. The two graphs shown are the axial (left) and radial (right) directions of the BEC. In Fig. 5.14 we plot the scaling parameters for varying hold times in the magnetic trap after the dimple potential has been switched off for a dimple of 805nK depth including the free fall expansion. These allow a direct comparison to the change in Thomas-Fermi width of the condensate when they are normalized to the size of the condensate without any hold time in the magnetic trap after dimple turn-off. The simulation shows oscillations that are consistent with the in-trap calculations shown in Fig. 5.13.

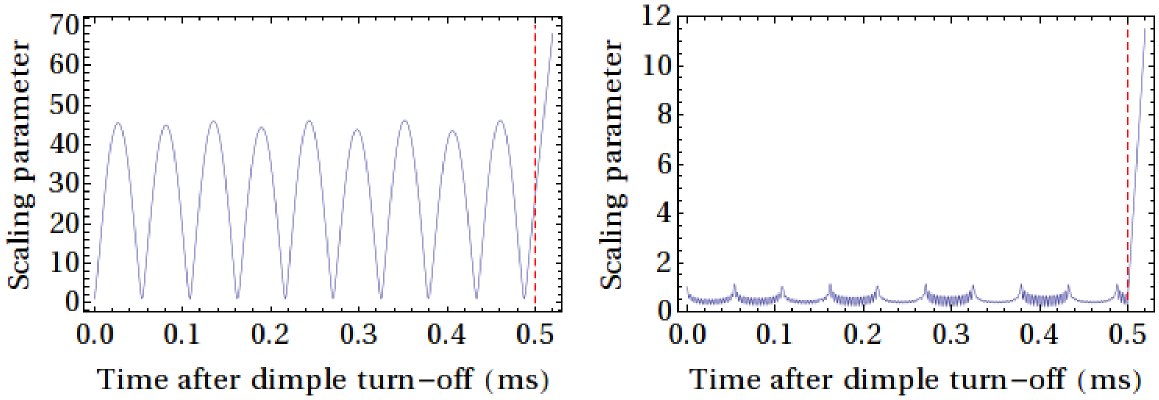

FIGURE 5.13: Time evolution of scaling parameters of a BEC released from a dimple trap at time $t = 0$ into a much wider magnetic trap including free expansion. The time when the magnetic trap is switched off is indicated by the red dashed line. The scaling parameter in the z-direction is shown on the left and the scaling parameter in x- and y-directions is shown on the right.

Looking at the time scale of Fig. 5.14 shows that the oscillations are so fast that no meaningful comparison between the calculations and the data points is possible as the data would be undersampling the oscillations by two orders of magnitude. Any slight errors in the measured trapping frequencies would therefore lead to large changes in the expected value of the relative condensate width rendering any comparison meaningless.

In conclusion we can report on the observation of a break down in condensate fraction with subsequent recovery which cannot currently be explained by existing theories. To further the understanding of rethermalization dynamics a full three-dimensional theory that also takes into account the existence of a thermal component would be desirable. While this

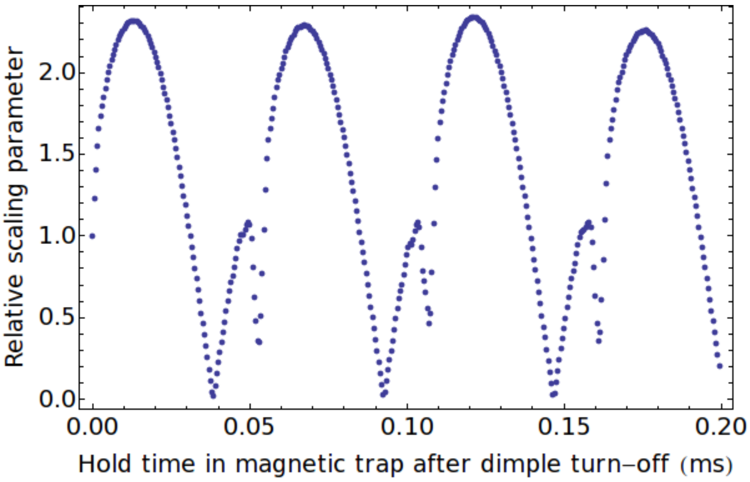

FIGURE 5.14: Scaling parameters normalized to the value of the scaling parameter without any hold time in the magnetic trap shown as a function of varying hold times in the magnetic trap after the dimple is turned off including free expansion of the condensate. The depth of the dimple potential before turn-off is 805nK. The oscillations of the scaling parameter after free expansion are consistent with the calculated oscillations in the trap which are shown in Fig. 5.13

.

theory does not exist, further measurements at lower temperatures are suggested to test the influence of thermal atoms on the observed behavior. These measurements are expected to give better agreement with current theories.

6

Critical Velocity Of Superfluidity In BEC

Superfluidity was first discovered in 1938 by Kapitza [11] and independently Allen and Misener [10]. What they observed was that liquid helium when cooled below a transition temperature of 2.17K underwent a phase transition and exhibited flow without viscosity - a "super" flow. This superflow was most impressively shown by Reppy and Depatie in 1964 when they set up a flow in a torus shaped vessel which showed no decay in angular velocity over a period of 12 hours [12]. Other unusual behaviour that was observed includes propagation of temperature waves at constant density, which is now known as second sound, film creep, where superfluid helium can leave a vessel by flowing over its walls, and irrotational flow, where rotations are only possible via quantized vortices. Another milestone in the understanding of superfluid behavior was reached when Castelijns *et al.* [13] observed a critical velocity above which very high dissipation sets in while the system below that critical velocity did not show any significant dissipation. Castelijns and coworkers were also able to identify this critical velocity with the Landau critical velocity described in more detail in section 6.1.

As of today a microscopic theory of superfluid helium remains elusive due to the strong interactions in the system. London was the first to draw a connection between the theory of Bose-Einstein condensation and superfluid behavior [6]. While this theory was developed for an ideal gas, which according to the Landau criterion cannot exhibit dissipation less flow, it is now accepted that superfluidity is connected to a macroscopic occupation of one and the same wavefunction. In contrast to the strong interaction in superfluid helium, interactions in dilute Bose-condensed gases are weak allowing accurate modelling. This modelling can be done by using the Gross-Pitaevskii equation or with more advanced quantum simulation techniques.

This chapter will start out by recapitulating Landau's theory of superfluidity, the first theory that explained the existence of a critical velocity above which superfluidity breaks down. It will then proceed by summarizing previous experimental results on measuring this critical velocity before reporting the results of one and two dimensional numerical simulations showing the existence of a critical velocity lower than the critical velocity expected from Landau's theory. The chapter will finish by presenting progress on experiments aiming to measure the critical velocity in a Bose-Einstein condensate.

6.1 Superfluidity

When trying to understand superfluidity, probably the easiest approach is to use Landau's theory of superfluids. (The description given here follows the approach used by Pitaevskii and Stringari [35].) In his theory a major role is played by the transformation rules for energy and momentum under Galilean transformations. Considering a Bose-Einstein condensed system in its ground state with energy E and momentum $\mathbf{P}$ in some reference frame S, when transferred into a reference frame S', moving with velocity V relative to S, standard Galilean transformation results in an energy and momentum, respectively, of the liquid of

$$E' = E - \mathbf{P}V + \frac{M}{2}V^2, \qquad \mathbf{P}' = \mathbf{P} - M\mathbf{V}, \tag{6.1}$$

where M is the total mass of the fluid.

Let us now consider a uniform BEC with a massive obstacle that is being dragged through the liquid at a constant velocity v. If the fluid is viscous the drag force between obstacle and fluid will lead to dissipation and therefore heating of the BEC. In the semi-classical Landau model the only way dissipative processes can take place would be via the creation of elementary excitations. If one of these excitations with momentum $\mathbf{p}$ and energy $\epsilon(\mathbf{p})$ is created the total energy of the fluid in its rest frame is

$$E = E_0 + \epsilon(\mathbf{p}). \tag{6.2}$$

According to Eqn. (6.1) the energy in the frame of reference where the barrier is at rest is then given by

$$E' = E_0 + \epsilon(\mathbf{p}) - \mathbf{p}v + \frac{M}{2}v^2. \tag{6.3}$$

Keeping in mind that the barrier has zero momentum in its own frame of reference and that therefore the ground state has zero momentum in this frame of reference, the ground state energy in the frame of reference where the barrier is at rest is given by

$$E' = E_0 + \frac{M}{2}v^2. \tag{6.4}$$

Consequently the energy needed to create an excitation in the frame moving with the barrier is given by the difference between Eqns. (6.4) and (6.3), which is $\epsilon(\mathbf{p}) - \mathbf{p}v$, where $\mathbf{p}$ is the momentum carried by the fluid in the presence of an excitation. This process is possible only when it is energetically favourable, i.e. if the energy to create an excitation is negative:

$$\epsilon(\mathbf{p}) - \mathbf{p}v < 0. \tag{6.5}$$

This is possible if $v > \epsilon(\mathbf{p})/\mathbf{p}$ and therefore results in Landau's critical velocity

$$v_c = \min\left(\frac{\epsilon(\mathbf{p})}{\mathbf{p}}\right) = \sqrt{\frac{gn}{m}}, \tag{6.6}$$

below which it is impossible to create excitations in the BEC. In this equation g is the physical coupling constant already used in section 2.3.1, n is the density of the condensate and m the atomic mass of the element used in an experiment. As shown in section 2.3.1 this is exactly equal to the speed of sound of the system c. As a result, there is no mechanism for a dissipation of energy and hence, no mechanism to degrade the motion of the condensate for velocities lower than Landau's critical velocity. The liquid becomes superfluid.

6.2 Previous Experiments In BEC

In this section I will briefly review two experiments that have shown the existence of a critical velocity for superfluidity in BEC.

The first work that showed a signature of a critical velocity for superfluidity in Bose-Einstein condensates was undertaken by Raman *et al.* [47]. In this work a blue-detuned Gaussian laser beam mimics a macroscopic obstacle moving through a Bose-Einstein condensate. The experimental setup is shown in Fig. 6.1. The laser beam repels the atoms from its focus, thus creating a moving boundary condition. The laser is then scanned back and forth for the barrier to move through the condensate at varying speeds. The effective velocity of this obstacle is then controlled by varying the amplitude and frequency with which the laser beam oscillates within a Bose-Einstein condensate. To observe the onset of friction within the superfluid Bose-Einstein condensate as a sign of a critical velocity a time-of-flight distribution was recorded after 35ms using absorption imaging and the condensate fraction N_0/N and temperature were determined by fitting to a bimodal velocity distribution. This experiment was done using sodium atoms.

The results from this experiment showed no heating for a laser beam that was kept stationary. Once the laser beam was spatially scanned two distinct regions of behaviour could be observed. In the first region where the laser beam was scanned slowly the thermal fraction remained approximately constant even though there was considerable noise in the condensate fraction measurement. In the second region, the thermal fraction increased as a function of obstacle velocity. The crossover between those two regions was observed at an average speed of about 1.6 mm/s. This velocity was compared to the speed of sound in the system which according to Landau's criterion should be giving the critical velocity. The speed of sound was found to be 6.2 mm/s, almost 4 times larger than the observed critical velocity.

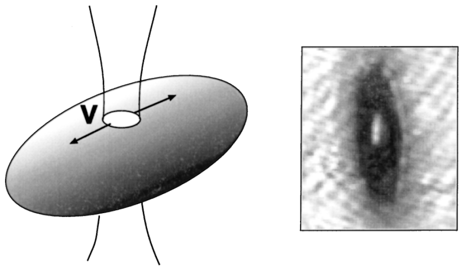

FIGURE 6.1: Stirring a condensate with a blue-detuned laser beam with a width of 13μm, while the radial width of the condensate is 45μm (left). *In situ* image of a condensate with the scanning hole (right). Reproduced from [47].

A graph of the results of this experiment is shown in Fig 6.2.

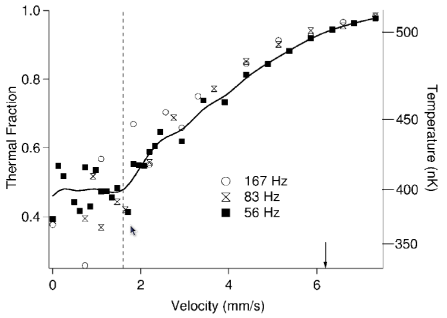

FIGURE 6.2: Evidence for a critical velocity from [47]. Data sets for different sweep velocities of a blue-detuned laser beam in a BEC are plotted as obstacle velocity versus thermal fraction. Two regimes can be observed separated by a dashed line. The low dissipation regime shows little change of thermal fraction or temperature with changed velocity while the high dissipation regime shows a clear increase of thermal fraction with increased velocity. The crossover between the two regions occurs around 1.6mm/s.

The other, more recent work that studied the critical velocity for superfluidity in Bose-Einstein condensates was performed by Engels and Atherton [48]. In their experiment a blue-detuned laser beam of a width larger than the condensate is swept through an elongated cigar shaped BEC thus forcing the atoms to flow through the barrier, which has a height of approximately 24% of the chemical potential of the condensate, as shown in Fig. 6.3. The beam starts moving outside the condensate and is then swept through the BEC at a constant speed. The beam is stopped and the BEC is imaged using absorption imaging after an anti-trapping procedure to allow observed features to be enlarged. The images obtained in this fashion were then analysed in Fourier space where the amount of surface ripples was used to gain the quantity ξ which measures the amount of excitation of the BEC. As a result Engels and Atherton observed an increase in excitations above a sweep velocity of 0.3mm/s, a velocity that is much lower than the speed of sound in their system, which was calculated to be 2.1mm/s. A graph that shows the onset of excitations with increasing sweep velocities is shown in Fig. 6.4. This experiment was done using rubidium atoms.

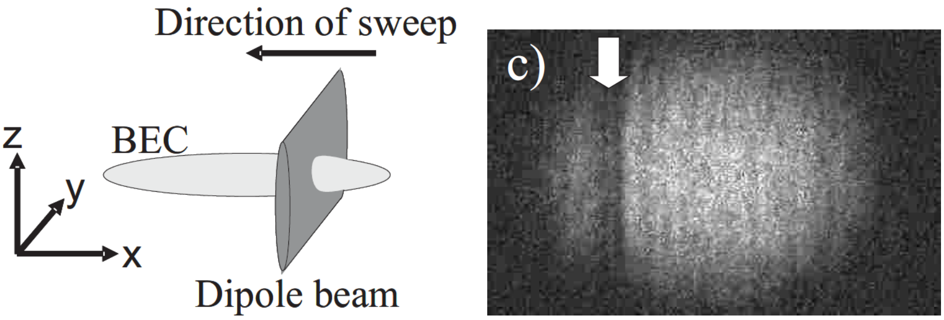

Figure 6.3: Schematic of a blue-detuned beam swept through a cigar shaped condensate (left). Absorption image of condensate with the density depression caused by the initial position of the laser sheet (right). Reproduced from [48].

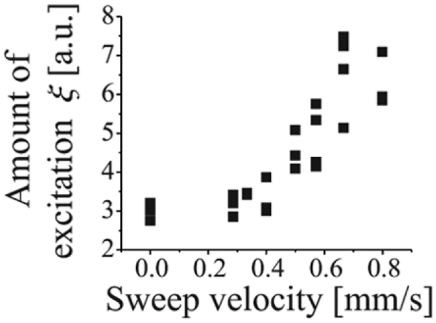

Figure 6.4: Evidence for a critical velocity from [48]. The onset of excitations is shown for varying sweep velocities. First excitations were observed at sweep speeds about 0.3mm/s.

The discrepancy between the onset of a critical velocity and the speed of sound is a remarkable feature of both experiments. According to Landau's criterion the speed of sound c and the critical velocity v_c should be identical linked by

$$v_{\mathrm{c}} = \min\left(\frac{\epsilon(\mathbf{p})}{\mathbf{p}}\right) = \sqrt{\frac{gn}{m}} = c. \tag{6.7}$$

Nevertheless in both experiments performed the critical velocities observed were consistently smaller than those expected from theory, sometimes by more than a factor of seven.

The observed inconsistency between experiment and theory might have two reasons. Firstly, in the Engels experiment, the sweep of the barrier was started outside the BEC. Because of the link of the critical velocity and the density of the Bose-Einstein condensate [see Eqn. (6.7)] the critical velocity tends towards 0 at the edges of the condensate where density tends towards 0. This would lead to the creation of excitations in regions with low density at very low sweep velocities influencing the measurements of a critical velocity. While this would explain some of the discrepancy in the Engels experiment, Raman's experiment should not be affected too much by this as the beam never leaves or enters the condensate. Instead, Raman's experiment suffers from the fact that the obstacle velocity is not constant, adding uncertainty about heating effects due to the acceleration of the barrier.

The second possible reason for the discrepancy between experimentally observed critical velocities and theoretical predictions is that Landau's theory only incorporates phononic excitations. Yet, in the wake of the Raman experiment theoretical predictions have been made that the formation of vortices, regions of zero density in 3D and 2D, and solitons, in 1D, might provide alternative mechanisms for excitations and therefore dissipation. These would not have been observable in the experiment conducted by Raman *et al.* as they only looked at the change in condensate fraction as a measure for dissipation. Engels and Atherton, however, were aware of this fact and subsequently tried to observe soliton formation in their experiment. To do this, they measured the lifetime of dark notches in their absorption images. They observed that the primary depression at the position of the laser beam barrier was filled in within 10ms after switching off the laser light, which is plausible as the initial width is roughly 20μm with a speed of sound of 2.1mm/s. However, the dark notches were still visible after more than 50ms from which Engel and Atherton concluded that these dark notches were indeed solitons.

To circumvent these problems and verify the existence of solitons and/or vortices as the mechanisms of dissipation our proposed experiment will have two advantages. Firstly, it will start the sweep of the obstacle within the BEC in a region where the potential is going to be very flat, guaranteeing minimal density changes over the scanned area. By this it will be made sure that lower densities will not lead to lower phononic excitation speeds. Secondly, we will try to observe the quantized nature of soliton/vortex creation by counting the number of excitations present in the condensate depending on the sweep velocity of the barrier, verifying by comparison with GPE calculations that observed features do correspond to features expected from theory.

6.2.1 Our Experimental Approach

Our experimental approach is as follows. Using the scanning beam trap described in section 4.3.2 a Gaussian beam is scanned horizontally over 25 scan positions to create a line potential with a very flat bottom. This is schematically shown in Fig. 6.5. The smoothness of the trap bottom is ensured by using the feed-forward technique described in the section on the scanning beam trap. A BEC is created in our magnetic trap and then transferred to the line trap. By turning down the power of the scanned beam at one of the scanned positions within the line a barrier is created which has a height of about 1/3 the chemical potential of the condensate in the line. By changing the position of the scanned beam that is reduced in power the barrier is then moved through the condensate at varying speeds. The condensate is imaged using absorption imaging in two directions to search for the signature of solitons and/or vortices looking down the z-direction and to measure temperature and condensate fraction looking down the y-direction. (Both directions are defined by Fig. 4.2.) Some of the results obtained here have also been presented as part of an honours thesis in [91].

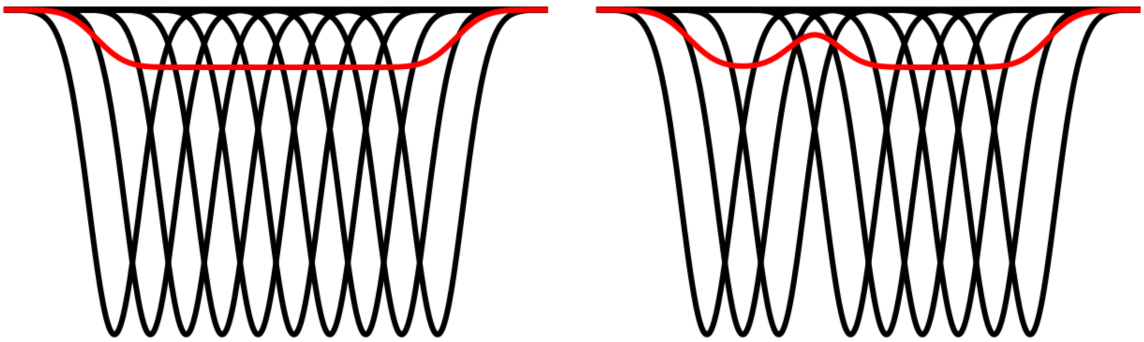

Figure 6.5: Potential created by ten scan positions of a red-detuned Gaussian beam (red) shown with the original Gaussian beams (black). The potential on the left shows a smooth line while the picture on the right shows a barrier that has been introduced by switching off the beam at one of the scan positions.

6.3 Numerical Simulations

To find the right parameter space for the experiment to measure the critical velocity, numerical simulations were run. Unlike the Schrödinger equation, the Gross-Pitaevskii equation is not linear and therefore, due to the nonlinearity, it is not enough to know one parameter, such as the derivative of the wavefunction for example, at a given point in space to determine the stationary state completely. This fact and the fact that analytic solutions are hard to find has led to the development of a number of powerful numerical methods to solve the GPE. In the following I will discuss a split-step Fourier method that has been used to run simple one-dimensional simulations, and some results obtained using these one-dimensional calculations. It was found that the features we are hoping to observe are not found in one-dimensional calculations and therefore it was necessary to do a more complicated analysis of the situation. More accurate two-dimensional modeling based on the well known Runge-Kutta algorithm was performed by fellow PhD student Chao Feng showing solition and vortex formation. A summary of his findings will be presented, giving the parameters for our experiment.

6.3.1 Split-Step FFT Method

The Split-Step FFT method is a numerical method to solve non-linear partial differential equations and is therefore perfectly suited to get numerical solutions to the non-linear Schrödinger equation [92]. Its name arises from the fact that it relies on computing the linear and non-linear parts in small steps for which it is necessary to Fourier transform back and forth between conjugate variables. This is because the kinetic energy part is computed in momentum space while the potential energy part is computed in position space where they are easy to calculate respectively.

The generalized solution to the Gross-Pitaevskii equation in one dimension can be written as

$$\psi(x,t) = \exp\left(-\frac{i\hat{H}(x)t}{\hbar}\right)\psi(x,0), \tag{6.8}$$

where the Hamiltonian operator $\hat{H}$ is made up of a kinetic energy part $\hat{T}$ and a potential energy part $\hat{V}$ such that $\hat{H} = \hat{T} + \hat{V}$. The kinetic energy part in momentum space has the form

$$\hat{T} = \frac{p^2}{2m}, \tag{6.9}$$

where p is the particle momentum and m the mass of the particle. The potential energy part will be written in its position space form which is

$$\hat{V} = V + g|\psi|^2, \tag{6.10}$$

with V the external trapping potential and g an interaction constant that describes atom-atom interactions within the BEC. Time evolution of the system can now be described as

$$\psi(x,t) = \exp\left(-\frac{i(\hat{T}+\hat{V})t}{\hbar}\right)\psi(x,0). \tag{6.11}$$

Because $\hat{T}$ and $\hat{V}$ do not commute the Baker-Hausdorff approximation has to be used which states that for small finite step times $\mathrm{d}t$ the error in treating them as commuting operators scales as $\mathrm{d}t^2$. Therefore, for small time steps the time evolution can be approximated by

$$\psi(x,t+\mathrm{d}t) \approx \exp\left(-\frac{i\hat{T}\mathrm{d}t}{\hbar}\right)\exp\left(-\frac{i\hat{V}\mathrm{d}t}{\hbar}\right)\psi(x,t), \tag{6.12}$$

where better accuracy is achieved if the momentum step is split up in two parts with the first of those momentum half steps being done before the position step and the second one after. With this symmetrized Split-Step FFT method errors on the order of $\mathrm{d}t^3$ rather than $\mathrm{d}t^2$ are achieved. Thus, the full equation can now be written as

$$\psi(x,t+\mathrm{d}t) \approx \exp\left(-\frac{i\hat{T}\mathrm{d}t}{2\hbar}\right)\exp\left(-\frac{i\hat{V}\mathrm{d}t}{\hbar}\right)\exp\left(-\frac{i\hat{T}\mathrm{d}t}{2\hbar}\right)\psi(x,t). \tag{6.13}$$

Since it is easy to calculate $\hat{T}$ in momentum space and easy to calculate $\hat{V}$ in position space the wavefunction ψ will be Fourier transformed back and forth to compute the different parts. The whole process of the split-step FFT method can therefore be written as

$$\psi(x,t+\mathrm{d}t) \approx F^{-1}\left[U_p F\left[U_x F^{-1}\left[U_p F\left[\psi(x,t)\right]\right]\right]\right], \tag{6.14}$$

where F and F^{-1} denote the Fourier transform and its inverse, respectively, and the U_i are the time evolution operators in momentum and position space, which can be written as

$$U_p = \exp\left(-\frac{ip^2\mathrm{d}t}{4m\hbar}\right) \qquad \text{and} \qquad U_x = \exp\left(-\frac{i(V+g|\psi|^2)\mathrm{d}t}{\hbar}\right). \tag{6.15}$$

6.3.2 Results Of One-Dimensional Simulations

As a first step the ground state of the system was found using integration in imaginary time. In this method $\Delta t \rightarrow -i\Delta t$, starting from a more or less random initial wavefunction, in this case the wavefunction given by the Thomas-Fermi approximation, and normalizing after every step. This leads to a fast decay of higher energy states eventually leaving only the lowest-energy state. This can be shown by starting from the Gross-Pitaevskii equation [93]

$$\left[-\frac{\partial^2}{\partial x^2} + V(x) + U_0|\psi|^2\right]\psi = \imath\frac{d\psi}{dt} \tag{6.16}$$

and remembering that any arbitrary trial function $F(x)$ can be written as a complete set of eigenfunctions (although these might be unknown) of the form

$$F(x) = \sum_{i=1}^{\infty} \alpha_i \mathcal{F}_i(x), \tag{6.17}$$

where the $\mathcal{F}_i(x)$ are the eigenfunctions. The time independent GPE then becomes

$$\left[-\frac{\partial^2}{\partial x^2} + V(x) + NU_0|F(x)|^2\right]F(x) = \sum_{i=1}^{\infty} \alpha_i E_i \mathcal{F}_i(x), \tag{6.18}$$

where the E_i are the energy eigenvalues corresponding to the $\mathcal{F}_i(x)$. When the spatial part of this is propagated in imaginary time, the exponential of the time evolution operator is take with a real exponent. This leads to a fast decay of high energy states such that the expansion of the solution is dominated by the eigenfunction of the ground state [93]. Using this method the ground state for an attractive trap created by 25 scan positions of a red-detuned laser beam was found for $N = 50,000$ atoms.

The effect on the ground state of an obstacle created by reducing the power at one of the beam positions has also been investigated. For this, simulations were run for different positions of the obstacle as explained in section 6.2.1 and different values of the dimple depth which can be achieved by reducing the optical power at the desired position of the obstacle. Figure 6.6 shows the ground states for no obstacle and obstacles at positions 5, 9, and 12, where the obstacle is created by completely switching off the beam at the position of the obstacle. It can be seen that for a situation where the obstacle is not sufficiently far inside the condensate the condensate is pushed to the side resulting in a smaller condensate while for situations where the obstacle is sufficiently far inside the BEC the barrier is too high resulting in the condensate being split in two unconnected parts.

Results for varying barrier heights are shown in Fig. 6.7. It can be seen that switching off the beam completely at one of the scanned positions creates a barrier that is splitting the condensate into two unconnected parts. Only upon reducing the power by about 0.5% or less does the condensate stay connected. A change of 0.1% gives a barrier that has a height of about 1/3 the chemical potential of the BEC.

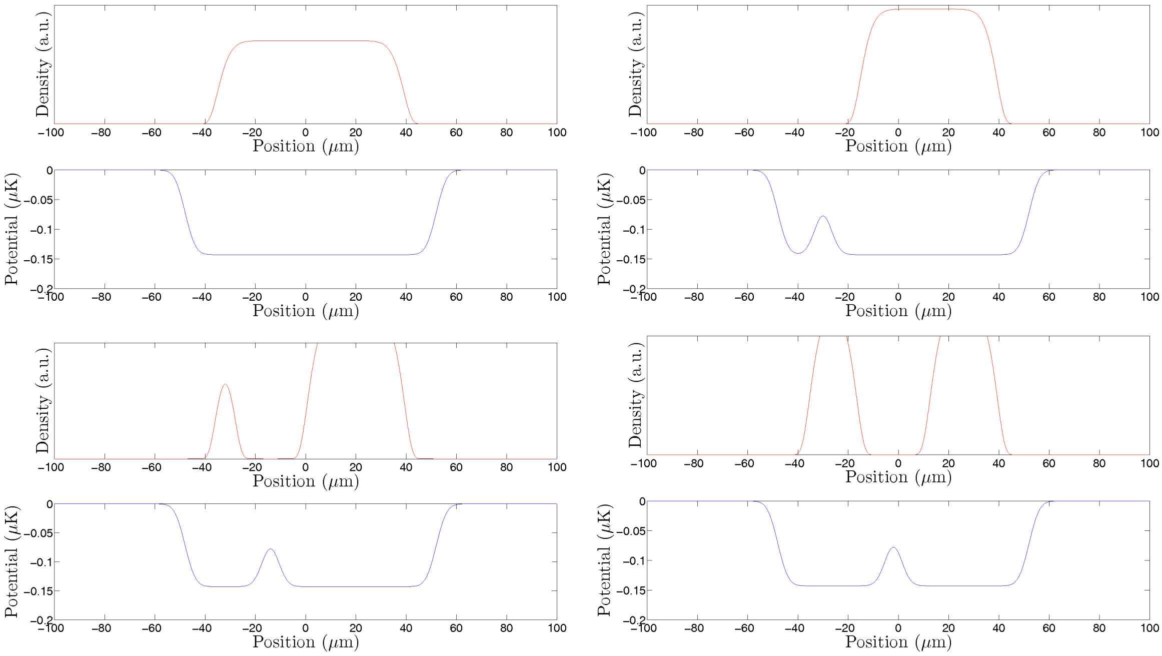

Figure 6.6: Calculated density $n = |\psi|^2$ of atoms for the ground state in a trap created by 25 positions of a red-detuned Gaussian beam (shown in red) with the potential of the trap it is created in (shown in blue) with no barrier (top left), barrier created by switching off the beam at position 5 (top right), position 9 (bottom left) and position 12 (bottom right). Calculations are 1D-GPE simulations.

In the experiment the trap is created by scanning an attractive Gaussian beam along 25 positions while introducing a barrier that is created by reducing the power of the attractive beam at one of the 25 scan positions. Creating the barrier this way causes it to move in a stepwise fashion rather than moving in a continuous way. To check whether this discrete movement would cause any problems by creating additional excitations, simulations were run with the same average speed of the barrier and same barrier heights and starting positions for a barrier moving in discrete steps, and for a barrier moving in a continuous fashion. (It has to be noted though that the continuous way is not actually continuous because of the discrete nature of numerical simulations. However, the step size is reduced by over a factor of 50 compared to the discrete obstacle movement.) Figure 6.8 shows density profiles for a number of different conditions where it was observed for all simulations that there was no significant difference between the two ways of moving the obstacle.

Since it is not possible to evaporate in the optical trap in our setup the actual ground state of the line trap with barrier is not accessible. To conduct the experiment the only way is to transfer a BEC into a line trap without a barrier and then to create the barrier with the BEC already in the line trap. To see if the turn-on of the barrier would cause major disturbances to the BEC, simulations were carried out that show the effects of turning on a barrier in a line with the BEC in the ground state of the trap without barrier, without actually moving the barrier, and then giving the BEC time to evolve in time, checking for excitations. Figure 6.9 shows the density profile of a BEC after a sudden turn-on of barriers

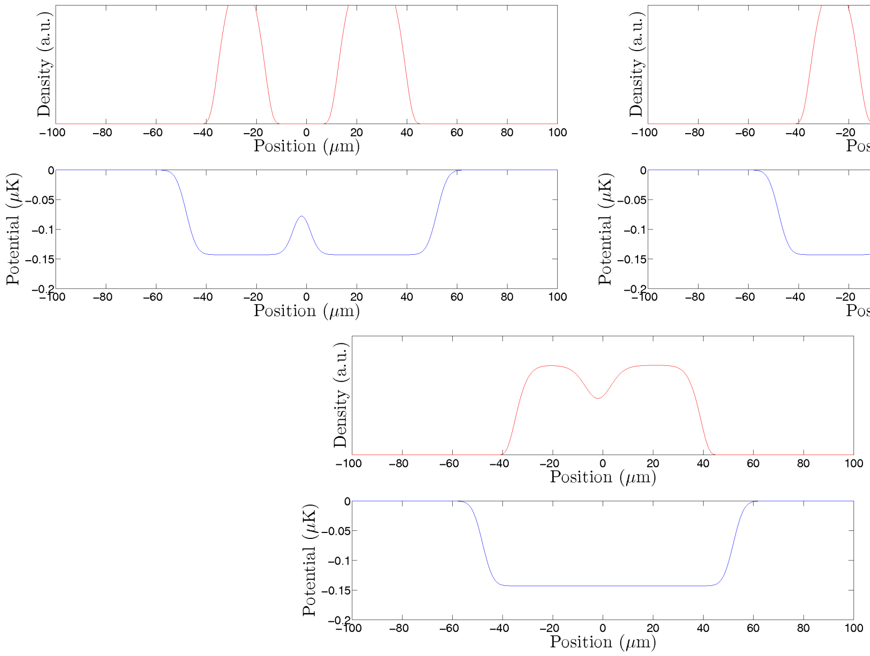

FIGURE 6.7: Calculated density $n = |\psi|^2$ of atoms for the ground state in a trap created by 25 positions of a red-detuned Gaussian beam (shown in red) with the potential of the trap it is created in (shown in blue) with a barrier at position 12 created by reducing the laser power at the obstacle position to 0% (top left), 50% (top right) and 99.9% (bottom) of the initial value. Calculations are 1D-GPE simulations.

of different heights. The time for the free evolution of the BEC was chosen to be the time it would take for a barrier to move through the condensate at a speed of 1mm/s, which is of the order of the expected critical velocity. It was found that for higher barriers the turn on is more violent but that in all cases bow waves are created that travel from the position of the barrier outwards. However, no creation of solitons was observed.

To find the critical velocity, simulations were then run where a BEC starts out in a line trap without a barrier being present. A barrier is then switched on at the ninth position of the scanning trap and moved through the condensate at varying speeds. For a barrier height reduced by $\tau = .001$ times the initial barrier height there is no clear sign of a critical velocity. Figure 6.10 shows calculated density profiles of BECs for various barrier speeds. The snapshot is always taken when the barrier is 1/3 through the condensate. At a velocity of $v = 10$mm/s the condensate seems completely undisturbed, which can be explained by the fact that, even though always travelling at a speed lower than that of the obstacle, the soliton does travel faster for faster obstacle velocities. At the same time the highest speed the soliton can travel at is given by the speed of sound in the system. Since $v = 10$mm/s is faster than the speed of sound it seems to be the case that the soliton created in the wake of the fast moving barrier would have been faster than the speed of sound and therefore no soliton is created. From previous experiments with similar conditions to ours, the critical velocity was expected to be around 1mm/s. Calculating the critical velocity according to Landau's criterion given in Eqn. (6.6) gives an expected value of $v_c = 0.7$mm/s for the one-dimensional

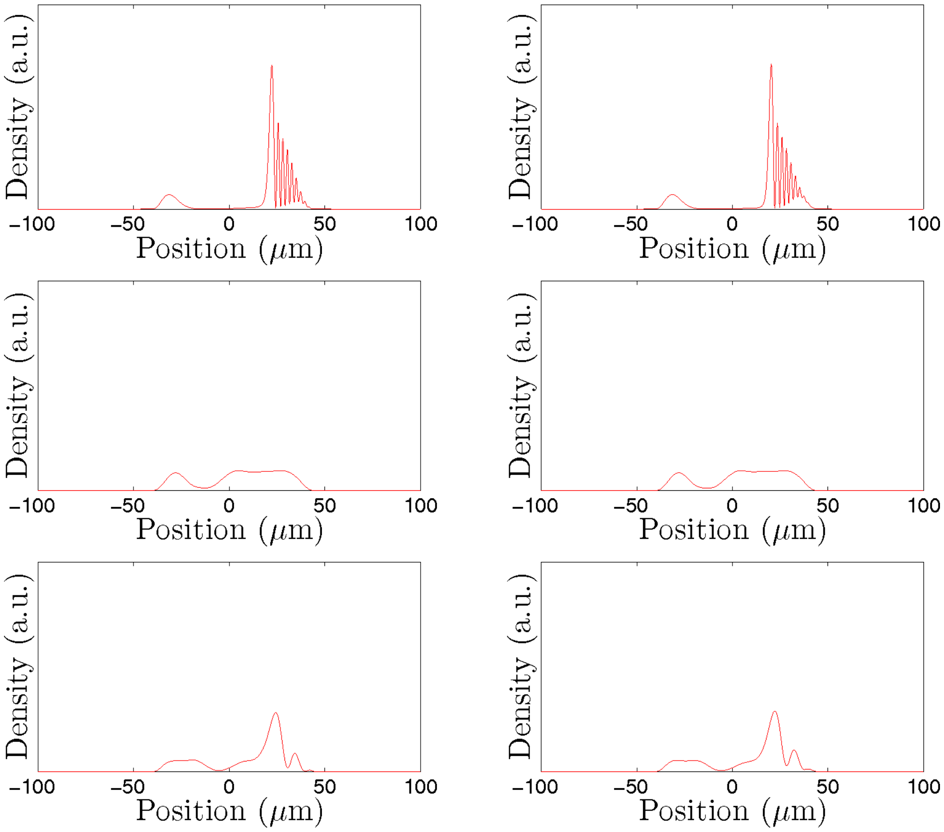

FIGURE 6.8: Calculated density profiles $n = |\psi|^2$ of a BEC after dragging a barrier through the condensate. The barrier was moved in a discrete way (left column) and in a continuous fashion (right column) for different barrier heights. All conditions show the same behaviour regardless of the nature of the obstacle movement. The density profiles were calculated with a barrier height reduced by $\tau = .1$ of the initial height(top row), $\tau = .005$ (centre row) and $\tau = .001$ (bottom row). All calculations were done with a barrier velocity $v = 1$mm/s. Calculations are 1D-GPE simulations.

case. The fact that no soliton formation is observed and that the condensate is always disturbed when a barrier is dragged through, even at the lowest speeds is taken as an indication that one-dimensional simulations of the situation might not be suitable to treat this problem.

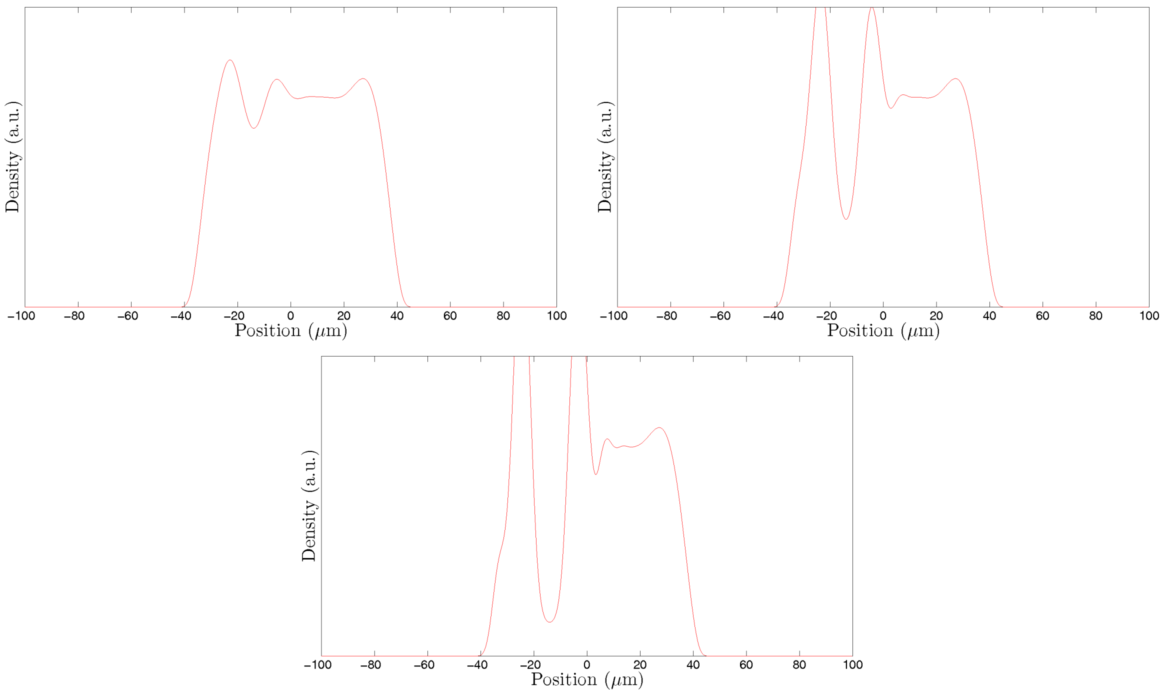

Figure 6.9: Calculated density profiles $n = |\psi|^2$ of a BEC after the sudden turn-on of a barrier where before no barrier was present. The profiles show a decrease in density at the position of the barrier with the depth of the decrease depending on the barrier height with bow waves travelling outward from the position of the obstacle. No formation of solitions is observed. The three graphs shown are for barrier height reductions of $\tau = .001$ times the initial height (top left), $\tau = .005$ (top right) and $\tau = .01$ (bottom). Calculations are 1D-GPE simulations.

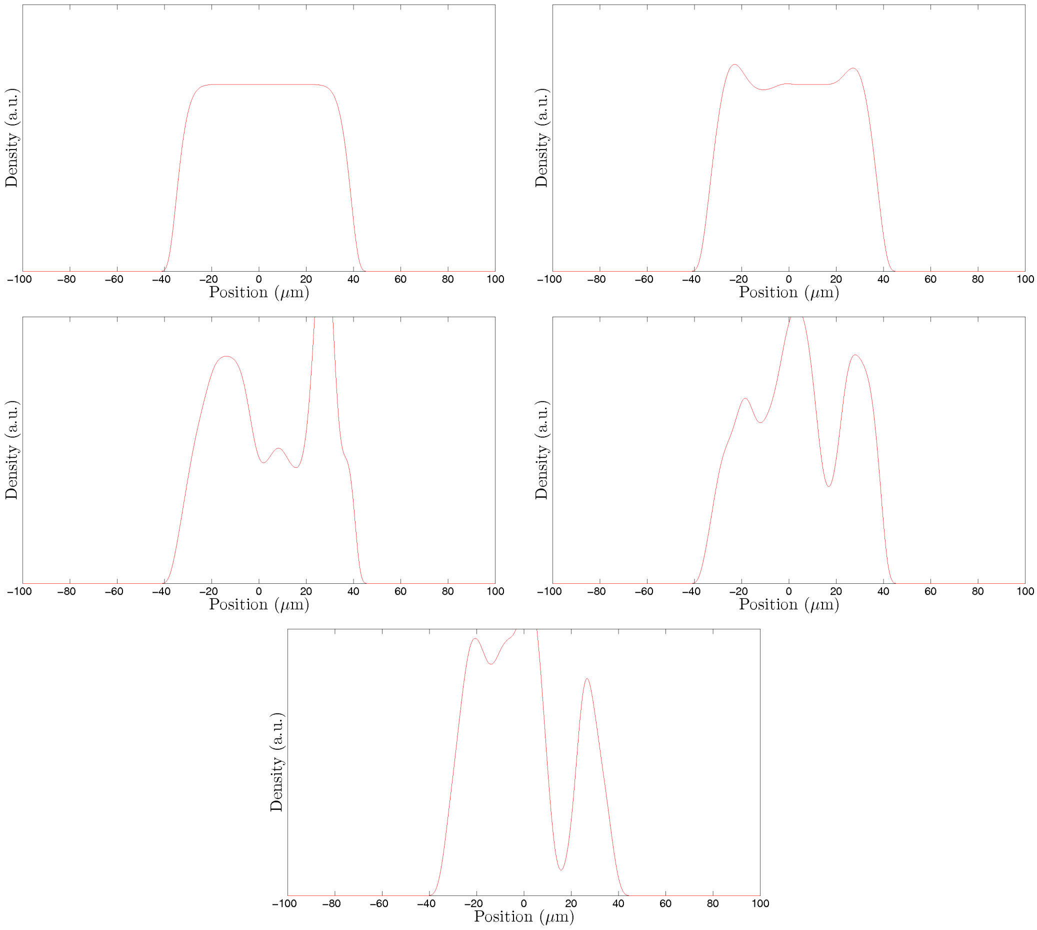

Figure 6.10: Calculated density profiles $n = |\psi|^2$ of a BEC after dragging a barrier through a

6.3.3 Results Of Two-Dimensional Simulations

To support the experimental work two-dimensional numerical simulations have been carried out by Chao Feng [49] to narrow down the possible parameter space and give suggestions on the exact experimental procedure in the scanning beam trap since no soltion and/or vortex creation could be observed in the simpler one-dimensional calculations. In the following section the work of Chao Feng will be summarized, simulation results will be presented and resulting suggestions will be put forward.

The Simulated Equation

The starting point to describe the experiments in the scanning trap is the 3D Gross-Pitaevskii equation (GPE) that can be written as

$$\begin{aligned} i\hbar\frac{\partial\psi}{\partial t} =& -\frac{\hbar^2}{2m}\left(\frac{\partial^2}{\partial x^2}+\frac{\partial^2}{\partial y^2}+\frac{\partial^2}{\partial z^2}\right)\psi \\ &+\sum_{m=1}^{N_{\text{traps}}} V_0 \exp\left[-\frac{2}{\sigma^2}\left((x-m\beta)^2+y^2\right)\right] \\ &+g|\psi|^2\psi-\mu\psi+\frac{1}{2}m\omega_z^2 z^2\psi. \end{aligned} \tag{6.19}$$

The first term describes the kinetic energy and has the usual form. The second term is made up of a series of N_{traps} 2D Gaussian traps that are evenly spaced and overlapping in such a way that they are creating a smooth line potential. The centres of these traps with a width of the beam waist σ are separated by a step size β. The third term describes the interaction between the atoms in a mean-field picture and the fourth is the chemical potential which has to be subtracted to keep the correct normalization which has to follow the normalization condition

$$\int |\psi|^2 \mathrm{d}x = N_{\text{atoms}}. \tag{6.20}$$

The fifth term is the harmonic confinement in the axial direction of the trap. It should be noted that the labelling of the directions in the equations above and for the rest of the section differs from that given in Fig. 4.2. In regards to the definition given before the x- and y-directions have been swapped such that the scanning of the beam is done in the x- rather then y-direction for this section.

To make this equation more tractable for numerical simulations it is converted to dimensionless units and then reduced to two dimensions, assuming that the z-confinement is strong and that excitations along this dimension are frozen out. This assumption is warranted because in the experiments a light sheet will be used to provide sufficient confinement in the z-direction. The transforms used are

$$\zeta_i = \frac{x_i}{x_0}, \qquad x_0 = \sqrt{\frac{\hbar}{m\omega_0}}, \qquad \tau = \omega_0 t, \qquad \bar{\psi} = x_0^{3/2}\psi. \tag{6.21}$$

In this equation $i = x, y, z$. The length is scaled by a harmonic oscillator length which is characterized by the frequency ω_0 which is chosen as convenient. It should be pointed out that ω_0 does not have to be the harmonic oscillator length of the z-confinement. In these new units the atom number is scaled from atoms per meter cubed to atoms per harmonic oscillator length. With all this Eqn. (6.19) can be rewritten as the dimensionless 3D GPE,

$$\begin{aligned} i\frac{\partial\bar{\psi}}{\partial\tau} =& -\frac{1}{2}\left(\frac{\partial^2}{\partial\zeta_x^2} + \frac{\partial^2}{\partial\zeta_y^2} + \frac{\partial^2}{\partial\zeta_z^2}\right)\bar{\psi} \\ & + \sum_{m=1}^{N_{\text{traps}}} \bar{V_0}\exp\left[-\frac{2}{(\sigma/x_0)^2}\left(\left(\zeta_x - \frac{m\beta}{x_0}\right)^2 + \zeta_y^2\right)\right] \\ & + g|\bar{\psi}|^2\bar{\psi} - \bar{\mu}\bar{\psi} + \frac{1}{2}\left(\frac{\omega_z}{\omega_0}\right)^2\zeta_z^2\bar{\psi}. \end{aligned} \tag{6.22}$$

The scaled coefficients are

$$\bar{g} = \frac{g}{\hbar\omega_0 x_0^3}, \qquad \bar{\mu} = \frac{\mu}{\hbar\omega_0}, \qquad \bar{V_0} = \frac{V_0}{\hbar\omega_0}. \tag{6.23}$$

For convenience, we will drop all bars and use x, y, z, t to mean $\zeta_x, \zeta_y, \zeta_z, \tau$ hereforth.

Since a light sheet created by a cylindrical lens will be used in the experiment it can be assumed that the condensate density profile is Gaussian in the tightly trapped z-direction so that the wavefunction can be factorized to $\psi = \phi(x, y)f_z(z)$ where

$$f_z(z) = \left(\frac{1}{\sqrt{2\pi}(\omega_0/\omega_z})\right)^{1/2}\exp\left(-\frac{z^2}{4(\omega_0/\omega_z)^2}\right). \tag{6.24}$$

Since the z-direction is tightly confined it is not possible to excite the condensate in that direction and the equation can be integrated over that direction. Therefore, multiplying Eqn. (6.22) by $f_z^*(z)$, the complex conjugate of $f_z(z)$, and integrating over z gives the dimensionless 2D GPE

$$\begin{aligned} i\frac{\partial\phi}{\partial t} =& -\frac{1}{2}\left(\frac{\partial^2}{\partial x^2}\frac{\partial^2}{\partial y^2}\right)\phi + \frac{1}{8}\left(\frac{\omega_z}{\omega_0}\right)^2\phi + V(x)\phi - \mu\phi \\ & + g\left(\frac{1}{2\sqrt{\pi}(\omega_z/\omega_0)}\right)|\phi|^2\phi + \frac{1}{2}\left(\frac{\omega_0}{\omega_z}\right)^4\phi. \end{aligned} \tag{6.25}$$

To make this equation more clearly laid out all constant terms that multiply ϕ can be grouped into the chemical potential, leading to the reduced, dimensionless 2D GPE

$$i\frac{\partial \phi}{\partial t} = -\frac{1}{2}\left(\frac{\partial^2}{\partial x^2} + \frac{\partial^2}{\partial y^2} + V(x) + \tilde{g}|\phi|^2 - \mu\right)\phi, \tag{6.26}$$

where $\tilde{g} = g(1/2\sqrt{\pi}(\omega_z/\omega_0))$ and the chemical potential has to be determined numerically such that the ground state wavefunction is correctly normalized to preserve the amount of atoms in the BEC. With the characteristic length scale chosen to be equal to the beam width of the scanned beam, $x_0 = \sigma$, this equation is used to simulate the system. This means that $\omega_0 = \hbar/(m\sigma^2)$.

An Initial Set Of Parameters

Eqn. (6.26) is solved using the numerical integration package xmds [94] to investigate the motion of an obstacle through an elongated, homogeneous BEC. The algorithm selected for these particular investigations is a 2D adaptive Runge-Kutta algorithm that also uses Fourier transform propagation steps to numerically integrate this partial differential equation. The system simulated is that of a BEC in a line potential with a barrier moving through the condensate where the barrier is created by switching off or attenuating one of the overlapping Gaussian potentials created by the different scanning positions of the scanning trap. The width of the barrier is therefore limited by the width of the laser beam, while the height of the barrier can be controlled by the amount of change of the potential in the barrier position.

For a first set of calculations the following base parameters were used:

Table 6.1: Initial Parameters for 2D Calculations

Parameter	**Value**
Laser Power	1W
Obstacle Modifier	-0.50
Beam Waist	12μm
Beam Spacing	4μm
Number of Registers	25
Number of Atoms	50,000
Obstacle Start Position	3
Z-Trapping Frequency	300Hz

It should be noted that the obstacle modifier describes how much the laser power is reduced at the position of the barrier in relation to the original potential depth.

With these parameters it was found that the obstacle is too high, resulting in a separation of the BEC into two parts if the obstacle's initial position is sufficiently far inside the BEC (Fig. 6.11) or a smaller condensate where the barrier pushes the atoms out of the way. This configuration means that rather than being a small obstacle around which BEC can flow the barrier acts like a hard wall hitting the fluid. The following figures show the ground state for 50,000 atoms with the obstacle initially at register positions 3, 7, 9 and 12 (Fig. 6.11) and for different obstacle modifiers 0.10 and 0.05 respectively (Fig. 6.12). From these ground state calculations it can be seen that the problem of too high barriers persists for obstacle strengths down to 0.1 (in dimensionless units).

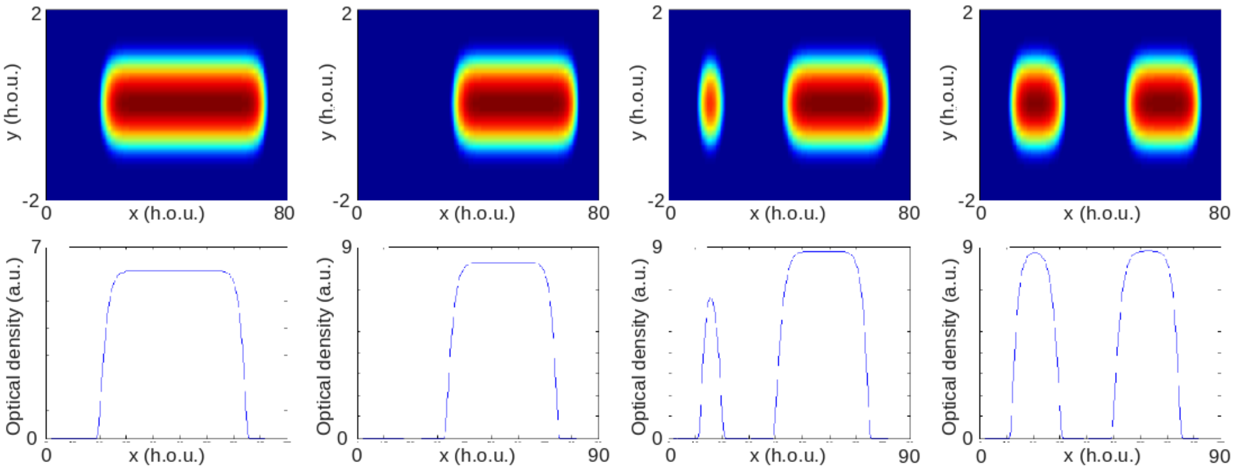

FIGURE 6.11: Calculated density $n = |\psi|^2$ of ground states in a trap created by 25 positions of a red-detuned Gaussian beam with barriers at position 3, 7, 9 and 12 (left to right). The top row shows a 2D plot of the condensate in the trap while the bottom row shows density cross sections. All length scales are in harmonic oscillator units. Calculations are 2D-GPE simulations. Courtesy of Chao Feng.

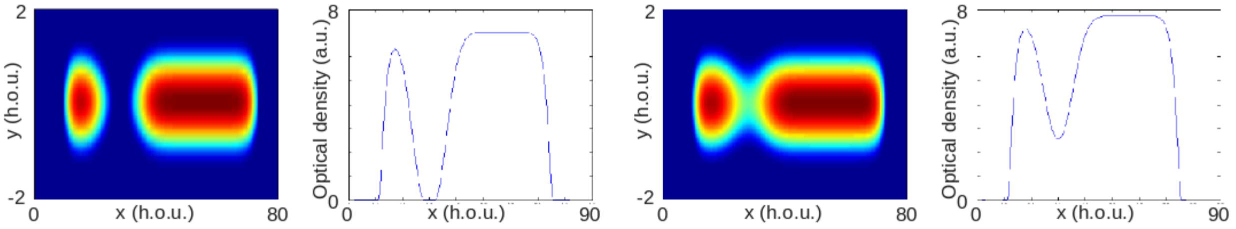

FIGURE 6.12: Calculated density $n = |\psi|^2$ of ground states in a trap created by 25 positions of a red-detuned Gaussian beam with obstacle modifiers of 0.10 (left) and 0.05 (right). Shown are 2D plots of the condensates in the trap and density cross sections. All length scales are in harmonic oscillator units. Calculations are 2D-GPE simulations. Courtesy of Chao Feng.

The ground state calculations shown above lead to following suggestions for the experiment. Firstly, to avoid the problem of the barrier being too high, an obstacle modifier of 0.05 (10 times less) or smaller should be used to avoid disconnection of the two parts of the BEC. Suggested is a modifier of 0.025 (20 times less) which can be achieved by attenuating the trapping beam rather than switching it off completely. Secondly, the obstacle should be placed well within the line so that the condensate to the left and to the right of the barrier are more or less homogeneous. Register 9 out of the possible registers that could be used seems to be sufficiently far into the line to satisfy this condition. All these findings are in agreement with the simple one-dimensional model presented in section 6.3.2.

Effects Of Initial Acceleration

When the obstacle is suddenly accelerated from its original position simulations show the emergence of a compression wave that travels outward from the barrier. This compression wave is an effect that is due to the acceleration only, as a constant velocity below the critical velocity would create no disturbance to the BEC whatsoever, while a constant velocity above the critical velocity would lead to the creation of solitons. The observed compression wave, however, is not of a soliton nature and therefore cannot be attributed to a constant velocity. Nonetheless, the compression wave can lead to the creation of solitons further along in the experimental process if the experiment is not imaged at the right time. When the compression wave bounces off the sides of the potential that forms the line the wave traveling in the direction of the barrier and the wave moving in the opposite direction of the barrier eventually recombine, thereby leading to an asymmetry in the density of the condensate. This asymmetry about the centre of the condensate (one side much denser than the other) seems to encourage soliton/vortex formation. This is an indirect effect of the initial acceleration that is indistinguishable from the solitons created as a result of a barrier velocity above the critical velocity, distorting any signature of a critical velocity. Figure 6.13 shows the density profile of a BEC in a line trap with a barrier moved below the critical velocity. The constant velocity of the barrier that is moved through the condensate does therefore cause no disturbance to the BEC and all observed effects have to be due to the initial acceleration of the barrier. It can be seen that two density depressions are formed due to the initial acceleration of the obstacle. Their paths are indicated by white arrows in the right figure. When the two depressions rebound off the sides of the potential and intersect the formation of solitons can be observed even below the critical velocity which might be indistinguishable from solitons formed due to a critical velocity in an experimental situation where only a final state image would be taken and information about the time evolution is not available.

These effects lead to the following suggestions. Firstly, the experiment should be stopped and the BEC imaged before the compression wave reaches the sides of the trapping potential leading to rebound effects that can distort any signature of a critical velocity. Secondly, the obstacle should be accelerated gradually, to minimize the effect of initial acceleration. Thirdly, if possible, the extent of the condensate in the y-axis should be widened. And fourthly, the critical velocity should be kept small which can be achieved by changing the number of atoms in the condensate.

Minimally Modified Parameters And Values

Running these simulations a minimally modified set of parameters was found that produces reasonable results which allow the observation of the critical velocity in BEC. Rebounding will be present in this situation but the condensate will be imaged before the rebound has

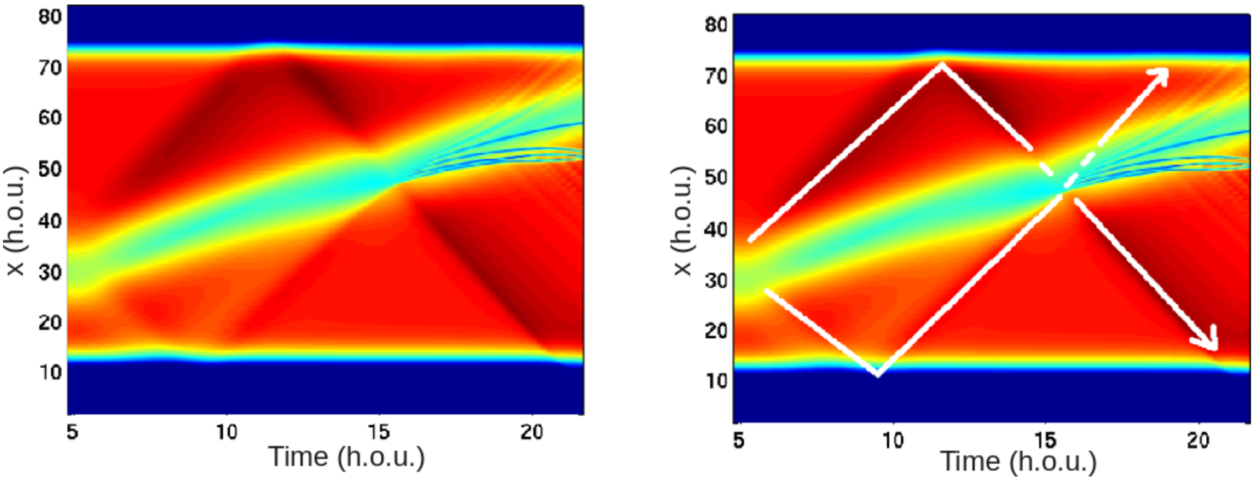

FIGURE 6.13: Rebounding waves creating solitons when intersecting around $t = 15$ even below the critical velocity. The rebound path is shown in the right figure for clarity. Courtesy of Chao Feng.

had a chance to return to the obstacle position and cause additional excitations which are not connected to a critical velocity.

Table 6.2: Parameters for 2D Calculations Which Allow Observation of Critical Velocity

Parameter	**Value**
Laser Power	1W
Obstacle Modifier	**-0.025**
Beam Waist	12μm
Beam Spacing	4μm
Number of Registers	25
Number of Atoms	50,000
Obstacle Start Position	**9**
Z-Trapping Frequency	300Hz

Figure 6.14 shows simulations for different obstacle speeds. In the top row the formation of solitons only after intersection of the rebounds can be seen which is taken as a sign that the obstacle velocity is smaller than the critical velocity of the system. In the middle and the bottom row the formation of one or more solitions is observed even before the rebound intersection occurs. The critical velocity for the creation of one soliton is $v_c = 1.28 \pm 0.07$ mm/s where the error is estimated from numerical solutions. In this case the critical velocity was defined as the first sign of a persistent excitation that could be observed before the bounce back occurs.

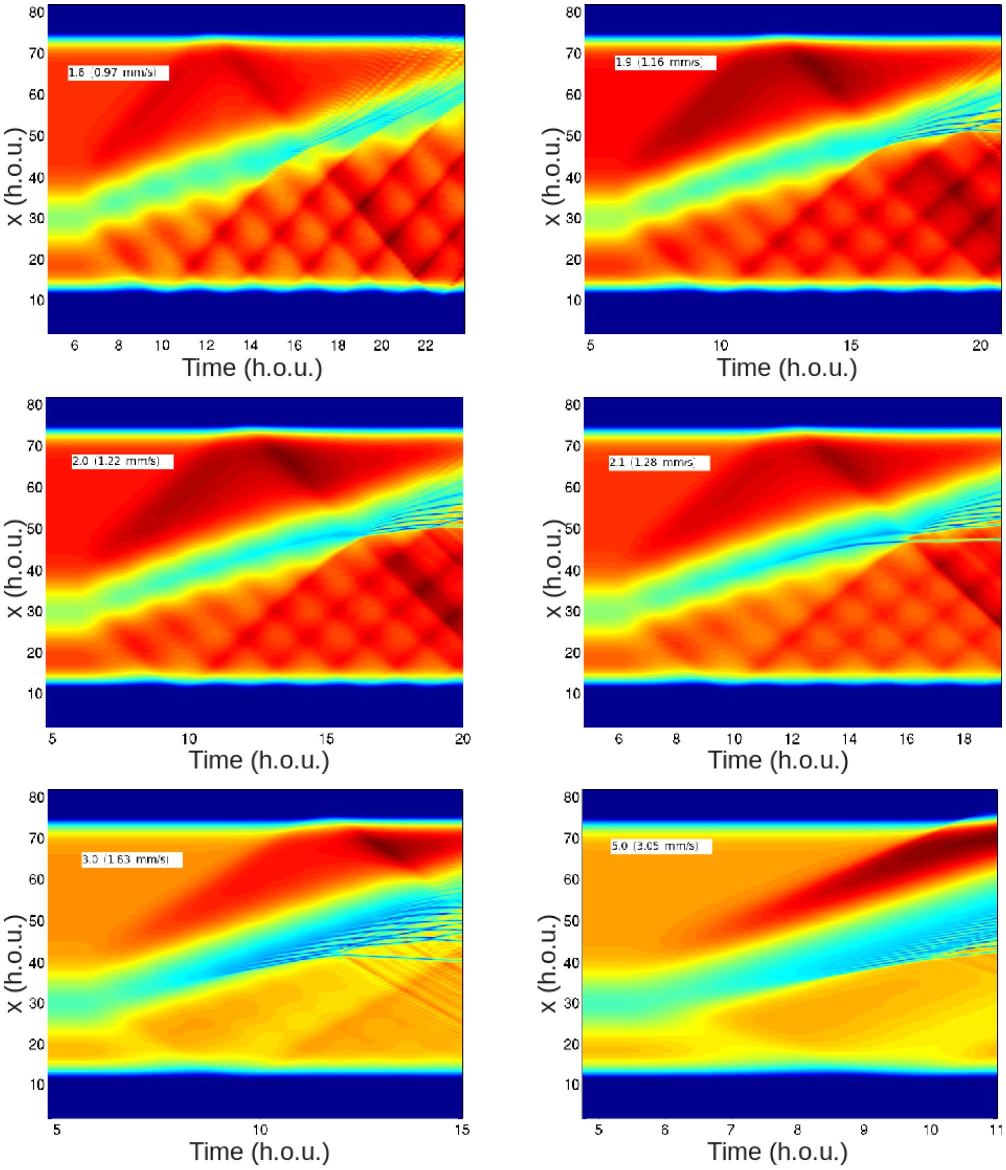

FIGURE 6.14: Time evolution of the average density $n = |\psi|^2$ of a BEC in a line trap with an obstacle moved through the condensate. - Top row: below critical velocity, $v = 0.97$mm/s, $v = 1.16$mm/s. Middle row: above critical velocity, $v = 1.22$mm/s, $v = 1.28$mm/s. Bottom row: much above critical velocity, $v = 1.83$mm/s, $v = 3.05$mm/s. Courtesy of Chao Feng.

To confirm that what is observed is in fact the critical velocity, energy transfer versus obstacle velocity has been calculated where the onset of an energy transfer is taken to be the critical velocity. A minimum was observed for an obstacle velocity of about 1.28mm/s. The position of this minimum is in agreement with the first observation of persistent excitations (see Fig. 6.15). However, instead of a minimum in energy transfer the onset of energy transfer should be observed at this point, meaning that the fact that there is a rise in energy transfer at low velocities needs further investigation. This was attributed to the nature of the numerical algorithm but requires further research.

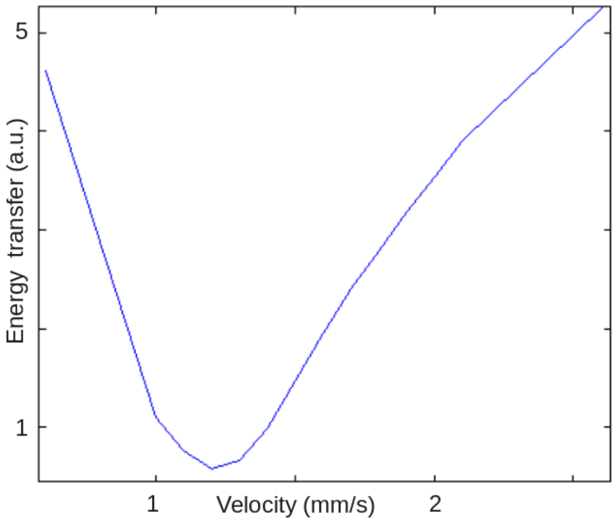

FIGURE 6.15: Energy transfer versus obstacle velocity plot showing an energy transfer minimum around $v_c = 1.28$mm/s. Courtesy of Chao Feng.

It is interesting to note that the mean speed of sound in the system is 19.1mm/s, which is a factor of 14 larger than the critical velocity observed indicating that Landau's picture which only takes phononic excitations into account is not complete. Solitons and vortices can be identified as pathways to energy dissipation below what is predicted by Landau's theory. Figure 6.16 shows a timeline of the creation of solitons above the critical velocity.

6.4 Experimental - Atoms In A Scanning Potential

Since using the scanning beam trap to measure the critical velocity of superfluidity in Bose-Einstein condensates potentially has many advantages over the experiments conducted so far (which have been summarized in section 6.2) we have been working towards the measurement of the critical velocity. These advantages include a very homogeneous potential which in turn leads to a uniform speed of sound in the experiment (since the speed of sound and the condensate density are linked) and a constant speed of the obstacle that is dragged through the condensate. The proposed experiment in the scanning beam trap also very closely mimics the experiments done in liquid helium which first showed the existence of a critical velocity in superfluids allowing comparisons between the two systems Bose-Einstein condensates and liquid helium. In the following the experimental progress towards measuring the critical velocity will be presented.

The proposed experiment itself consists of a homogeneous line potential that is created by spatially scanning a far red-detuned laser beam and loading it with a Bose-Einstein condensate created on an atomchip. A barrier is then introduced into the line by reducing the power of the laser beam at one of the scan positions (as shown in Fig. 6.5) and dragged through the BEC with varying speeds. After a time-of-flight absorption images are taken looking for solitons/vortices and measuring the condensate fraction and temperature.

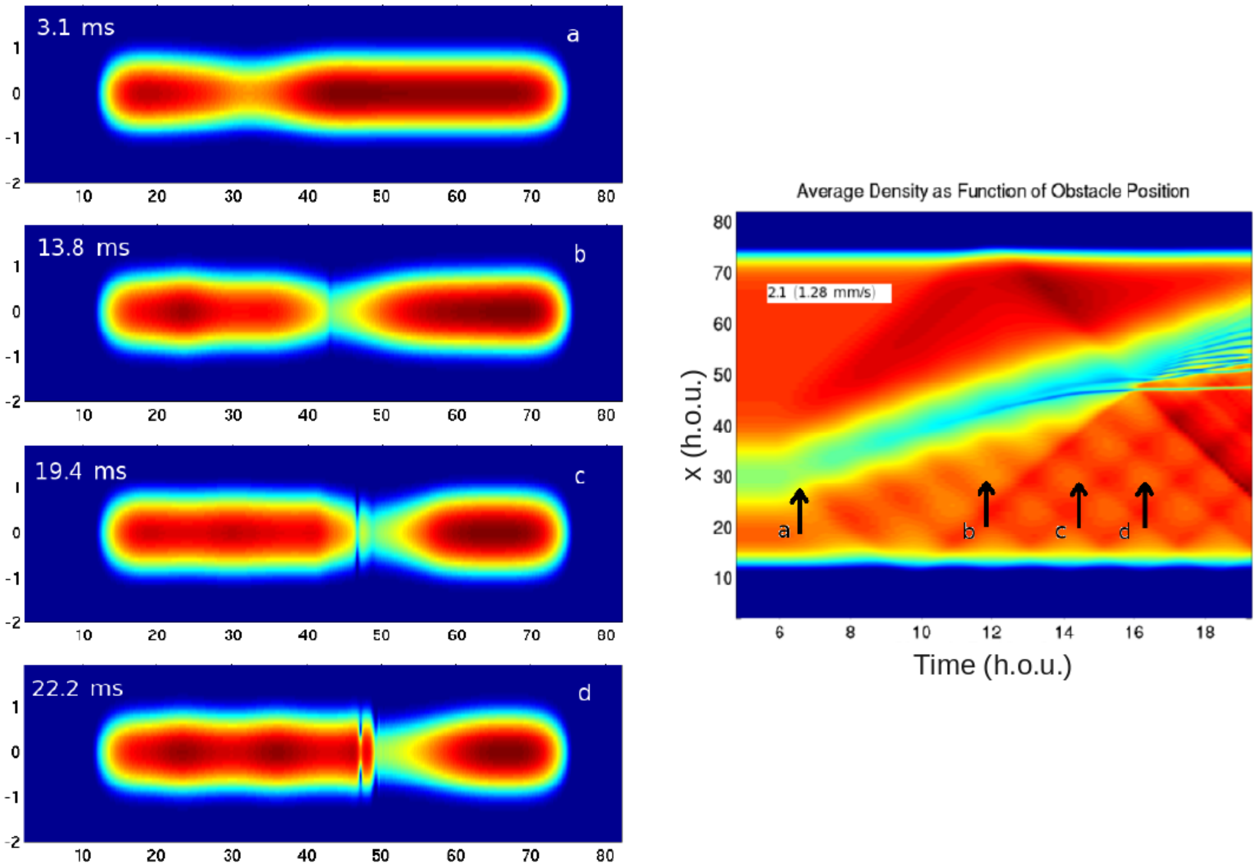

Figure 6.16: Condensate profiles at various times (3.1, 13.8, 19.4 and 22.2ms after first obstacle movement) and average density evolution over time shown for a barrier moving with a speed above the critical velocity. The creation of a solition around 13.8ms can be observed before more solitons are seeded by the intersection of the bouncing back waves. Courtesy of Chao Feng.

When trying to load a line potential with a BEC created on the atomchip, the first step is to align the scanned beam with the magnetic trap. To do this a new imaging direction was used, which is also necessary to observe the resulting potential landscape and atom distribution created by it. The new imaging direction looks down the z-direction as defined in Fig. 4.2, along the direction of the MOT beams that are not reflected off the chip when creating the surface MOT. This means that a motorized flip mirror had to be used such as not to block the MOT beams during the MOT phase. It also means that the imaging beam will follow the way of one of the counterpropagating MOT beams which does not constitute a problem since the MOT beams are switched off during imaging. A further problem that arose was that the trapping beam, with up to 1W of light with $\lambda = 1064$nm, would also be aiming straight at the camera when turned on. That problem was solved by putting an edge filter in front of the camera that blocked the longer 1064nm wavelength while being transparent for the 780nm imaging light. The camera used (ProSilica) has a pixel size of 3.2μm and the imaging optics were chosen to give a resolution of approximately 6μm. A schematic drawing of the imaging setup is shown in Fig. 6.17.

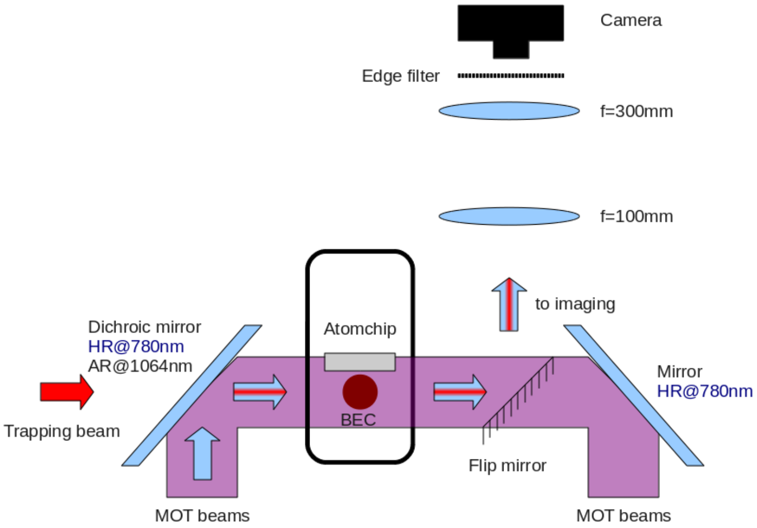

FIGURE 6.17: The new imaging direction set up to take images of the scanned beam and resulting atom distributions. The resonant imaging beam (light blue arrows) follows the beam path of one of the MOT beams. For imaging a motorized flip mirror is flipped into the path of the other MOT beam during imaging. The 1064nm trapping light (red arrows) is blocked from entering the camera by an edge filter transparent for the resonant imaging light.

To align the magnetic trap and the dipole trap an in-trap image of magnetic trap was taken and the trapping beam imaged on the camera afterwards with very low power. Overlapping the beam position on the camera with the position of the image of the magnetic trap resulted in trapping of atoms. The atom number and lifetime in the dipole trap was optimized by carefully tweaking the trapping beam position. A lifetime measurement of the dipole trap is shown in Fig. 6.18. It can be seen that in the first 100ms after transfer the number of atoms in the trap decays quickly. This was found to be due to atoms sloshing in the dipole trap after transfer. Even with careful alignment this could not be avoided due to a slight mode mismatch between magnetic trap and dipole trap. After that the atom number decays very slowly. A fit to the data ignoring the first data points gives a $1/e$ lifetime in the crossed dipole trap (light sheet is turned on for tighter trapping in the z-direction) of 2.1s which is sufficiently long for measurements of the critical velocity.

After transferring the atoms from the magnetic trap to a crossed dipole trap the trapping beam with the BEC in it is scanned horizontally. Even after using the feed-forward technique described in section 4.3.2 was performed and the beam imaged on the camera showed an even light distribution no extension of the BEC width was observed. It was found that this was due to a tilt in the scanned beam which made the atoms "roll down" the line to the lower end of the line potential. Using the vertical scanning ability of the scanning beam trap it was ensured that the scanning of the line was made perpendicular to the direction of gravity by choosing the amplitude of the scan in vertical direction accordingly. It was found that a correction of 0.2MHz scanning width was necessary in the vertical direction which corresponds to a tilt in the scanning of 2.9°. Calculating the potential gradient due to

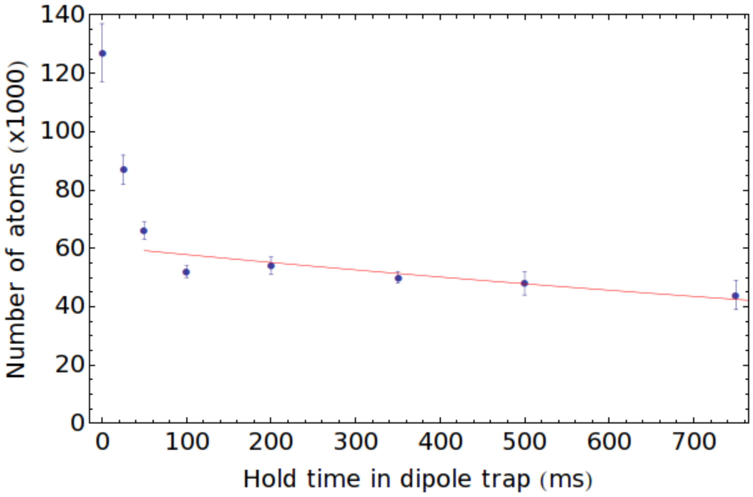

FIGURE 6.18: Lifetime measurement in the crossed dipole trap. After initially losing atoms due to sloshing in the trap the number of atoms decays slowly with a $1/e$ lifetime of 2.1s. Measurements are three shot averages with statistical errors indicated. The red line shows the exponential decay fit ignoring the first data points.

gravity over a length of the condensate of 100μm gives 61nK, which is six times larger than the chemical potential calculated for the BEC in the trap. It was found that the minimum gradient over the length of the trap BEC will visibly respond to is of the size of the chemical potential. This means that tilt has to be kept below 0.5° to have little to no effect on the experiments [91].

Even after correcting for the tilt no line distribution could be observed. It was found that a homogeneous light distribution on the camera was not necessarily good enough due to not enough sensitivity of the camera. It was found that the feed-forward system is able to correct the homogeneity of the line to within 200nK based on the light distribution on the camera which is about 20 times the calculated chemical potential of the Bose-Einstein condensate. To overcome this obstacle the density distribution of the atoms which follows the trapping potential was used to map the potential. With those corrections a line potential with a homogeneous distribution could be observed. An image of the line and a cross section with a flat area over 80μm is shown in Fig. 6.19. Over the homogeneous region fluctuations are of the order of 3% which amounts to the noise in the imaging system also visible in the flanks of the cross section.

To prove that the BEC survives the transfer from the magnetic trap to the dipole trap an image was taken in the "old" imaging direction which is shown in Fig. 6.20. A condensate fraction of 15% is measured. Since the initial condensate fraction in the magnetic trap was of the order of 35% the transfer process has to be improved. To do this we suggest a different loading mechanism for the dipole trap. Instead of loading a static single beam trap which will then start the scanning process we suggest to load the scanned trap directly from the magnetic trap. It is hoped that by doing this the spatial modes of the magnetic trap and

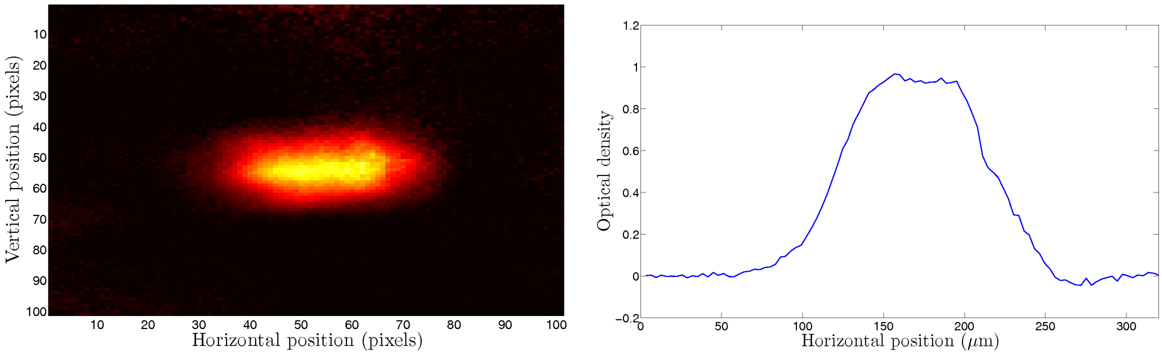

Figure 6.19: Image and cross section of atoms in a line potential. The flat area is about 80μm in width. Fluctuations are about 3% of the density in the homogeneous region.

dipole trap will be better matched, similar to matching laser light when coupling into wave guides or cavities, and thus create less heating. It might also reduce the losses from the atom cloud sloshing in the dipole trap.

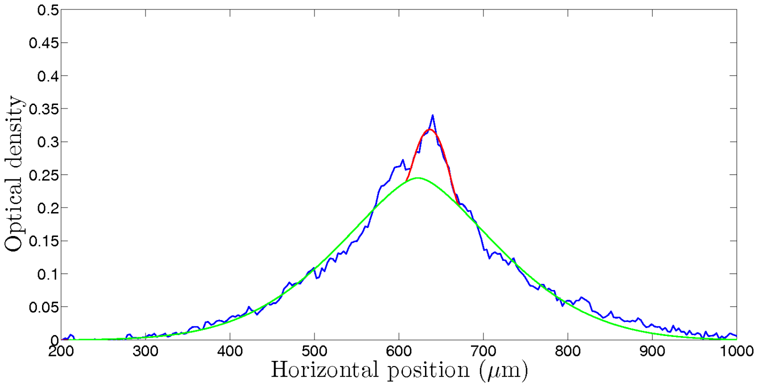

Figure 6.20: Image of the line trap shown in Fig. 6.19 showing a BEC with a condensate fraction of about 15% where the imaging direction is along the length of the line. The green curve shows a Gaussian fit to the thermal background atoms, the red curve an inverse parabola fit to the condensed atoms and the blue line the datapoints.

Another problem that was identified is that the corrections to the beam necessary to create a homogeneous light field are not yet stable enough. In Fig. 6.21 three images taken directly after Fig. 6.19 are shown. It can be seen that the line first becomes less homogeneous and then starts moving to the side of the line. The cause of this instability is not yet known but could be connected to the scanning AOM crystals heating up over time and changing their diffraction efficiencies. The heating of the AOM crystals could be due to the optical power absorbed from the 1W trapping beam and the rf-power that drives the AOMs.

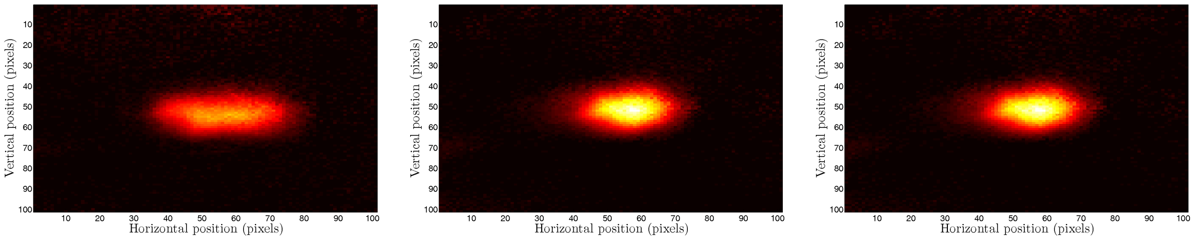

Figure 6.21: Images of atoms in a line potential taken directly after the image shown in Fig. 6.19. The first image has been taken 3 minutes after the one showing the homogeneous line and all further images 3 minutes after the previous one. It can be seen that the correction on the light distribution is not yet stable enough leading to a less and less homogeneous line.

6.5 Outlook

In order to proceed to measure the critical velocity of superfluidity in BEC, the following steps and improvements will be necessary. First, the loading scheme of the line trap will have to be improved to increase the number of BEC atoms in the line trap as well as to reduce heating during the transfer which currently reduces the condensate fraction by over 50%. The number of atoms could potentially be brought close to $150,000$ atoms, the number of atoms in the BEC before transfer to the line trap, which would increase the contrast after time-of-flight imaging to bring out observable features more clearly and an increase in condensate fraction would reduce effects of the thermal cloud on the measurements of the critical velocity. It is suggested to load the trap from the magnetic trap already scanning rather than loading a static dipole trap. This will provide better matching of the spatial modes and thus hopefully reduce atom loss and heating. Secondly, the source of the instability of the light distribution will have to be identified. One probable source is heating of the two-dimensional AOM used for scanning resulting in a change of diffraction efficiencies over time, due to the absorption of optical power from the trapping beam and the rf-power that is driving the AOM. This can be partially solved by leaving the trapping beam and rf on in-between experimental runs to achieve thermal equilibrium of the AOM crystal. With those changes it will be possible to conduct the experiments to measure the critical velocity of superfluidity in BEC.

While first experimental results have been achieved, demonstrating a homogeneous distribution of BEC in a line potential, the theoretical investigations have been ongoing. In those recent calculations it was found that the width of solitons in the system after no free expansion time is of the order of only 0.5μm and even after a free expansion time of 15ms those features would only expand to a size of about 5μm. Even if we are to use the full time of flight available in the system, which is of the order of 25ms or even less the maximum feature size that can be obtained is of the order of 8μm which is on the verge of the resolution of our imaging system which is 6μm. Simulations of various free expansion times are shown in Fig. 6.22.

The small size of the solitons even after free expansion time means that very likely solitons will not be able to be observed with the current imaging system or if they can be observed

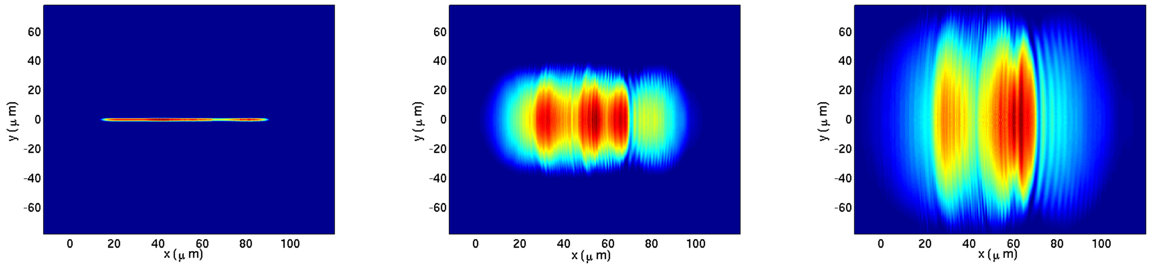

FIGURE 6.22: Size of the condensate with created solitons after free expansion. Shown are calculations for a time-of-flight of 0ms (left), 5ms (center) and 10ms (right). The respective feature sizes are about 0.5μm, 2μm and 3.5μm. Calculations are 2D-GPE simulations. Images courtesy of Chao Feng.

only with very low contrast. To be able to observe solitons with high contrast either of two approaches is therefore suggested. Either the imaging system could be re-designed to give a resolution sufficient to observe the solitons after a time of flight of no more than 20ms, or an anti-trapping technique where atoms are pumped into an anti-trapped state, such as the state $F = 2$, $m_F = 1$ for example, could be used. The anti-trapping process would speed up the expansion of the atom cloud and therefore increase the size of observable features allowing their observation with the current imaging system. Such an approach was used by Engels and Atherton for example [48]. Pumping the atoms into an anti-trapped state could be done with the rf-antenna used for evaporation that is already built into the setup but exact parameters for the population transfer would have to be found.

The candidate ran out of time to actually implement these changes. The key challenges for future experimenters would be to first try the anti-trapping technique mentioned to improve the feature size without having to change the imaging optics which would be more work than determining parameters for the population transfer. Also the AOM heating would have to be checked and it would have to be found out if that was in fact what caused the instabilities in the line homogeneity. These, as well as trying to load the trap already scanning instead of stationary to improve the BEC numbers, are relatively straight forward improvements that could be implemented within a short time frame. If these actually solve the problems that were encountered then a future researcher could obtain results - everything going well - within further six months of experiments.

7

Conclusion

In conclusion, this thesis has shown outcomes on the generation of non-harmonic optical potentials for Bose-Einstein condensates as well as on the physics of Bose-Einstein condensates in non-harmonic optical potentials. The outcomes are as follows.

The Scanning Beam Trap (Chapter 4)

One outcome was the development of a new tool for ultra-cold atom physics which allows the creation of nearly arbitrary two-dimensional potential landscapes. Using a two-dimensional acousto-optic modulator a far red-detuned and therefore attractive laser beam is spatially scanned with a scanning frequency of order of tens of KHz, fast compared to the trapping frequencies in the system, to create time-averaged potentials. Using a feed-forward technique it has been shown that the bottom of such a trap can be made flat enough for use in ultra-cold atom physics allowing a wide range of potential landscapes, in particular the creation of ring traps which are desirable to create persistent currents and investigate superfluidity in a multiply connected geometry. The fact that the scanning beam trap allows the creation of static as well as dynamic potentials has been used to create a line potential with a moving barrier used for experiments on superfluidity in Bose-Einstein condensates. The feasibility of such a trap could be shown through proof of principle measurements and progress towards the measurement of a critical velocity of superfluidity in Bose-Einstein condensates using the scanning beam trap have been presented. For the future, experiments to create vortices in a deterministic fashion as well as experiments on quantum computation with Rydberg atoms have been proposed making use of the new trap design. We are convinced that through its versatility more proposals and experiments using the scanning beam trap will be seen in future.

Condensation Dynamics In A Dimple Trap (Chapter 5, Part 1)

Another outcome presented is the measurement of equilibrium thermodynamic properties and condensation dynamics in Bose-Einstein condensation shedding light on the question on how condensates form out of a thermal cloud which is inherently incoherent. For this, measurements have been presented where a narrow optical dimple potential is superimposed upon a much wider magnetic trap and the condensate fraction and temperature are measured as a function of dimple depth and equilibration time in the dimple trap, for both wide and narrow dimples. The measurements have been compared to theoretical results, in particular quantum kinetic theory, and showed good agreement with the data taken. This means that for the first time a quantitative study has been presented that correctly predicts the growth of a condensate out of a thermal cloud when crossing the Bose-Einstein transition at constant temperature.

Rethermalization Dynamics Of A BEC (Chapter 5, Part 2)

Furthermore, measurements on the rethermalization dynamics of a Bose-Einstein condensate have been reported. In those measurements an optical dimple potential is switched off suddenly and the condensate is given time to rethermalize in a much wider magnetic trap. Measurements have been taken for two different dimple depths. It was found that a sudden breakdown in condensate fraction occurs with a subsequent recovery and equilibration at a different level. Since quantum kinetic theory cannot be applied to the situation there is currently no theory to compare the experiments to. However, the outcome was checked for plausibility using a theory developed by Castin and Dum to predict the size of Bose-Einstein condensates in time-dependent potentials. It was found that the results were inconclusive. Expected behaviour that was not observed includes form oscillations of the Bose-Einstein condensate. One possible reason for this is that the condensate fraction might have been too low allowing for a large influence by the present thermal fraction which is not considered in Castin and Dum's theory. It is suggested that for future research those measurements could be repeated at lower temperatures and consequently with higher condensate fractions to reduce the influence of thermal atoms. Unfortunately this is not possible using the current apparatus at the University of Queensland. It would also be good to see theoretical efforts in that area to develop a theory that is able to include the effects of thermal background atoms to compare to the existing measurements.

Critical Velocity Of Superfluidity In BEC (Chapter 6)

In the last chapter theoretical results and experimental progress towards the measurement of a critical velocity of superfluidity in Bose-Einstein condensates have been presented. Since previous measurements showed a disagreement between experimental results and the predictions of Landau's theory of superfluidity (which predicts that the critical velocity should be equal to the speed of sound in the system), this area is still of considerable interest today. It is particularly important, since superfluidity provided the link to Bose-Einstein condensation in liquid helium, where superfluidity was first observed. Calculations show that Landau's picture is incomplete and that soliton and vortex formation provide a mechanism for energy dissipation leading to a break down of superfluidity at energies lower than those predicted by Landau. The scanning beam trap developed as part of this project has been used to create a line trap with a movable barrier. A smooth line shaped Bose-Einstein condensate has been shown with a homogeneous region of 80μm length and a condensate fraction of about 15%. For the future there are still some experimental obstacles to overcome in the quest to measure the critical velocity in that setup. These include a loading mechanism that increases the number of atoms in the line trap and reduces heating when the atoms are transferred over from the magnetic trap in which the Bose-Einstein condensate is initially created. It is suggested to load an already scanning trap, as opposed to a static trap as done here, to improve the mode matching between magnetic trap and optical trap. Also the source of instabilities in the feed-forward mechanism employed to create the homogeneous potential have to be identified. One possible source is heating of the AOM crystals used to scan the beam which could be overcome by turning the trapping beam on in-between experimental runs to see if the crystals reach a thermal equilibrium. Recent calculations also show that the solitons we hope to observe are too small for detection in the current setup of the experiment. A new imaging system with a higher resolution or an anti-trapping technique to increase the size of observable features are possible solutions.

References

[1] M. Anderson, J. Ensher, M. Matthews, C. Wieman, and E. Cornell. *Observation of Bose-Einstein condensation in a dilute atomic vapor.* Science **269**, 198 (1995).

[2] K. Davis, M.-O. Mewes, M. Andrews, N. van Druten, D. Durfee, D. Kurn, and W. Ketterle. *Bose-Einstein condensation in a gas of sodium atoms.* Phys. Rev. Lett. **75**, 3969 (1995).

[3] A. Einstein. *Quantentheorie des einatomigen idealen Gases: Zweite Abhandlung.* Sitzungsber. Preuss. Akad. Wiss. p. 3 (1925).

[4] L. de Broglie. *Radiation waves and quanta.* Comptes rendus p. 507 (1923).

[5] S. N. Bose. *Plancks Gesetz und Lichtquantenhypothese.* Z. Phys. **26**, 178 (1924).

[6] F. London. *The λ-phenomenon of liquid helium and Bose-Einstein degeneracy.* Nature **141**, 643 (1938).

[7] J. Bardeen, L. Cooper, and J. Schrieffer. *Theory of superconductivity.* Phys. Rev. **105**, 1175 (1957).

[8] L. Chase and N. Peyghambarian. *Evidence for for Bose-Einstein condensation of biexcitons in CuCl.* Phys. Rev. Lett. **42**, 1231 (1979).

[9] N. Peyghambarian and L. Chase. *Bose-Einstein statistical properties and condensation of excitonic molecules in CuCl.* Phys. Rev. B **27**, 2325 (1983).

[10] J. F. Allen and A. D. Misener. *Flow of Liquid Helium II.* Nature **141**, 75 (1938).

[11] P. Kapitza. *Viscosity of liquid helium below the λ-point.* Nature **141**, 74 (1938).

[12] J. D. Reppy and D. Depatie. *Persistent currents in superfluid helium.* Phys. Rev. Lett. **12**, 187 (1964).

[13] C. A. M. Castelijns, K. F. Coates, A. M. Guenault, S. G. Mussett, and G. R. Pickett. *Landau critical velocity for a macroscopic object moving in superfluid 3He-B: Evidence for gap supression at moving surfaces.* Phys. Rev. Lett. **99**, 160405 (2007).

[14] J. Bogoliubov. *On the theory of superfluidity.* J. Phys. **XI**, 23 (1947).

[15] O. Penrose and L. Onsager. *Bose-Einstein condensation in liquid helium.* Phys. Rev. **104**, 576 (1956).

[16] K. Huang and C. Yang. *Quantum-mechanical many-body problem with hard-sphere interaction.* Phys. Rev. **105**, 767 (1957).

[17] T. Lee, K. Huang, and C. Yang. *Eigenvalues and eigenfunctions of a Bose system of hard spheres and its low-temperature properties.* Phys. Rev. **106**, 1135 (1957).

[18] K. Huang, C. Yang, and J. Luttinger. *Imperfect Bose gas with hard-sphere interaction.* Phys. Rev. **105**, 776 (1957).

[19] T. Lee, K. Huang, and C. Yang. *Low-temperature behavior of a dilute Bose system of hard spheres. I. Equilibrium properties.* Phys. Rev. **112**, 1419 (1958).

[20] T. Lee, K. Huang, and C. Yang. *Low-temperature behavior of a dilute Bose system of hard spheres. II. Nonequilibrium properties.* Phys. Rev. **113**, 1406 (1959).

[21] T. Lee, K. Huang, and C. Yang. *Bose-Einstein condensation of lithium: Observation of limited condensate number.* Phys. Rev. Lett. **78**, 985 (1997).

[22] C. J. Pethick and H. Smith. *Bose-Einstein Condensation in Dilute Gases* (Cambridge University Press, Cambridge, 2008).

[23] D. Jin, J. Ensher, M. Matthews, C. Wieman, and E. Cornell. *Collective excitations of a Bose-Einstein condensate in a dilute gas.* Phys. Rev. Lett. **77**, 420 (1996).

[24] M.-O. Mewes, M. Andrews, N. van Druten, D. Kurn, D. Durfee, C. Townsend, and W. Ketterle. *Collective excitations of a Bose-Einstein condensate in a magnetic trap.* Phys. Rev. Lett. **77**, 988 (1996).

[25] D. Jin, M. Matthews, J. Ensher, C. Wieman, and E. Cornell. *Temperature-dependent damping and frequency shifts in collective excitations of a dilute Bose-Einstein condensate.* Phys. Rev. Lett. **77**, 420 (1996).

[26] M. Andrews, C. Townsend, H.-J. Miesner, D. Durfee, D. Kurn, and W. Ketterle. *Observation of interference between two Bose-Einstein condensates.* Science **275**, 637 (1997).

[27] B. Anderson and M. Kasevich. *Macroscopic quantum interference from atomic tunnel arrays.* Science **282**, 1686 (1998).

[28] E. Burt, R. Ghrist, C. Myatt, M. Holland, E. Cornell, and C. Wieman. *Coherence, correlations and collisions: What one learns about Bose-Einstein condensates from their decay.* Phys. Rev. Lett. **79**, 336 (1997).

[29] W. Ketterle and H.-J. Miesner. *Coherence properties of Bose-Einstein condensates and atom lasers.* Phys. Rev. A **56**, 3291 (1997).

[30] E. Hagley, L. Deng, M. Kozuma, M. Trippenbach, Y. Band, M. Edwards, M. Doery, P. Julienne, K. Helmerson, S. Rolston, and W. Phillips. *Measurement of the coherence of a Bose-Einstein condensate.* Phys. Rev. Lett. **83**, 3112 (1999).

[31] R. Gati, B. Hemmerling, J. Fölling, M. Albiez, and M. K. Oberthaler. *Noise thermometry with two weakly coupled Bose-Einstein condensates.* Phys. Rev. Lett. **96**, 130404 (2006).

[32] J. M. Obrecht, R. J. Wild, M. Antezza, L. P. Pitaevskii, S. Stringari, and E. A. Cornell. *Measurement of the temperature dependence of the Casimir-Polder force.* Phys. Rev. Lett. **98**, 063201 (2007).

[33] N. S. Ginsberg, S. R. Garner, and L. V. Hau. *Coherent control of optical information with matter wave dynamics.* Nature **445**, 623 (2007).

[34] W. Bakr, A. Peng, M. Tai, R. Ma, J. Simon, J. Gillen, S. Fölling, L. Pollet, and M. Greiner. *Probing the superfluid-to-Mott insulator transition at the single atom level.* Science **329**, 547 (2010).

[35] L. Pitaevskii and S. Stringari. *Bose-Einstein Condensation* (Oxford Science Publications, Oxford, 2003).

[36] F. Dalfovo, S. Giorgini, L. P. Pitaevskii, and S. Stringari. *Theory of Bose-Einstein condensation in trapped gases.* Rev. Mod. Phys. **71**, 463 (1999).

[37] B. Upcroft. *Atom Chips And Non-Linear Dynamics In Macroscopic Atom Traps* (PhD Thesis. The University of Queensland, 2004).

[38] C. J. Vale, B. Upcroft, M. J. Davis, N. R. Heckenberg, and H. Rubinsztein-Dunlop. *Foil-based atom chip for Bose-Einstein condensates.* J. Phys. B: At. Mol. Opt. Phys. **37**, 2959 (2004).

[39] A. Ratnapala. *Optical Manipulation Of Matter: Thermal and Dynamical Responses in Bose-Condensed Rubidium* (PhD Thesis. The University of Queensland, 2008).

[40] S. K. Schnelle, E. D. van Ooijen, M. J. Davis, N. R. Heckenberg, and H. Rubinsztein-Dunlop. *Versatile two-dimensional potentials for ultra-cold atoms.* Opt. Express **16**, 1405 (2008).

[41] C. W. Gardiner, P. Zoller, R. J. Ballagh, and M. J. Davis. *Kinetics of Bose-Einstein condensation in a trap.* Phys. Rev. Lett. **79**, 1793 (1997).

[42] H.-J. Miesner, D. M. Stamper-Kurn, M. R. Andrews, D. S. Durfee, S. Inouye, and W. Ketterle. *Bosonic stimulation in the formation of a Bose-Einstein condensate.* Science **279**, 1005 (1998).

[43] C. W. Gardiner, M. D. Lee, R. J. Ballagh, M. J. Davis, and P. Zoller. *Quantum kinetic theory of condensate growth: Comparison of experiment and theory.* Phys. Rev. Lett. **81**, 5266 (1998).

[44] M. D. Lee and C. Gardiner. *Quantum kinetic theory. VI. The growth of a Bose-Einstein condensate.* Phys. Rev. A **62**, 033606 (2000).

[45] M. J. Davis, C. W. Gardiner, and R. J. Ballagh. *Quantum kinetic theory. VII. The influence of vapor dynamics on condensate growth.* Phys. Rev. A **62**, 063608 (2000).

[46] M. C. Garrett, A. Ratnapala, E. D. van Ooijen, C. J. Vale, K. Weegink, S. K. Schnelle, O. Vainio, N. R. Heckenberg, H. Rubinsztein-Dunlop, and M. J. Davis. *Growth dynamics of a Bose-Einstein condensate in a dimple trap without cooling.* Phys. Rev. A **83**, 013630 (2011).

[47] C. Raman, M. Köhl, R. Onofrio, D. S. Durfee, C. E. Kuklewicz, Z. Hadzibabic, and W. Ketterle. *Evidence for a critical velocity in a Bose-Einstein condensed gas.* Phys. Rev. Lett. **83**, 2502 (1999).

[48] P. Engels and C. Atherton. *Stationary and non-stationary fluid flow of a Bose-Einstein condensate through a penetrable barrier.* Phys. Rev. Lett. **99**, 160405 (2007).

[49] C. Feng. *Superfluid Critical Velocity in a Line Trap Potential* (PhD Thesis in preparation. The University of Queensland, 2010).

[50] K. Huang. *Statistical Mechanics* (Wiley & Sons, 1987).

[51] L. Landau and E. Lifshitz. *Quantum Mechanics* (Pergamon, Oxford, 1987).

[52] D. A. Steck. *Rubidium 87 Line Data* .

[53] J. Fortagh and C. Zimmermann. *Magnetic microtraps for ultra-cold atoms.* Rev. Mod. Phys. p. 235 (2007).

[54] T. Hänsch and A. Shawlow. *Cooling of gases by laser radiation.* Opt. Commun. **13**, 68 (1975).

[55] D. Wineland and H. Dehmelt. *Proposed* 10^4 $\delta\nu/\nu$ *laser fluorescence spectroscopy on* Tl^+ *mono-ion oscillator III (side band cooling).* Bull. Am. Phys. Soc. **20**, 637 (1975).

[56] H. J. Metcalf and P. van der Straten. *Laser Cooling and Trapping* (Springer, Cambridge, Massachusetts, 1997).

[57] J. Dalibard and C. Cohen-Tannoudji. *Laser cooling below the Doppler limit by polarization gradients: simple theoretical models.* J. Opt. Soc. Am. B **6**, 2023 (1989).

[58] A. L. Migdall, J. V. Prodan, and W. D. Phillips. *First observation of magnetically trapped neutral atoms.* Phys. Rev. Lett. **54**, 2596 (1985).

[59] W. Ketterle, D. S. Durfee, and D. M. Stamper-Kurn. *Making, probing and understanding Bose-Einstein condensates.* AI Magazine **1**, 127 (1999).

[60] W. Petrich, M. Anderson, J. Ensher, and E. Cornell. *Stable, tightly confining magnetic trap for evaporative cooling of neutral atoms.* Phys. Rev. Lett. **74**, 3352 (1995).

[61] A. Ashkin. *Acceleration and trapping of particles by radiation pressure.* Phys. Rev. Lett. **24**, 156 (1970).

[62] J. Butcher. *Scanning Potentials for an All-Optical Bose-Einstein Condensate* (MSc Thesis. The University of Queensland, 2010).

[63] E. van Ooijen, K. Weegink, S. Haine, H. Rubinsztein-Dunlop, and M. Davis. *Dynamical, time-averaged 2D optical lattice traps for Rydberg atom quantum computing.* to be submitted to Phys. Rev. Lett .

[64] R. Grimm, M. Weidemüller, and Y. B. Ovchinnikov. *Optical dipole traps for neutral atoms.* Adv. At. Mol. Opt. Phys. **42**, 95 (2000).

[65] L. Allen and J. H. Eberly. *Optical Resonance and two-level atoms* (Wiley, 1975).

[66] C. Cohen-Tannoudji. *Manipulating atoms with photons.* Rev. Mod. Phys. p. 707 (1998).

[67] A. E. Siegman. *Lasers* (Oxford University Press, Oxford, 1987).

[68] A. Sa. *Do you know accousto optics? Application notes.* (AA Opto-Electronic).

[69] W. Petrich, M. H. Anderson, J. R. Ensher, and E. A. Cornell. *Stable, tightly confining magnetic trap for evaporative cooling of neutral atoms.* Phys. Rev. Lett. **74**, 3352 (1995).

[70] P. Rudy, R. Ejnisman, A. Rahman, S. Lee, and N. P. Bigelow. *An optical dynamical dark trap for neutral atoms.* Opt. Express **8**, 159 (2001).

[71] N. Friedman, L. Khaykovich, R. Ozeri, and N. Davidson. *Compression of cold atoms to very high densities in a torating-beam blue-detuned optical trap.* Phys. Rev. A **61**, 031403 (2000).

[72] V. Milner, J. L. Hanssen, W. C. Campbell, and M. G. Raizen. *Optical billiards for atoms.* Phys. Rev. Lett. **86**, 1514 (2001).

[73] A. S. Arnold, C. S. Garvie, and E. Riis. *Large magnetic storage ring for netral atoms.* Phys. Rev. A **73**, 041606 (2006).

[74] S. Gupta, K. W. Murch, K. L. Moore, T. P. Purdy, and D. M. Stamper-Kurn. *Bose-Einstein condensation in a circular waveguide.* Phys. Rev. Lett. **95**, 143201 (2007).

[75] J. A. Sauer, M. D. Barrett, and M. S. Chapman. *Storage ring for neutral atoms.* Nature **87**, 270401 (2001).

[76] O. Morizot, Y. Colombe, V. Lorent, and H. Perrin. *Ring trap for ultracold atoms.* Phys. Rev. A **74**, 023617 (2006).

[77] S. Franke-Arnold, J. Leach, M. J. Padgett, V. E. Lebessis, D. Ellinas, A. J. Wright, J. M. Girkin, P. Öhberg, and A. S. Arnold. *Optical ferris wheel for ultracold atoms.* Opt. Express **15**, 8619 (2007).

[78] C. Ryu, M. F. Anderson, P. Clade, V. Natarajan, K. Helmerson, and W. D. Phillips. *Observation of persistent flow of a Bose-Einstein condensate in a toroidal trap.* Phys. Rev. Lett. **99**, 260401 (2007).

[79] J. R. Abo-Shaeer, C. Raman, J. M. Vogels, and W. Ketterle. *Observation of vortex lattices in Bose-Einstein condensates.* Science **292**, 476 (2001).

[80] M. Köhl, M. Davis, C. Gardiner, T. Hänsch, and T. Esslinger. *Growth of Bose-Einstein Condensates From Thermal Vapor.* Phys. Rev. Lett. **88**, 080402 (2002).

[81] M. Davis and C. Gardiner. *Growth of a Bose-Einstein Condensate: A Detailed Comparison of Theory And Experiment.* J. Phys. B: At. Mol. Opt. Phys. **35**, 733 (2002).

[82] M. Hugbart, J. Retter, A. Varon, P. Bouyer, A. Apsect, and M. Davis. *Population And Phase Coherence During The Growth of an Elongated Bose-Einstein Condensate.* Phys. Rev. A **75**, 011602 (2007).

[83] S. Ritter, A. Öttl, T. Donner, T. Bourdel, M. Köhl, and T. Esslinger. *Observing The Formation of Longe-Range Order During Bose-Einstein Condensation.* Phys. Rev. Lett. **98**, 090402 (2007).

[84] C. Weiler, T. Neely, D. S. adn A.S. Bradley, M. Davis, and B. Anderson. *Spontaneous Vortices in the Formation of Bose-Einstein Condensates.* Nature **455**, 984 (2008).

[85] M. J. Davis. *Dynamics of Bose-Einstein Condensation* (PhD Thesis. University of Oxford, 2001).

[86] M. J. Bijlsma, E. Zaremba, , and H. T. C. Stoof. *Condensate growth in trapped Bose gases.* Phys. Rev. A **62**, 063609 (2000).

[87] M. Houbiers, H. T. C. Stoof, and E. A. Cornell. *Critical temperature of a trapped Bose gas: Mean-field theory and fluctuations.* Phys. Rev. A **56**, 2041 (1997).

[88] C. W. Gardiner, J. R. Anglin, and T. Fudge. *The stochastic Gross-Pitaevskii equation.* J. Phys. B: At. Mol. Opt. Phys. **35**, 1555 (2002).

[89] C. W. Gardiner and M. Davis. *The stochastic Gross-Pitaevskii equation: II.* J. Phys. B: At. Mol. Opt. Phys. **36**, 4731 (2003).

[90] Y. Castin and R. Dum. *Bose-Einstein Condensates in time dependent traps.* Phys. Rev. Lett. **77**, 5315 (1996).

[91] K. J. Weegink. *Time Averaged Optical Potentials For Trapping Bose-Einstein Condensates* (Honours Thesis. The University of Queensland, 2010).

[92] G. W. F. Drake. *Springer Handbook Of Atomic, Molecular, And Optical Physics* (Springer, New York, 2006).

[93] M. Olsen and A. Bradley. *Computational Physics PHYS3071.* The University of Queensland (2007).

[94] J. Hope. *XmdS: Extensible multi-dimensional simulator* URL `http://www.xmds.org/index.html`.